Lithological Mapping of Northwest Argentina with Remote Sensing Data Using Tonal, Textural and Contextual Features

Robin Bryan Oldfield

Doctor of Philosophy

Aston University
August 1988

Acknowledgements

I would like to thank Islwyn Thomas of the National Remote Sensing Centre and Dave Rothery of the Open University for the provision of the LANDSAT MSS data used in this project. Charles Elachi of the National Space Science Data Center for the provision of SIR-A data, and Nigel Gammage of Joyce Loebl for digitising these data. I would also like to thank my supervisors, John Elgy and John Morton, and Gordon Collins head of the remote sensing unit for their help and support. Finally, I must thank John Cox of the Library and Information Services and the postgraduates in the remote sensing unit (especially David Booth) for their help and friendship.

Summary

Tonal, textural and contextual properties are used in manual photointerpretation of remotely sensed data. This study has used these three attributes to produce a lithological map of semi arid northwest Argentina by semi automatic computer classification procedures of remotely sensed data. Three different types of satellite data were investigated, these were LANDSAT MSS, TM and SIR-A imagery.

Supervised classification procedures using tonal features produced only poor classification results. LANDSAT MSS produced classification accuracies in the range of 40 to 60%, while accuracies of 50 to 70% were achieved using LANDSAT TM data. The addition of SIR-A data produced increases in the classification accuracy. The increased classification accuracy of TM over the MSS is because of the better discrimination of geological materials afforded by the middle infra red bands of the TM sensor. The maximum likelihood classifier consistently produced classification accuracies 10 to 15% higher than either the minimum distance to means or decision tree classifier. This improved accuracy was obtained at the cost of greatly increased processing time. A new type of classifier, the Spectral Shape Classifier, which is computationally as fast as a minimum distance to means classifier is described. However, the results for this classifier were disappointing, being lower in most cases than the minimum distance or decision tree procedures.

The classification results using only tonal features were felt to be unacceptably poor, therefore textural attributes were investigated. Texture is an important attribute used by photogeologists to discriminate lithology. In the case of TM data, texture measures were found to increase the classification accuracy by up to 15%. However, in the case of the LANDSAT MSS data the use of texture measures did not provide any significant increase in the accuracy of classification. For TM data, it was found that second order texture, especially the SGLDM based measures, produced highest classification accuracy.

Contextual post processing was found to increase classification accuracy and improve the visual appearance of classified output by removing isolated misclassified pixels which tend to clutter classified images. Simple contextual features, such as mode filters were found to out perform more complex features such as a gravitational filter or minimal area replacement methods. Generally the larger the size of the filter, the greater the increase in the accuracy.

Production rules were used to build a knowledge based system which used tonal and textural features to identify sedimentary lithologies in each of the two test sites. The knowledge based system was able to identify six out of ten lithologies correctly.

Key words: Argentina, Geological Remote Sensing, Digital Image Processing, Textural Analysis, Contextual Analysis

Contents

List of Figures

List of Maps

List of Plates

List of Tables

List of Appendices

Chapter 1
Introduction

1.0 Data Production Rates

Remotely sensed data are being acquired at such rates that it is now impossible to view all scenes which are recorded. According to Hardy (1985) LANDSAT Multispectral Scanner (MSS) generates $5x10^3$ bits/km^2 (208 pixels by six bits by four bands). The Thematic Mapper (TM) on LANDSAT four and five generates $5.4x10^4$ bits/km^2 and the SPOT High Resolution Visible (HRV) sensor generates $6x10^4$ bits/km^2 in multispectral mode and $8x10^4$ bits/km^2 in panchromatic mode. If the area covered by a typical satellite is $5x10^8$ km^2, and this is covered in say 16 days, then the earth is covered by somewhere in the region of 10^{14} bits of data every year by just one satellite. Put another way this is equivalent to over 100 000 Computer Compatible Tapes (CCT's) recorded at 6250 Bits per inch (BPi) every year. Furthermore with the new generations of radar satellites now being planned such as ERS-1 (and ERS-2), RADARSAT and the Japanese radar satellite, this situation can only be exacerbated. Especially as active sensors such as these radars can produce images in all weathers both night and day. The data generated by these satellites may be useful for a number of different disciplines, therefore the processing of the data is daunting. A plethora of papers appear when a new sensor becomes operational while the data from yesterday's satellite is left not fully investigated for their potential benefits.

1.1 The Nature of Remotely Sensed Data

The user needs knowledge or information about an object being sensed by a remote sensing device, in a form which he can understand. This information is generated by interpretation of the data. Remotely sensed data can be interpretted in two ways: firstly by the human interpreter and secondly by computer. The human interpretation may take place either prior to enhancement or after enhancement; the enhancement may either be non digital (photographic enhancement),or digital (computer enhancement). Typical enhancement might be contrast stretching or edge sharpening. Computer analysis may be in the form of the production of area statistics of classes in a scene, or the production of a thematic map such as land cover or lithological map.

In an ideal world remotely sensed data would be stationary (that is, the measurements made on an unchanging object would not vary with time). The variations of the physical properties of an object would be explained by simple mathematical models

(for example gaussian distributions). The physical properties being sensed might be the spectrum of energy a material reflects (or absorbs), a particular wavelength of radiation it emits, or some property of its radar roughness. Therefore the sensor would image in regions of the electromagnetic spectrum where the object being sensed was uniquely discriminated and identified.

In the real world of course the criteria above are not found; normally the remotely sensed data is non-stationary, non gaussian distributions are found, physical properties of objects are ambiguous, and the image is noisy to a greater or lesser extent. Furthermore, the means of analysis is by computer (digital image processor) which are normally not designed for remote sensing data sets. Most computers are designed to hold relatively small data sets with a high degree of precision. However, remote sensing images are normally large data sets, for example 3240 by 2340 pixels for a typical LANDSAT MSS scene(LANDSAT TM and SPOT images are much larger), held with a low degree of precision (typically eight bits or less for each band). Therefore there is a mismatch between the data source and the means of analysing it. In the real world therefore there are many problems which need to be investigated.

1.2 Trends in Remote Sensing

Many trends or developments in the twin fields of remote sensing and digital image processing can be identified. These include the following:

1) Higher resolution images and therefore much larger data arrays. In the past decade the spatial resolution of earth resource satellites has come down from about 80 m (for LANDSAT MSS), to 30 m in 1982 (for LANDSAT TM) to 10 m in 1986 (for SPOT HRV panchromatic). A LANDSAT MSS image pixel is therefore covered by some 64 SPOT panchromatic pixels. The Earth Observation Satellite Company (EOSAT) who operate the LANDSAT series of satellites are investigating the possibility of placing a panchromatic band on LANDSAT 6 or 7 which will have a spatial resolution of 5 m, and therefore the increasing spatial resolution of sensors will continue into the forseeable future.

2) More and better positioned spectral bands. LANDSAT MSS has four bands in the visible and near infra red, these bands are both broad (that is they cover a wide part of the electromagnetic spectrum) and are in adjacent parts of the spectrum, so that particular spectral features cannot be identified. LANDSAT TM has six bands which are both narrower and better positioned than the bands for LANDSAT MSS. This is particularly important in geological surveys because of the ambiguous spectral response of geological materials in the visible and near infra red. The trend toward terrestrial

sensors with improved spectral capability continues, from the ATM with 11 bands, to instruments such as the Fluorescent Line Imager (FLI) which has some 288 channels covering the visible to the thermal infra red. It is only a matter of time before a spaceborne spectroradiometer of this sort is launched.

3) Three dimensional data sets for stereoscopic viewing. These are the norm in aerial surveys because of the topographical information they provide. The SPOT satellite is the first commercial earth resources satellite available with the ability to produce stereoscopic images at nearly all latitudes. Stereoscopic images are particularly important in geological work because of the structural detail they give, such as amount and direction of bedding dip, amount and direction of fault movement and chronostratigraphic information such as unconformable contacts.

4) The use of multitemporal and or multisensor data sets. This will become particularly important when radar data sets become routinely available in the 1990's, in the same way that multispectral passive images are now available from the LANDSAT and SPOT satellites. The importance of radar images is that they have 'all weather night and day' imaging capability, because they provide their own energy to sense an object. They also provide information about the physical properties of an object, such as its roughness or complex dielectric constant, which are not provided by other sensors. Therefore radar images have very important benefits to both the civilian and the military remote sensor.

5) The repeat time of sensors. This is an important point, especially in the case of dynamic situations such as monitoring volcanic events. The repeat time (the revisit time for a point on the earth's surface) of LANDSAT's 1, 2 and 3 was 18 days, this was reduced to 16 days with LANDSAT's 4 and 5. Although the revisit time for an orbit of the SPOT satellite is 26 days, the satellite can steer its sensors so that (depending on latitude) a revisit time of 3 to 4 days is possible. The revisit time of meteorological satellites is by necessity much more frequent than those of earth resources satellites: once a day for AVHRR data, and three images an hour for METEOSAT data. Much useful work can be done viewing large scale geological phenomenon with these satellites, such as monitoring the progress volcanic clouds in the upper atmosphere.

In order to be able to fully exploit the information content of the data which is currently being produced by remote sensing devices, it will be necessary to develop algorithms which efficiently process and analyse the data. This means producing results which are satisfactory to an end user who may have no knowledge of how the product was generated. It may be possible that processing to geometrically and radiometrically correct the data onboard the satellite will be developed. Radar images might be converted to images onboard the satellite, perhaps by using a transputer array to

perform the necessary processing. Processing of this sort is important because it not only cuts down the amount of processing which must take place on the ground, it also means that the amount of data transmitted to the ground might be reduced. Further investigation into the uses of radar images and combined data sets must be undertaken. However, one of the problems of such multiple data sets was pointed out by Mather (1985) who states that the computational time of the maximum likelihood classifier increases as a square of the number of bands. Therefore new algorithms must be investigated which are both computationally simple and efficient. Multisensor data sets are a great demand on computer time, however, advanced processor technology such as that described by Landgrebe (1981) is likely in the near future to make this less of a problem.

Clearly there is a need for a policy on archiving otherwise, the rate of production would eventually outstrip the ability to record and store the data. This means devising algorithms to do automatically, or at least semi automatically, what is currently done by the human interpreter. It also means throwing data away which is either of poor quality or of little interest to users. While this rather glib statement sounds relatively straightforward this is no means the case, as some of the very special operations that are undertaken by the human brain are at present very difficult if not impossible to emulate. Furthermore, problems of archiving are exacerbated by the fact that one scientist's cloud ruined scene is another's interesting weather pattern. One of the tasks for remote sensing scientists must be to evaluate the full potential of each type of imagery for each interested discipline. This means research into the fields of Artificial Intelligence and image understanding. This is a long term aim for digital image processing, in the shorter term there should be an aim to better exploit the data with more sophisticated analysis techniques and to produce more accurate useful and timely products.

1.3 The Aims of this Research

The aims of this research are to investigate the various types of multisensor data set (which are now becoming increasingly common), and their application to lithological mapping. This is of great interest, as large regions of the planet remain either poorly mapped or totally unmapped in terms of both geomorphology and geology. This is particularly the case in desert areas where the inhospitable conditions make fieldwork both expensive and dangerous. It is intended that remote sensing data sets can be used to produce geometrically and lithologically accurate thematic maps. There is a slight problem here, because the only way at present to produce geometrically correct remote

sensing data is to register to an existing map or surveyed ground control points. It is envisaged that in the near future the orbital characteristics of resources satellites will be monitored sufficiently, so that the geometric errors of the satellite can be modelled. Therefore, accurate maps will be produced from these data without the need for reliable base maps. The techniques which are described and tested in this work have been specifically applied to lithological mapping. However, exactly the same techniques can find application in the many diverse subjects for which digital satellite data has found use.

1.4 Methodology

Chapter 2, deals with geological remote sensing and some of the techniques, both digital and non-digital, which are currently used for this work. The next chapter discusses digital image classification techniques and attempts to show why these techniques have received but limited success in the field of lithological mapping. Chapter four describes the nature of the imagery used for this work. Chapter five describes the geological setting of the study areas for this research (that is North Western Argentina) and the appearance of the lithounits in the imagery. Chapter six investigates the techniques of textural classification and attempts to show which are the most useful for remotely sensed data sets. The following chapter introduces some of the ideas which have been suggested for contextual analysis for increasing classification accuracy, and describes the results of tonal/textural and contextual classification of the test sites. Chapter eight describes how simple knowledge based rules may possibly be used for high level labelling of classes in imagery. This means assigning names to lithotypes in a similar way to the photogeologist. Finally the conclusions of the research are drawn and a discussion about the possible benefits of this research is given along with possible areas for further research.

Chapter 2
Geological Remote Sensing

2.0 Introduction

Geological remote sensing is an extension of the earlier discipline of photogeology. Photogeology can be defined as the visual extraction of geological information from photograph or image (Robinove, 1963). The term remote sensing was first used in the early 1960's with the first Symposium on Remote Sensing of Environment (University of Michigan, 1962). Much of the impetus for remote sensing was provided by the declassification of military imagery and the wide variety of electronic and optoelectronic scanners then being developed (Colwell, 1983). Further momentum occurred with the advances in platform design and especially the potential made possible by space platforms.

Geological remote sensing includes all the techniques and principles of photogeology combined with a multitude more borrowed from a wide variety of other disciplines such as computing, chemistry, spectroscopy and physics. The term embraces the manual and digital analysis of images from a large number of remote sensing devices in order to extract geological information. The importance geological remote sensing is underlined by Allan (1986) who shows that this is one of the few commercially viable areas of remote sensing.

A number of texts have been published on both photogeology and geological remote sensing. Photogeology Regional Mapping (Allum, 1966) remains a classic text on photogeology. The first edition of the manual of remote sensing has a chapter given over to "Terrain and Minerals: Assessment" (Reeves et al., 1975) and this is updated in the second edition under the title "Photogeology and Geological Remote Sensing" (Williams, 1982). One of the best texts in geological remote sensing remains "Remote Sensing in Geology" (Siegal and Gillespie, 1980), two of the four sections are devoted to image processing and enhancement techniques. Slaney (1982) in "LANDSAT Images of Canada a Geological Appraisal" provides field geologists with LANDSAT imagery and invites them to comment on the usefulness of these data. Probably the most visually impressive and most up to date text in this area is Image Interpretation in Geology (Drury, 1986a). This book includes excellent chapters on thermal images, radar images and image processing.

2.1 Development of Geological Remote Sensing

As previously stated the use of conventional aerial photography in geological interpretation is a long established technique but it was not until the results of the space programme became available that the scope of remote sensing in geology began to be appreciated. For example much of the pioneering work on lunar stratigraphy was carried out by the United States Geological Survey (notably by Shoemaker and Hackman) from earth based photography and Soviet Moon probe imagery (Rothery, 1985a).

Many geologists (particularly academics) remain largely unaware of the geological value of remotely sensed data. Many may have become disenchanted by the wild, and largely unfilled claims made in the early days of LANDSAT, others were probably disappointed by the poor quality of the standard products produced by NASA (Rothery, 1985b). However, hardware and software for digital processing of these data is now becoming comparatively inexpensive. An example of what can be achieved can be found in the remote sensing unit at Aston, here 3 frame grabber boards each able to hold 512 x 1024 x 8 bits of data were purchased to work with an IBM PC-AT host. A certain number of low level subroutines were provided with the boards for software development. The total cost of the system including IBM PC, display and colour printer was somewhere in the region of £7000 in 1987 prices. With this price tag the production of products suitable for the special requirements of the geologist are now possible for relatively small (under financed) Geology Departments and for small companies.

2.2 Objectives of Geological Remote Sensing

The major objectives of geological remote sensing from satellite data were given by Fischer (1976) he lists four main aims, these are:

1. The identification and location of large features (including glacial, fault, and volcanic features) which are present on the surface of the earth, but because of their size and subtle expression have gone unrecognised. These features can be seen because of the synoptic viewpoint given by satellites.

2. The use of multispectral imagery for mapping the distribution of lithology.

3. The identification of certain environmental features which are only intermittently visible depending on the angle of illumination and on snow, water or vegetation distributions.

4. Viewing certain geological processes such as vulcanicity or sedimentation which can be better understood if seen in some form of time lapse mode.

The following sections describe some of the routine ways in which remotely sensed imagery has been applied to geological problems and some of the manipulation techniques carried out. An emphasis in this text is placed on those techniques which satisfy Fischer's second aim of geological remote sensing, because this is the major thrust of this thesis.

2.3 Lineament Analysis

O'Leary et al. (1976) defined a lineament as a "mappable, single or composite linear feature of a surface, whose parts are aligned in a rectilinear or slightly curvilinear relationship. . . . and reflect a subsurface phenomenon". They can be formed by a variety of geomorphological elements, including, topography, vegetation and soil or rock tonal alignments. Most appear to be continuous, but on closer inspection consist of closely spaced edge and line segments which tend to be merged by the eye. This intermittent nature of lineaments is one of the reasons why it is difficult to produce algorithms which will objectively enhance and extract these features.

Geological lineaments are important for a number of reasons, they may represent fault or fracture zones. These zones may be areas of high seismic risk or subsidence. They also be areas of economic importance, for example it is well known that certain types of mineralising fluids tend to follow zones of weakness in rocks these can give rise to the famous Mississippi valley (Cu-Pb-Zn) type of mineral deposit.

Many studies by photo-interpretation of lineaments have been attempted, Qureshy (1982) found coincidence between photo-interpreted lineaments in LANDSAT MSS imagery and gravity and magnetic data of a study area in northern India. Ray et al. (1980) studied lineaments in LANDSAT MSS imagery of northwestern India they linked this to the genesis of base metal mineralisation in the area. Other studies include Babcock and Sheldon (1976); Bhan and Krishnanunni (1983); Gold and Parizck (1976); Haman (1976) and Wheeler and Stubbs (1976).

2.3.1 Measuring Lineaments

Podwysocki et al. (1976) studied lineaments interpreted by four different skilled observers. They found that "only 0.4% of the total 785 linears" (in the image) " were seen by all four operators, 5% by three operators, and 18% by two operators". The study also showed that the average lengths of the lineaments mapped by different observers were significantly different. It should also be noted that right handed interpreters find it easier to draw NE-SW trending lines (conversely left handed interpreters find easier to draw NW-SE lines). To avoid bias, the image should be periodically rotated through 90°. These results show some of the drawbacks of manual interpretation of lineaments. It is for these reasons that objective procedures for lineament enhancement and extraction have been proposed.

2.3.2 Lineament Enhancement Methods

Various techniques have been tested to enhance lineaments, these include both digital and optical processing methods. The next sections describe some these.

2.3.2.1 Optical Processing

Pohn (1970) pointed out that lineaments could be enhanced by using a coarse diffraction grating consisting of closely spaced parallel lines on a glass or plastic plate. The apparatus is slowly rotated in front of the image, features perpendicular to the grating become enhanced at the expense of those parallel to the grating (ie directional filtering). This apparatus is known as "Ronchi Ruling" and was used to identify several sets of linear features by Offield (1975).

Other optical techniques for lineament extraction are based on the Fourier transform of the image. If an image is thought of as a two dimensional surface where the brightness at any point (i,j) represents the height of the surface at that point then the image can be thought of as a three dimensional wave surface. This wave can be thought of as a composite wave made up of pure sine and cosine waves of various amplitudes and frequencies. The low spatial frequency content of the image represents large areas with constant brightness. High frequency information consists of brightness changes over a short spatial dimension. Lineaments therefore can be thought of as belonging to the high spatial frequency component of the image.

McCullagh and Davis (1972) found that the technique was useful for showing the spatial frequencies in various types of aerial images. Experiments using the optical Fourier transform on LANDSAT imagery were carried out by Barnett et al. (1976). They were able to extract textural information corresponding to fine details in the image and thus they claim that a better appreciation of the geological structure can be obtained.

2.3.2.2 Digital Processing

Two types of digital processing have been used for lineament analysis, these are firstly, Fourier based techniqes and secondly, techniques based on convolution filtering. In the Fourier transform the image is separated into its component sine and cosine waves, the image is said to be transformed from the spatial domain to the frequency domain. The transform can be performed by both optical and digital means. The transform is fully reversible so that the Fourier transform of an image can be transformed back to the original image. The simplest way to view a Fourier transform of an image is by computing the power spectrum, this is the magnitude of the transform at each (i,j) point in the image.

$$\text{power spectrum} = \sqrt{((\text{real part})^2 + (\text{imaginary part})^2)} \qquad \textit{equation 2.1}$$

The power spectrum shows the highest spatial frequencies at the centre of the transformed image and successively lower spatial frequencies at greater distances away from the centre. The direction of a particular frequency is given by the angle that it plots at.

Various filters which can block out or enhance certain directions or frequencies can be used. The simplest way of blocking out the lower frequencies is a ring which allows frequencies near the centre of the image to be passed while impeding those which occur in the vicinity of the ring.

Gramenopoulos (1973) used both optical and digital Fourier methods to extract spatial signatures of land cover classes using LANDSAT MSS data, he had accuracies ranging from 11% for river beds to 97% for a desert class. Fredericksen (1981) used digitised aerial photography in order to obtain spatial signatures of various geological and geomorphological classes using the Fourier transform.

This is a digital technique in which a small matrix (or kernel) is passed over all the pixels in the image. The pixel to be altered (in figure 2.1 this is denoted by P5) is

replaced by some mathematical function of the pixels in the kernel (see figure 2.1). In general the new pixel value P5' is given by:

$$P5' = (A.P1 + B.P2 + C.P3 + D.P4 + E.P5 + F.P6 + G.P7 + H.P8 + I.P9)/K$$

equation 2.2

Where P1, P2, P3, P4, P6, P7, P8 and P9 are the neighbouring pixel values to P5. A, B, C, D, E, F, G, H and I are kernel values as shown in figure 2.1, and K is constant.

The new central pixel is placed in the output image and the kernel advances along one pixel in the image as shown in figure 2.2. Typical sizes of kernels are 3 x 3, 5 x 5, 7 x 7 but sizes of up to 101 x 101 are sometimes used. For example, the average of the pixels in the kernel may calculated, the output image will appear blurred because the high spatial frequencies are suppressed. If this (low pass filtered) image is then subtracted from the unfiltered image then only the high frequencies will remain. As already stated these high spatial frequencies include the lineaments which we are seeking. This type of approach known as subtractive filtering was used by Chavez et al. (1976), Thomas et al. (1981) and by Brunner and Veck (1985).

Figure 2.1 To illustrate the Kernel used in convolution filtering

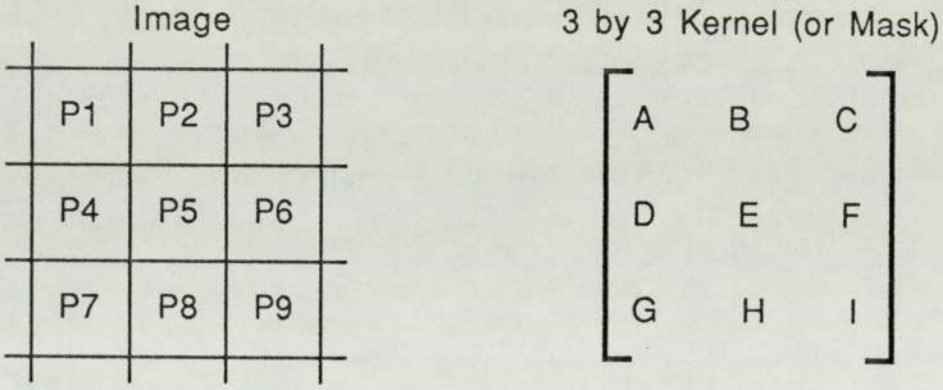

Figure 2.2 To illustrate the movement of a filter through the image

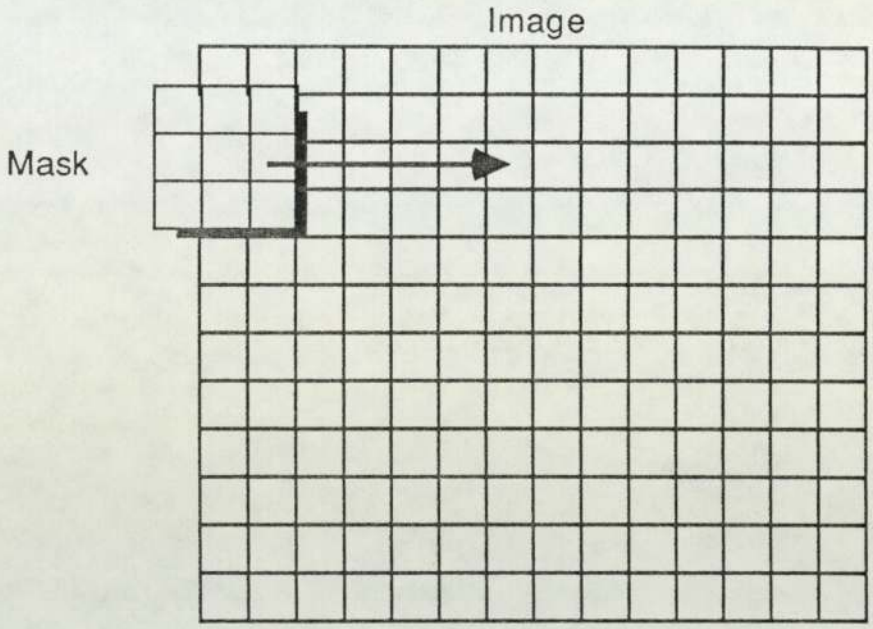

Filters which enhance high spatial frequencies are known as high pass filters, those which suppress high spatial frequencies are known as low pass filters. Non square filters or directional filters are sometimes used but these can introduce linear artefacts into the image (Gillespie, 1976). Directional filters were used by Moore and Waltz (1983) who outline an objective procedure for lineament enhancement. This method involves selective thresholding of the filtered imagery to find the lineaments in the imagery after filtering. Drury (1986b) finds disappointing results for directional filtering of LANDSAT TM imagery of South west England because of the clutter caused by agricultural features.

2.4 Lithological Mapping

The major aim of geological mapping is to identify geological materials, in terms of age, structural relationship and lithology. Remote sensing cannot give absolute ages but can be sometimes indicative of relative age. Just as a field geologist bases his subdivisions on hand specimens which are more generalised than the subdivisions used by the petrologist using the microscope, so the photogeologist must use more generalised subdivisions than the field geologist. The ability to distinguish lithology is often very much restricted because of the relatively poor positioning of spectral bands and the low spatial resolution in many remote sensing devices used for geological work. Lithological mapping using remotely sensed data involves the ability to both distinguish and identify at least two lithofacies in the imagery. The ability to distinguish implies recognising differences in spectral and/or spatial properties of the classes in the data. The ability to identify lithological materials is a much more difficult problem than simply distinguishing them. Lithological materials which are quite different lithologically may have similar spectral responses while similar materials may have different spectral responses. This is further exacerbated by vegetation and soil development which can alter spectral signatures. Geological photo-interpreters are able to recognise and map units in an image by a number of different criteria, including differences in albedo, spectral contrast, textural (spatial) properties and by position in the image. It is these skills which the computer must emulate in order to routinely process images in a meaningful way.

2.4.1 Spectral Identification and Discrimination of Geological Materials

LANDSAT MSS data has a spectral range that covers only the visible and the near IR parts of the electromagnetic spectrum. In this region of the spectrum limonite (a catch all term for iron hydroxides) is the only mineral which can be uniquely identified (Hunt, 1976). Limonite has absorption bands associated with the ferric cation which gives rise to a characteristic spectral response in this part of the spectrum. The unique identification of rock material is therefore not possible in the visible or near IR. However, considerable success can be achieved in delineating and discriminating rock units, providing the correct processing is carried out.

Limonite is important because hydrothermally altered rocks often contain iron pyrites which oxidizes to give limonite. Rowan et al. (1974), Podwysocki and Segal (1980), and Podwysocki et al. (1982) used multispectral scanner data to delineate limonitic material which may be associated with hydrothermally altered rock. However, not all

limonite occurs in hydrothermally altered rocks, or hydrothermally altered rocks may occur without iron pyrites. Therefore the presence or absence of limonite does not unequivocally prove hydrothermal alteration.

Distinctive silicate bending and stretching vibrations occur when silicate lattices are excited by radiation from the middle and the thermal infrared. This gives rise to distinctive spectral responses for these materials in those parts of spectrum. As silicates make up over 80% of the earths crust they are of the upmost importance for the geologist. For these reasons much effort has been expended producing scanners such as TIMS (thermal inertia multispectral scanner) and other thermal scanners and even spectro-radiometers such as FLI (fluorescent line imager) which has up to 288 channels.

Minerals such as carbonates, clay minerals such as kaolinite, montmorillonite, jarosite, alunite, sericite and pyrophyllite have distinctive spectra in the middle infra red 1.8 μm to 2.5 μm range. It is for this reason that the band 7 of the thematic mapper was added (on the recommendation of the GEOSAT working group (Henderson and Swann, 1976)). This band was added at such a late stage that it was given the name band 7 even though band 6 is a thermal band covering the 10 μm to 12 μm range.

Clay and other minerals diagnostic of hydrothermally altered rocks have been mapped using aircraft MSS data by Ashley and Abrams (1980), and by Rowan and Kahle (1982) and using satellite data by Rothery (1987).

The thermal IR (8-14 μm) range is especially important for the reasons stated above, that is it contains emittance minima diagnostic of the major types of silicates (Vincent et al., 1975); Hunt (1981). These minima occur at different spectral positions depending primarily on the mineral composition. The position of these absorption features is associated with bending and stretching movements in the Si - 0 tetrahedra (the so called restrahlen bands). The amount of absorption is dependent on the interconnection of the Si - 0 tetrahedra comprising the crystal lattice. The end members are represented by quartz with complete sharing of all oxygen molecules, to olivine, with its isolated $Si0_4$ tetrahedra (Goetz and Rowan, 1983).

2.4.2 Radar Image Analysis

Radar images provide complementary information to other forms of remote sensing imagery which make them useful for mapping the surface roughness of classes on the

ground. In terms of lithology this means that they can often differentiate between fine and coarse grained rocks. Koopmans (1985) using SAR 580 data of European test sites found that the "spectral" characteristics of radar data were not useful for mapping rock units. He found that the geological information was bound up the texture of the image, the texture being related mostly to the drainage pattern. Evans et al. (1986) used 10m resolution multipolarisation data over geological sites in the Death Valley area of California. The radar images gave data for the mapping of surficial deposits of differing age, lithology, and chemical composition. In the Wind River Basin area, they found that multiple polarisation radar data could discriminate sedimentary rocks based on their surface roughness and vegetation cover.

2.4.3 Coregistered Multispectral Imagery and Radar Imagery

Stewart et al. (1980) used coregistered LANDSAT MSS and SEASAT data of the San Rafael Swell area of Utah. This is a large breached asymmetric anticline composed of a variety of sedimentary rock types. The SEASAT image allows differentiation of fine grained rock units from coarse grained units, because it is sensitive to surface roughness. The LANDSAT image on the other hand provides surface composition information, therefore the two images provide complementary information. Furthermore the SEASAT image with a pixel size of 35 m allows additional lithological units to be differentiated, the added texture is of great help in distinguishing between some of the subtly different units.

Geometric registration of SIR-A, SEASAT and LANDSAT MSS images was carried out by Rebillard et al. (1984) for analysis of a terrain in northern Tunisia. The SEASAT image was chosen as the reference image and root mean square (RMS) errors of two to three pixels in both x and y were obtained for a least square method of solving the transform equations and using a bicubic interpolation. Similar RMS errors were found by Oldfield et al. (1988) using LANDSAT MSS, TM and SIR-A data in a study area of northern Argentina.

2.4.4 Band Ratioing

Various arithmetic combinations of bands are possible. The most useful of these combinations for lithological discrimination is the ratio of one band to another (that is, band A divided by band B). The ratios can theoretically produce values from zero to infinity but because of the restricted range of pixel values in most images ratios rarely fall outside the range of $^1/_4$ to 4. These ratios are then scaled into the range of 0-255

for display. This may be completed by setting values of less than unity to values of 0-127 and values of greater than unity to the range of 129-255.

The most important advantage of a ratio image is that the spectral signature curve of the particular surface material is accentuated. If the bands cover peaks, or absorption troughs, or changes in slope of the curve they can be combined in pairs to enhance the subtle spectral response of the material. In LANDSAT MSS for example, bands 5 and 7 show vegetation as dark and light respectively (the so called red edge). In a standard false colour composite vegetation will stand out as red. However, variations in vegetation density and type are lost. Ratios of these two bands show small changes in these parameters because the amount of vegetation has a large effect on the ratio.

A second major advantage of band ratioing is the reduction of shadow effects. Because of topographic slopes in a scene a lithology may appear in different tones due to shadow effects. The amount of shadow should be the similar in all bands, therefore a ratio image of the same lithology should show similar tone no matter what the illumination (ie the shadow divides out). In practice this is not always the case because the spectral response of the material is subtly different in shadow than that of the same material in direct illumination. Nevertheless, a ratio image does reduce the effects of uneven lighting caused by slope and shadow.

A disadvantage of band ratioing is that it enhances noise, this is because noise is uncorrelated with the data set. This gives rise to erroneous values in the numerator or the denominator of the ratio which in turn produces extreme values for the ratio. A second disadvantage of band ratioing is that it suppresses albedo information (where albedo is the overall ability of a material to reflect radiation of all wavelengths). For example some clay rich rocks such as marls have similar spectral properties to the basic igneous rocks. However, the basic rocks have lower albedo than the marls. In a ratio image the lithologies will appear identical. Clearly in this case a multispectral image is needed to discriminate the features in the image.

Because of the 4 bands on LANDSAT MSS there are only 6 possible ratios (and their 6 reciprocals) these are 4/5, 4/6, 4/7, 5/6, 5/7 and 6/7. These can be combined in various false colour composites of which more than 20 different choices are possible. In order to determine which composite will produce the best discrimination the important spectral features should be decided upon prior to analysis. This can only be achieved by a knowledge of the rocks and the soils in the study area and their spectral response.

Band ratioing has been successfully used to identify rocks containing limonite by Rowan et al. (1974); Goetz et al. (1975); and Blodget et al. (1978). It has been applied to aircraft MSS data by Rowan and Kahle (1982); and Podwysocki et al. (1982). Davis et al. (1982) used band ratios for locating phosphate, gypsum and limestone deposits with LANDSAT MSS imagery of south central Tunisia.

2.4.5 Principal Components Transform

Principal Component Analysis (PCA) (also known as the Kohunen Loeve transform) is a mathematical transformation based on the image covariance or correlation matrix. In this transformation the original n bands of data are projected onto n new principal components. The new axes are calculated by, linear additive combinations of the old bands. The principal axis known as the first principal component (PC1), lies along the line of greatest variance in the scene. The second principal component (PC2) is orthogonal to the first principal component in such a direction to maximize its variance (see figure 2.3). Successive components each have successively less scene variance. Principal components is an analysis technique used to give the investigator a feel for the distribution of data. In a typical LANDSAT MSS scene the first principal component may contain between 90% and 95% of the total scene variance and the fourth principal component (PC4) (last and least component) may have less than 1% of the variance.

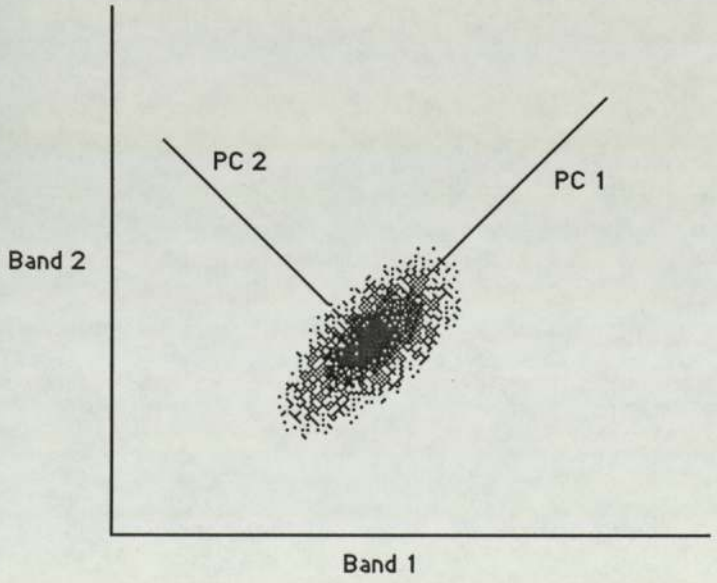

Figure 2.3 To illustrate the principal components transform

Principal components may be displayed in combinations of threes one on each of the colour guns of a video output to produce a false colour composite. The transform can reduce the dimensionality of large multiband data sets (which are becoming increasingly common in remote sensing). Further instead of the limited number shades and hues that characterise most images, principal components with their decorrelated bands give vivid colours. Unfortunately since the statistics of no two scenes are alike, the colours in the image after the transform will not be alike even though identical themes may be present. A further disadvantage is that noise is not correlated with the data set, lower components therefore often have large contributions of noise. Since in the false colour composite each band is given equal prominence the lower components give the scene a noisy appearance.

Despite these drawbacks the principal components transform has been successfully applied to lithological discrimination by many authors including Taylor (1974); Fontanel et al. (1975); Merembeck et al. (1977); Blodget et al. (1978); Blodget and Brown (1982); Jacobberger et al. (1982); Lees et al. (1985); and Fraser and Green (1987);

A technique similar to the principal component transform is called canonical analysis. Here the statistics of the PCA are calculated from small training areas which are indicative of the themes which are to be discriminated, but the transform is applied to whole image. This method was used by Rothery (1985c).

A process known as decorrelation stretching is based on the principal component transform. In this method the new decorrelated axes are computed and some form of contrast enhancement is applied. The data are then projected back onto the original axes so that the original colours of the lithologies are preserved. The scene, however, has a much richer set of colours which makes interpretation easier. This method was applied to LANDSAT TM geological images by Rothery and Francis (1987); and Rothery (1987).

2.4.6 Colour Spaces

Most images are expressed as the three additive primary colours red, green and blue. This is known as the RGB colour co-ordinate system or the RGB colour space. The problem with this colour space is that it is difficult to optimise contrast stretches. Some transformations such as the principal components produce vivid colours but are scene dependent, so that they are not easy to relate to the electromagnetic interactions of the

surficial material. To overcome these problems alternative colour spaces can be considered.

One of the most widely used colour spaces is the Intensity, Hue, Saturation system (IHS). The hue of an object is the average wavelength which it reflects. There are two kinds of hue those like green, yellow and blue which can be found in the visible spectrum (known as the spectral hues) and those such as purples and browns which cannot be found in the visible spectrum (known as non-spectral hues). Saturation is the range of wavelengths around the average wavelength, in other words it is a measure of the pureness of the light. A high value of saturation indicates a single pure colour. Intensity is a measure of the total energy involved in all wavelengths of the reflected light from an object. A high intensity means much light.

Transformation from RGB to IHS space can be performed by rotation of the RGB system co-ordinates to spherical co-ordinates. The IHS system can be thought of as possessing a conical shape, where intensity is the vertical axis, saturation is the distance from the centre of the cone and the hues lie in a radial sequence about the centre of the cone.

Rothery (1987) performs a contrast stretch in IHS colour space and then transforms the data back onto the original axes for the reasons described section 2.4.5. IHS transforms have been used on single band data by using low pass and high pass filtered images of a scene. These can be used together with the raw data to modulate intensity, hue and saturation, thereby producing a coloured image. This was described by Daily (1983) and by Brunner and Veck (1985).

Other colour spaces have been investigated including Taylor colour space where brightness is controlled by PC1. The range of DN of PC2 are assigned hues produced by mixing red (DN=0) and green (DN=255). Hues between blue (DN=0) and yellow (DN=255) are controlled by the DN of PC3 (Drury, 1986a). Munsell colour space is yet another colour space here brightness and colour variations in the image are expressed as brightness, red-greeness and blue-yellowness (ibid.).

2.4.7 Image Classification

This is a technique to define or recognise classes or groups where members have certain characteristics in common. It may be performed manually by the skilled interpreter or semi-automatically by computer. The classes or 'themes' give a thematic

map (although this term has now fallen out of favour as all maps have some theme). In geological terms the classes will be lithologies and the map will be a lithological map. For reasons discussed earlier in this chapter a map produced by remotely sensed data cannot be a true geological map. Two approaches to image classification can be attempted these are (1) supervised, and (2) unsupervised. These will be described in more detail in the chapter 5.

2.5 Summary

Remotely sensed data offers the geologist a viewpoint of features so large that they cannot be seen on the ground and may only be inferred after careful fieldwork. The structural features which are observed on the ground can be placed in their proper regional context by the unique synoptic viewpoint offered by remote sensing. Therefore a better understanding of the regional geology can be obtained

Remotely sensed data are capable of discriminating and even identifying geological materials in favourable circumstances. However, the most commonly used satellites (LANDSAT and SPOT) have poorly positioned spectral bands for geological mapping and therefore only a very limited number of lithologies can be identified. Digital processing of the data can produce good discrimination of rock types. The data cannot be directly used for geological mapping as age data are not present so that stratigraphic units can only be inferred. In the case of the LANDSAT satellite the lack of stereoscopy means that few structural features such as the dip of bedding can be mapped, therefore these data can only be used to produce lithological maps.

Chapter 3
Description of the Study Areas

3.0 Introduction

The study areas used for this project are in the region adjacent to the city of San Jose de Jachal (La Rioja Province) in northwest Argentina. This region was chosen for four reasons. Firstly, because of its semi-arid nature which gives good exposure of lithology. Secondly, conventional forms of fieldwork are both expensive and difficult to carry out because of logistical difficulties. Thirdly, because of the opportunity for analysis of multi-sensor data, as satellite data from three different sources were available for this study. The areal coverage of each data set is shown in figure 3.1. LANDSAT 2 MSS image 249/081, viz. LANDSAT 5 TM quarter scene 232/081 and SIR-A data take 29 (a fuller description of these data is given in chapter 4). The LANDSAT TM scene was available only for the last three months of the project. Finally the region was chosen because of the availability of ground data showing the distribution of lithologies, from the Argentine Geological Survey 1:200 000 series of geological maps and their corresponding bulletins.

The physiography of the region can be split into two parts. In the west of the region there are a series of mountain belts trending north to south, parallel to strike, which reach heights of over 2600 m. These pass eastwards into a great outwash plain (which is at a height of 1400 to 1500 m) covered by recent alluvium, on which the city of San Jose de Jachal is situated. The drainage is dominated by the eastward flowing Rio Jachal (perpendicular to strike) and its tributaries which are parallel to strike.

3.1 Climate and Soils of the Study Area

Canoba (1983) describes the general climate of the region. The area has a mean winter temperature of 8 °C, the summer temperature is 25 °C with variations depending mainly on local topography. The region has in general, very low precipitation, with the mean annual rainfall in La Rioja being 275 mm. The spring is dry and most of the rain occurs in the summer (January and February). The rains are unpredictable and torrential in nature, causing flash floods with great erosive force. The autumn and the winter are dry, the latter being cold, with frosts occurring almost daily between March and August.

The soils of the region are generally granular (stony, stony sandy and sandy) but a thin humic layer can occur in places. Vegetation is small and stunted in size and generally sparse, though it is more common on the higher parts of the mountains.

Figure 3.1 To show the areal coverage of each data set

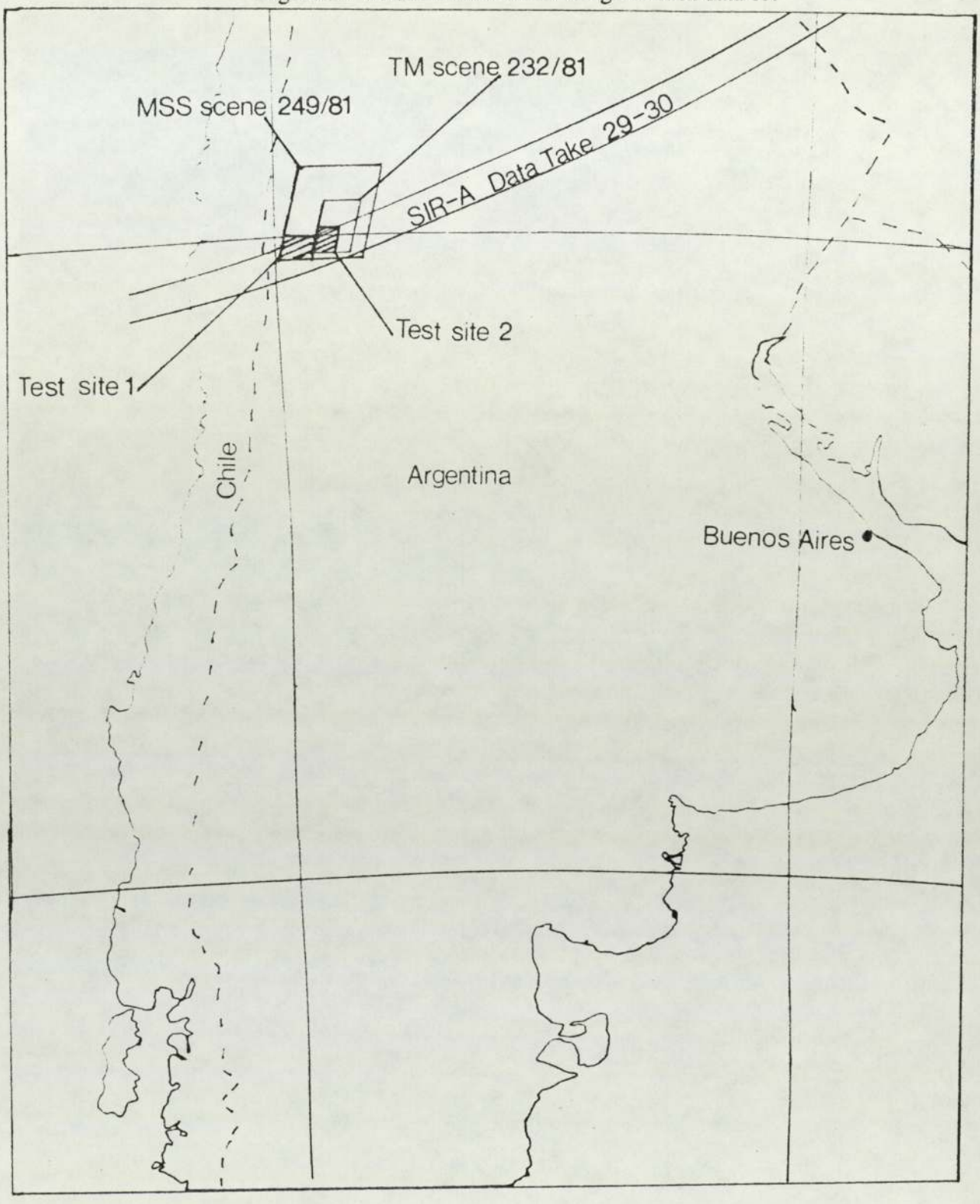

3.2 Description of the Test Sites

The two test sites are close to the city of San Jose de Jachal (see figure 3.1) they are covered by a SIR-A swath (data take 29) and LANDSAT MSS image 249/081. Test site 2 is also covered by TM scene 232/081. In both test sites five different lithostratigraphic units were shown on the geological map. The assumption was made that the published geological maps show the correct distribution and type of lithology, and that the whole area of each test site was represented by only these classes. The possibility that other unrecognised lithologies exist was not taken into account. Classification accuracy is inversely proportional to the number of classes present, therefore the fact that each test site is covered by the same number of lithologies makes the direct comparative tests of classification accuracy possible.

3.3 Test Site 1 Jachal, Provincia de San Juan

Test site 1, lies some 10 km west of the city of San Jose de Jachal, it is covered by sheet 18c of the Argentinian 1:200 000 series of geological maps and the geology is described in the corresponding bulletin written by Furque (1979). Most of the description of the geology of the area which follows is largely abridged from this work. Test site 1 is represented by a number of sedimentary rock types with some pyroclastics, and some basic igneous intrusives. Rocks ranging in age from the Ordovician period to the Quaternary period outcrop in this test site which have been subject to low grade regional metamorphism (with the exception of the Quaternary). The lithological map of test site 1 is shown in map 3.1, plate 3.1 shows the LANDSAT MSS (4, 5, 7) false colour composite of the test site, plate 3.2 is the SIR-A image of test site 1.

Plate 3.1 LANDSAT MSS false colour composuite of test site 1, band 7 displayed as red, band 5 as green and band 4 as blue.

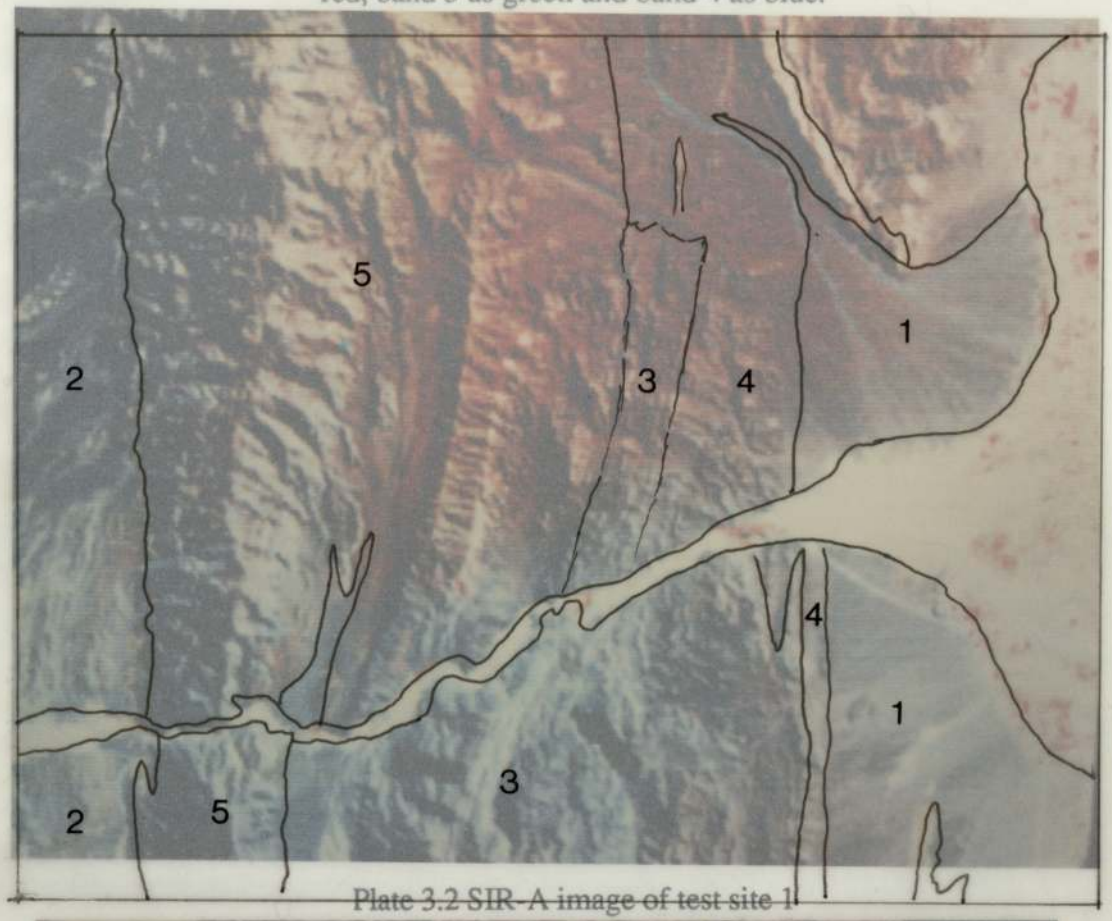

Plate 3.2 SIR-A image of test site 1

Plate 3.1 LANDSAT MSS false colour composuite of test site 1, band 7 displayed as red, band 5 as green and band 4 as blue.

Plate 3.2 SIR-A image of test site 1

3.3.1 Ordovician Yerba Loca Formation

The oldest rocks in test site 1 belong to the Ordovician period and are called the Yerba Loca Formation. The outcrop of this formation extends in a band from the extreme north of the test site, where it reaches a width of 15 km, to the extreme south where its width is less than 3 km. The outcrop forms the mountain range which is called Sierra de Yerba Loca (which gives the formation its name).

The oldest rocks of this formation occur in the western part of the outcrop, consisting of a medium grained conglomerate 2 to 3 m in thickness and composed of rounded quartzite pebbles in a sandy matrix. This passes upwards into coarse, pale grey, sandy quartzites, interbedded with a fissile, finely laminated pale green sericitic argillite which is overlain by thickly bedded, massive quartzites (beds reaching thicknesses of up to 12 m). These beds are strongly resistant to erosion and form distinctive benches. The quartzite is overlain by greywackes of a green and grey-green colour. These are generally fine grained and very compact with many laminations. They increase in both thickness and coarseness towards the south.

Neither the base nor the top of this formation outcrop occur in this area. The formation is slightly fossiliferous yielding graptolites such as Climacograptus, Nemagraptus, Glyptograptus and Dicellograptus. These indicate an age of Lower Caradoc. The rocks have been metamorphosed producing the sericite, which is much more common in the west of the outcrop than in the east. A suite of basic and igneous rocks has been intruded into the formation, coarse gabbros occur in the east, and andesites in the south.

In the LANDSAT MSS false colour composite the formation appears a dark bluish red (probably because of the presence of a thin soil supporting vegetation). The outcrop has an overall very rough, very coarse texture with a strong directional fabric perpendicular to its strike caused by numerous drainage channels. The eastern boundary is sharp and well defined possibly indicating a faulted margin. In the SIR-A image the outcrop is medium to light toned possibly indicating a fine grained rock and it is again the texture fabric is coarse, due to drainage channels perpendicular to strike.

3.3.2 Silurian Tucunuco Group

Rocks of Silurian age occur in a north-south trending strip to the east of the Ordovician

outcrop, in the form of a asymmetrical syncline cut by east-west faulting. This group has been divided into two units which for the purposes of this study have been amalgamated. The rocks are dominantly marine sediments and were deposited transgressively upon the Ordovician.

The lower unit of this group reaches a thickness of 435 m in its type locality, and is composed of lutites and sandy lutites of greenish colour. The sandy lutite is predominant in the upper third of the unit, whilst in the lower two thirds abundant pale to dark brown calciferous bands 0.2 - 0.5 metres in thickness occur, which can yield well preserved fossils of Wenlockian age.

The upper unit consists of three parts. The lowest is composed of unfossiliferous green lutites with some lenticular intercalations of quartzite (this part is up to 250 m thick). The central part is made up of lutites of pale grey-green to dark green colour with many sandy intercalations. These intercalations are thinner than in the lower part of the formation and can be highly fossiliferous. The top third part of the group consists of quartzites and sandy quartzites of maroon colour which alternate with thin green lutite bands which yield scarce brachiopods.

In the LANDSAT MSS standard false colour composite this formation has a pale blue to light red colour, and is characterised by relatively subdued topography with medium to fine texture and some fabric parallel to strike. The group has well defined boundaries in the north and less well defined boundaries in the south on the SIR-A image. The texture of this rock group is much more random than that of the Ordovician in both the MSS and SIR-A imagery.

3.3.3 Devonian Talacasto Formation

The lower part of the formation is composed of calcilutites of grey-green to greenish-red colour, with intercalations of fine brown and green sand. In some localities intercalations of conglomerates and calcareous, fossiliferous concretions occur. The presence of an abundant marine fauna in the older rocks of this formation give a lower Devonian age to the rocks. The middle part of the formation is composed predominantly of lutite which has a grey-blue colour and reaches a thickness of 400 m. The upper part of the formation is composed of finely stratified lutite, limestones and sandstones of greenish grey colour. The lutites alternate with fine sandstones and greywackes, of light grey colour and reach a thickness of up to 200 m. These upper beds have a scarce fossil content because of the increasing continentality of the

depositional environment. The overall thickness of Devonian sediments in this test site is some 1000 m.

The LANDSAT false colour composite shows this formation to be light blue in colour, indicating little vegetation. The formation has a very coarse, medium texture with little discernible fabric. In the SIR-A image the formation has very indistinct boundaries and very variable tone ranging from very pale to very dark. The texture is coarse dominated by the reflections from drainage channels.

3.3.4 Tertiary El Corral Formation

The Tertiary sediments of this test site occur in a basin to the west of the Yerba Loca mountain range. The lowest part comprises reddish-violet fanglomerates composed of fragments of extrusive igneous rocks, especially andesites. Lenticular beds derived from Ordovician grey limestone and crystalline basement complex occur in places. In the basal levels some sandstones interbedded with tuffs occur, these diminish rapidly in the upper levels. Beds of gypsum are also present in places. The presence of a brownish-green lutite sequence yielding a gastropod fauna which has a Tertiary age is noted by Cuerda (1963). The middle and upper units of the formation consist of thickly bedded lenticular conglomerates which pass laterally into fine dark brown sandstones. The conglomerate is mainly composed of rounded pebbles of crystalline basement but in places Ordovician limestones become the chief constituent.

Because of the scarcity of fossils in this lithology the age of the rocks can not be given accurately, however, it is accepted that the lower part of the formation is of Pliocene age.

In the LANDSAT MSS image the Tertiary sediments appear dark because they occur on west facing slopes which are not illuminated. Bands 5 and 6 show relatively higher reflectance than the other two bands, possible due to presence of ferrous bearing minerals or weathering products. The sediments have a very coarse, very rough texture, characteristic of conglomerate (see plate 3.1).

3.3.5 Quaternary Iglesia Formation

Superficial cover of Quaternary age is of great importance in this region as it is very areally extensive. The formation is principally composed of alluvial fans (debris cones) and valley alluvium dominated by thickly bedded conglomerates of light green to green

yellow colour, composed of rounded pebbles of sandstone and quartzite. The formation occurs in fans which flank the mountain belts.

In the LANDSAT MSS image the formation appears pale blue to pale red and fine grained with a smooth homogeneous texture. In the SIR-A image the formation has a fine smooth texture with no directional fabric. The formation is light to medium toned with distinct boundaries.

Map 3.1 Lithological map of test site 1

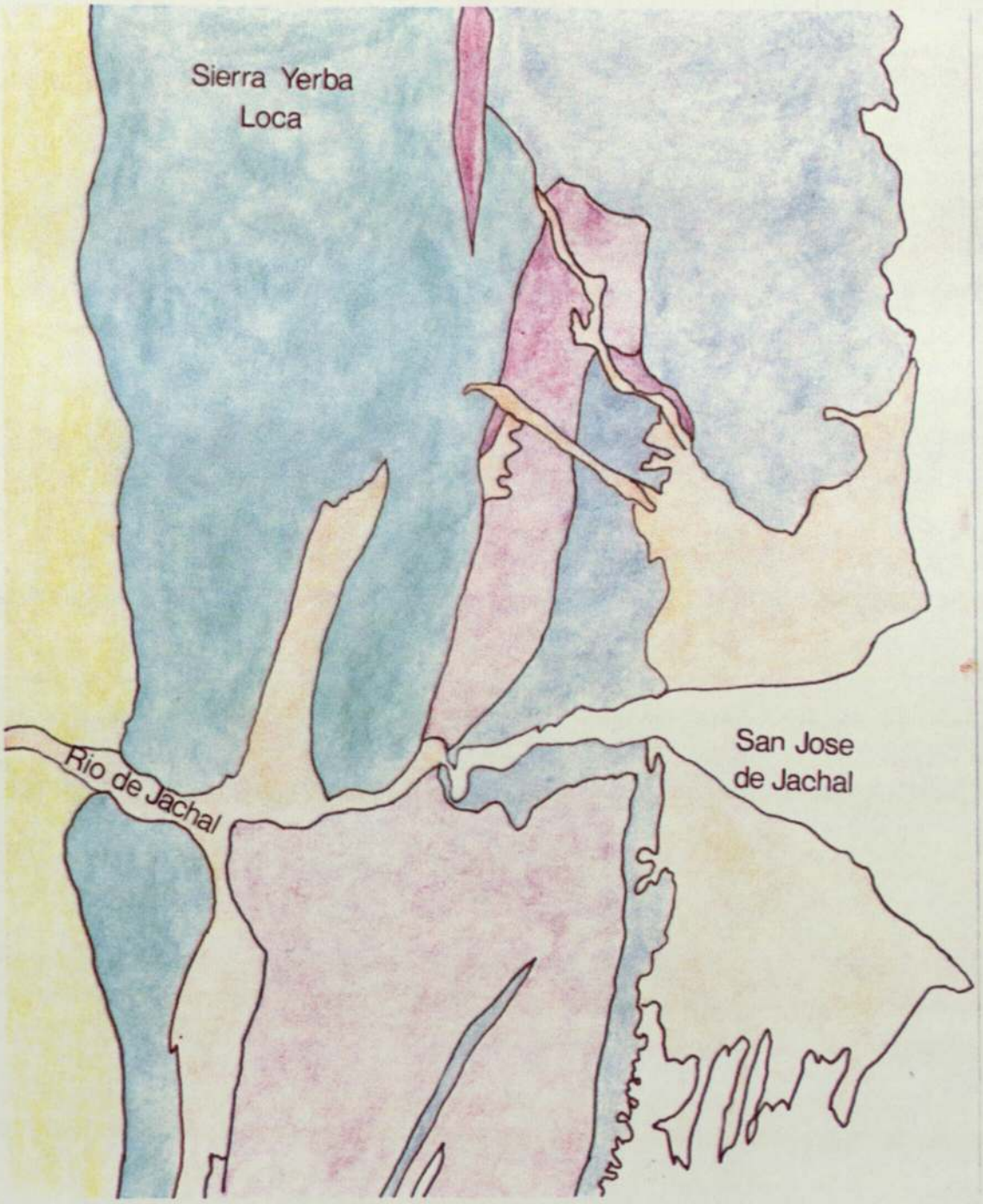

Legend

- Class 1 Alluvium
- Class 2 Conglomerate
- Class 3 Conglomerate/Sandstone
- Class 4 Sandstone/Siltstone
- Class 5 Greywacke/conglomerate

Table 3.1 Summary of the Geology of Test site 1

ERA	PERIOD	FORMATION	LITHOLOGY	SETTING	THICKNESS	CLASS
CENOZOIC	Quaternary	Iglesia	Alluvium	Continental	10-50 m	1
	MAJOR UNCONFORMITY					
	Tertiary	El Corral	Sandstone/ Conglomerate	Continental	800 m	2
	MAJOR UNCONFORMITY					
PALAEOZOIC	Devonian	Talacasto	Calcipelite/ Sandstone/ Conglomerate	Marine	1000 m	3
	Silurian	Tucunuco (undivided)	Lutite/Sandy Lutite/Sand	Marine	500 m	4
	Ordovician	Yerba Loca	Sericite/ Lutite/ Greywackes/ Conglomerate	Marine	200 m+	5

3.4 Test site 2 Cerro Rojado

Test site 2 is 100 km west of San Jose de Jachal and is covered by sheet 17c of the Argentinian 1:200 000 series of geological maps and by its corresponding bulletin Gentili (1972), it updates the earlier work of Frenguelli (1948) and is shown in map 3.2. The description of lithologies which follows is taken from the bulletin and the map. As in test site 1 some five lithologies occur within the test site, ranging in age from the Triassic to the Quaternary, these are predominantly sedimentary in origin.

The physiography of the area is dominated by a mountain chain; the Sierra Morada trending north-northwest to south-southeast. Summits reach heights in excess of 1800 m. The drainage is dominated by the southward flowing Rio del Bermejo and the northward flowing Rio del Alto. The Sierra Morada is dominantly composed of Triassic strata, and a fault bounded plateau to the east of the Sierra is composed of Palaeozoic sediments mantled by Quaternary sediments. The intermediate area is covered by Quaternary fluvial sediments. West of the Sierra Morada the ground is again mantled by Quaternary sediments which obscure the underlying Tertiary sediments. Plate 3.3 is the MSS false colour composite of test site 2, plate 3.4 is the

SIR-A of the test site, and plate 3.5 is the TM false colour composite of test site 2.

Plate 3.3 LANDSAT MSS false colour composite of test site 2, band 7 displyed as red, band 5 as green and band 4 as blue.

Plate 3.4 SIR-A image of test site 2

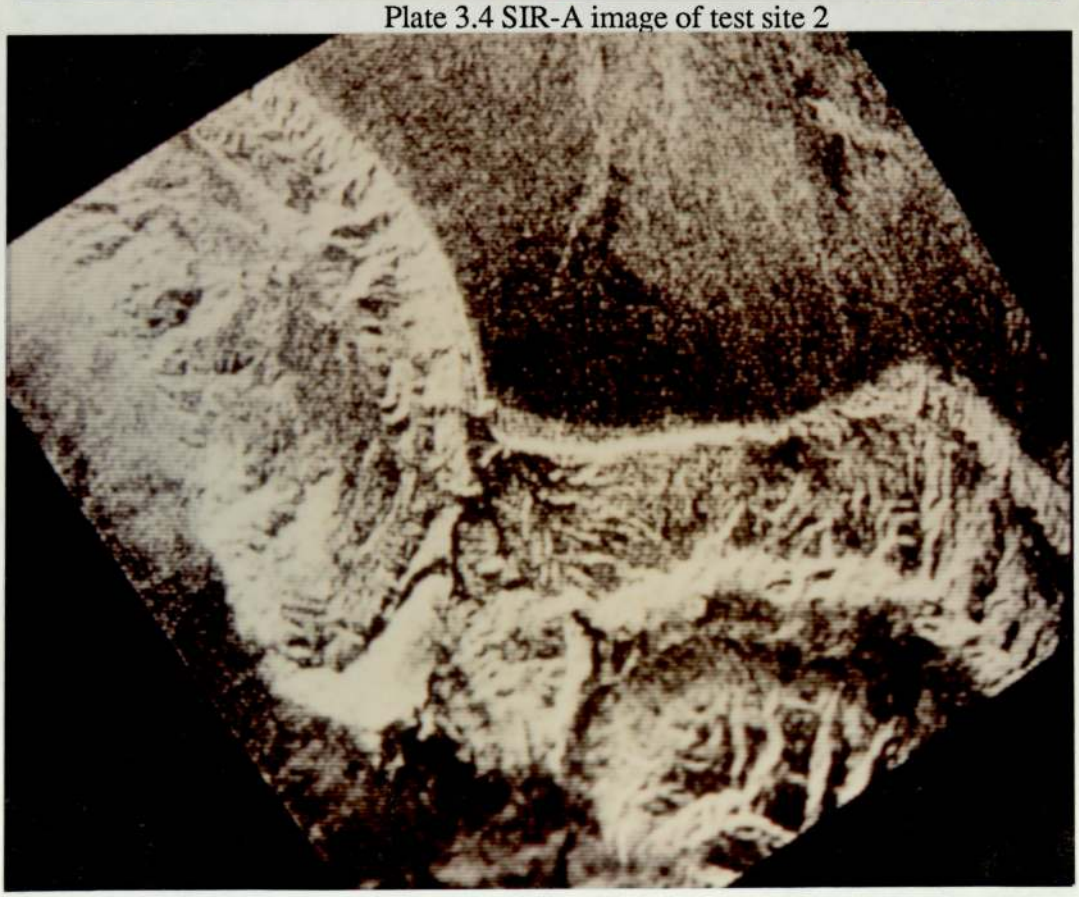

Plate 3.5 LANDSAT TM false colour composite of test site 2, band 7 displayed as red, band 5 as green and band 2 as blue.

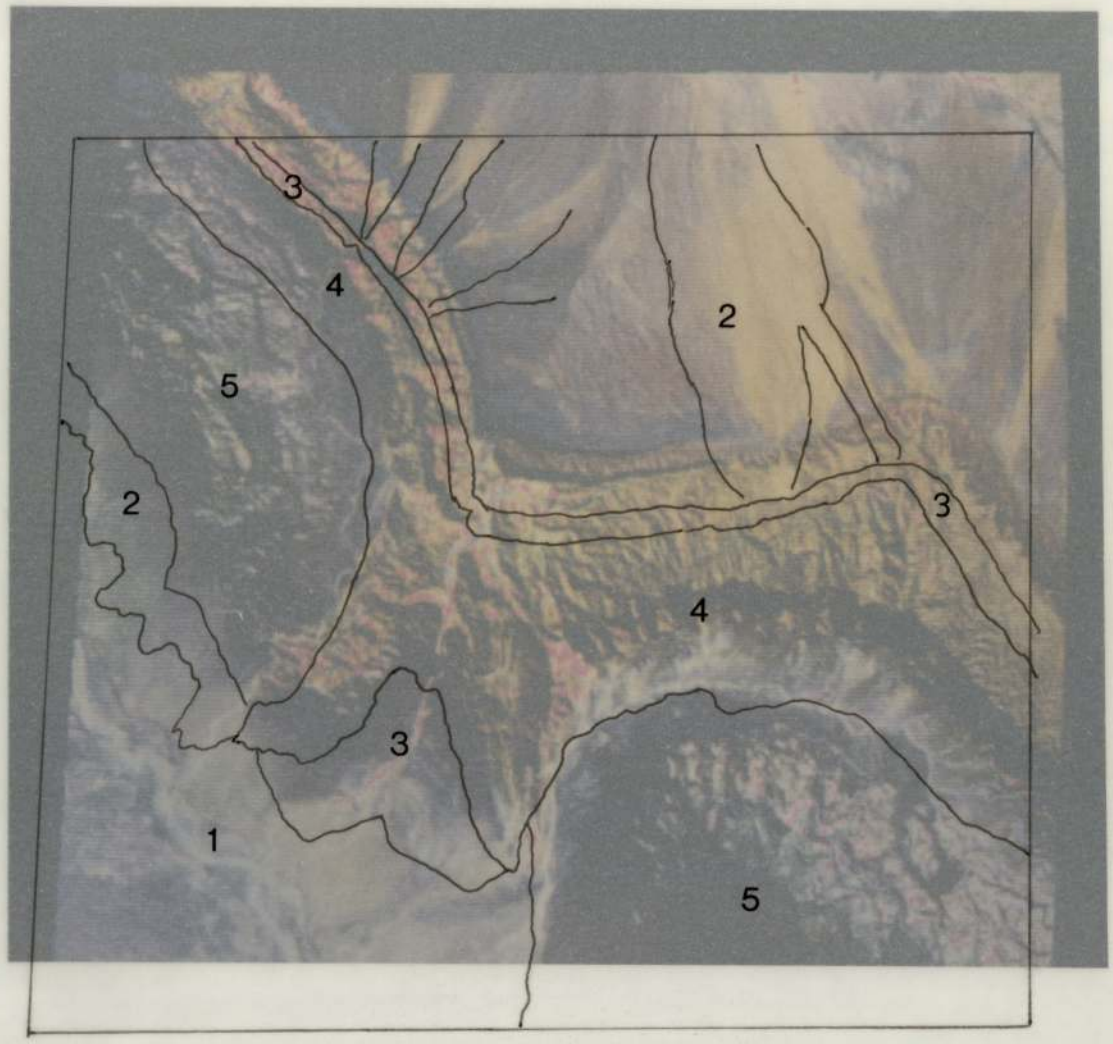

Plate 3.5 LANDSAT TM false colour composite of test site 2, band 7 displayed as red, band 5 as green and band 2 as blue.

3.4.1 Middle Triassic Series

This unit corresponds with a number of divisions which Frenguelli called "Estratos de Ischichuca, Los Rastros and Ischigulasto". The unit constitutes a thick series of sediments (over 1500 m in thickness), beginning with a basal conglomerate which lies unconformably upon Lower Triassic sandstones. The outcrop forms a major part of the Sierra Morada in an anticlinal structure at the centre of this test site.

The series is composed of two units. The lower unit is composed of a sequence of sandstones, sandy conglomerates and conglomerates with a complex bedded texture. The basal conglomerate is similar in morphology to an ancient alluvial fan. The conglomerate is made up of rounded volcanic clasts, especially basalts and porphyry. The larger clasts generally occur towards the base of the series. Towards the upper part of the series the member grades into a predominantly sandy lithology with siliceous matrix of a grey-green colour.

In the upper unit, abundant carbonaceous and clay intercalations occur in which the clay bands reach thicknesses of up to 500 mm. The carbonaceous bands are in the form of sub-bituminous coal seams with a high clay content and a lenticular form. The coal seams are not of any commercial value.

The total thickness of the Middle Triassic in this test site is in excess of 1500 m.

The formation has a dark reddish to purple colour in the LANDSAT MSS false colour composite, with coarse texture. The SIR-A image shows the lithology as medium toned. The texture is coarse and in places is formed from V shaped en echelon shapes which are due to layover effects, resulting from very steep sided hills facing in the direction of the receiver.

3.4.2 Upper Triassic Series

The Upper Triassic corresponds to the series which Frenguelli (1948) called "Estratos de Gualo". The series forms three subparallel outcrops. The outcrops form an extensive asymmetrical fold with an anticlinal structure. The western limb of this fold is cut by a major reverse fault which runs north-northwest to south-southeast across the region. The fault disturbs Triassic and Tertiary rocks, and in places the Triassic rocks have been intruded by basic igneous rocks along the line of this fault and its related

subparallel faults.

The rocks of the Upper Triassic sit concordantly upon the Middle Triassic and pass gradually from one to the other, with levels of conglomerate becoming abundant in the transition zone. The middle part of series is made up of friable sandy sediments which are predominantly brick-red or brown in colour. In general the sediments are fine grained, cemented with iron based minerals which give the rocks their distinctive colour. Intercalations of strata with a siliceous cement form resistant beds up to 30 m thick, massive in character producing a distinctive landform. In the siliceous parts of the sequence the reddish colouration changes to a yellowish grey colour.

In the fold north of Cerro Rajado, the Upper Triassic Series strike is predominantly northwest to southeast, with a dip of 30- 40 degrees in a north easterly direction. The total thickness of Upper Triassic sediments is in the region of 400 m.

The formation appears pale yellow to dark yellowish green in the LANDSAT MSS false colour composite. The rock displays a coarse, rough texture with some alignment perpendicular to strike. In certain places, especially east facing slopes, the texture becomes very coarse, being picked out by well defined stream courses. In the SIR-A image the formation has very variable grey tone caused by irregular topography and giving rise to a very rough texture. The texture on many of the river valleys which cut this outcrop being due to the favourable alignment of reflectors toward the radar.

3.4.3 Tertiary

The outcrop of the Tertiary trends northwest across the region to the southeast, in the form of a major asymmetric syncline. The lower part of the succession is a basal conglomerate which lies unconformably upon the rocks of the Upper Triassic with a strongly angular unconformity. The upper part of the succession is a series of interbedded sandstones, limestones and volcanic tuffs. The sandstones are fine grained with a reddish-grey to green colour. The upper part of the succession is made up of granular with a scant cement which forms the so called "rotten ground".

The Tertiary rocks form a girdle to the east of the Sierra Morada mountain range. The middle part of the succession is characterised by the presence of sandstones and limestones of reddish brown colour. The upper part of the Tertiary is not present in test site 2. The total thickness of Tertiary sediments in test site 2 is over 2000 m.

In the LANDSAT MSS imagery, the Tertiary rocks appear dark yellowish grey with fine smooth texture and some fabric running perpendicular to strike. In places the texture becomes much coarser as it is picked out by well defined stream courses.

3.4.4 Quaternary

The Quaternary rocks are directly related to the outcrops of rocks in the mountainous country, the sediments occur in alluvial fans (or debris cones) and as alluvial cover. On the eastern side of the Sierra Morada the sediment is derived from basalt and rounded sandstone clasts. On the western side of the Sierra, the debris cones are formed of calcareous sediment, with rounded pebbles of limestone. The debris cones are very variable in thickness, while the alluvial cover forms thicknesses of 10 to 50 m.

The debris cones appear light grey to purple with some yellow cones, with the colour dependent on the provenance of the parental material. The texture is fine grained, homogeneous with a strong salt and pepper effect.

The texture of the alluvial deposits is fine and smooth on both the LANDSAT MSS imagery and the SIR-A imagery. The colour is relatively inhomogeneous ranging from grey purple to yellow and white where saline minerals locally become abundant.

Map 3.2 Lithological map of test site 2

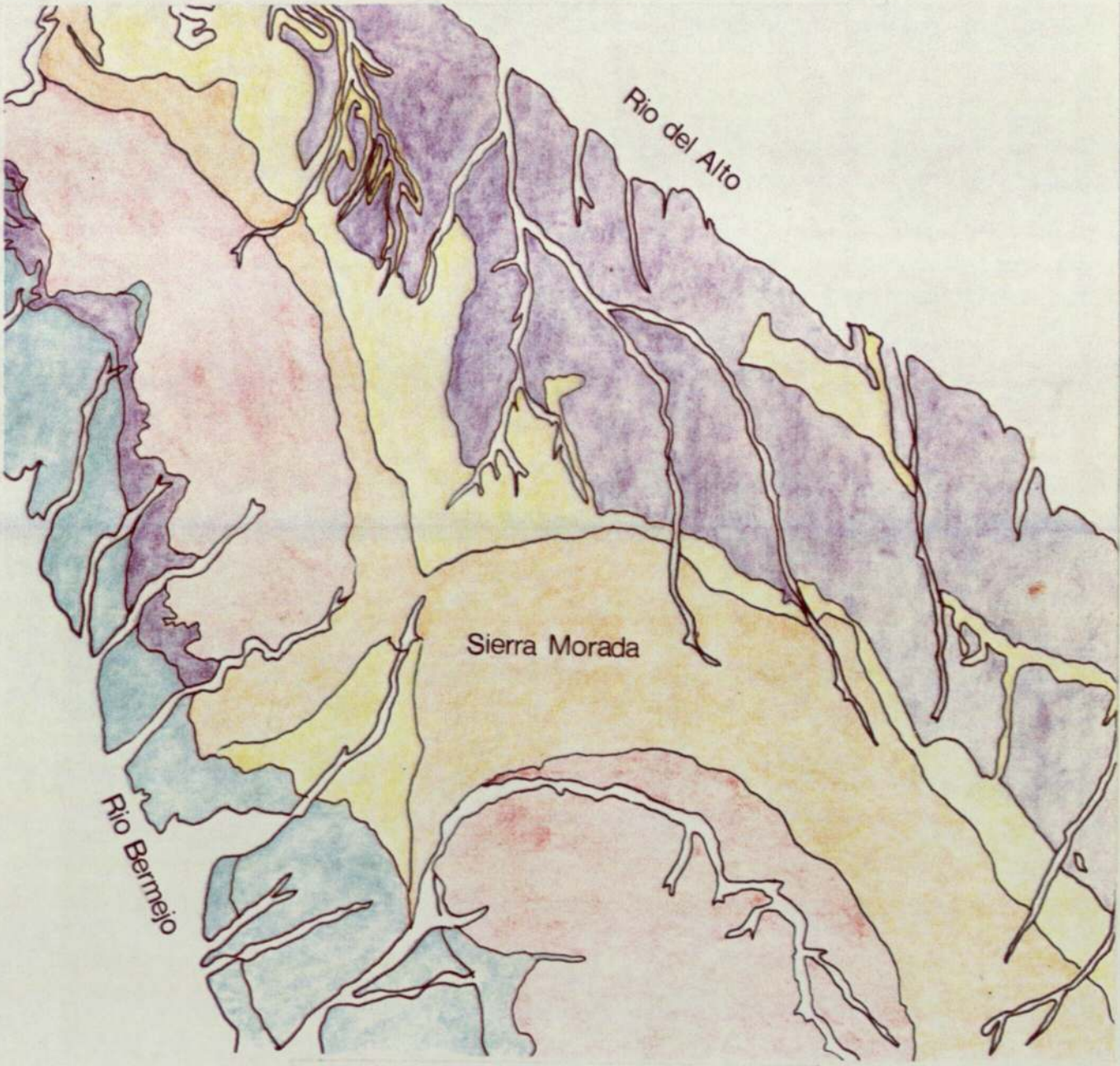

Legend

- Class 1 Alluvium
- Class 2 Alluvial Fan
- Class 3 Sandstone/limestone
- Class 4 Fine Sandstone
- Class 5 Sandstone/conglomerate

Table 3.2 Summary of the Geology of test site 2.

ERA	PERIOD	FORMATION	LITHOLOGY	SETTING	THICKNESS	CLASS
CENOZOIC	Quaternary		Alluvium	Continental	10-50 m	1
			Alluvial Fans	Continental	Variable	2
	UNCONFORMITY					
	Tertiary	Undivided	Sandstone/ Limestone/ Tuff	Continental	2,500 m	3
	MAJOR UNCONFORMITY					
MESOZOIC	Triassic	Upper	Fine red sandstones	Marine	400 m	4
		Lower	Sandstone/ Conglomerate/ Limestone	Marine	1,500 m+	5

3.5 Photomorphic Mapping of Lithologies

The photomorphic attributes of a class may be used to characterise its lithology. In the following section some the photo characteristics used by manual interpreters will be described and discussed.

3.5.1 Photomorphic Interpretation of Test site 1

The formation Yerba Loca (class 5) in test site 1 is composed of sandstones, conglomerates and greywackes. These have a dark tone and a very coarse, very rough texture. The dark tone is probably due to the presence of the greywackes in the sequence. The overall very coarse, very rough texture being due to the resistance to physical and chemical weathering of the lithology and its coarse grain size which in turn gives the outcrop strong positive relief and hence a rough texture.

The Tucunuco Group (class 4) is composed of thinly bedded quartzites and green siltstones. This lithology is medium toned, the texture has a fine, medium roughness, this is due to the moderate resistance to erosion of this lithology giving moderate relief and hence only moderate image texture.

The Talacasto Formation (class 3) is composed of conglomerates interbedded with fine grained red and green sandstones. The lithology has overall a light tone and this is probably due to the presence of iron bearing minerals in the rocks which give the rocks high reflectance in bands 5 and 6 of the LANDSAT MSS. The texture is very coarse, with medium roughness, the coarse texture is due to widely spaced river channels, which are in turn due to the well drained nature of the sediments. The medium rough texture is a property of the moderate resistance to erosion of the lithology, which gives rise to a moderate topographic expression.

The El Corral Formation (class 2) is an unconsolidated alluvial (mainly conglomeratic) sediment which forms alluvial fans. The lithology has overall medium tone which is due to it being composed of a mixture of all the consolidated lithologies. The texture is relatively fine and smooth, so called 'salt and pepper' texture. This is caused by a lithology made up of rocks derived from a variety of different sources.

The Iglesia Formation (class 1) is a river valley alluvium which is medium to dark in tone and has a very coarse texture. The dark tone is at first somewhat surprising (an average medium toned would be expected), but may be due in part to the lithology occurring at the base of mountain slopes, where it is at least partly in the shadow of the surrounding mountains.

3.5.2 Photomorphic Interpretation of Test site 2

The Middle Triassic of test site 2 (class 5) is composed of conglomerates and sandstones (composed of intermediate volcanics) interbedded with limestones. The lithology has an overall light tone with a medium, smooth texture. The intermediate volcanics are likely to have weathered to the bright reds and purples which are characteristic of these lithologies. This colouration is due to the break down of their ferromagnesian content, and gives the lithology a high reflectance in bands 5 and 6 of LANDSAT MSS, and hence the overall relatively light tone. The fine smooth texture may be due to the interbedded nature of the lithology, the limestone beds being liable to chemical erosion, and hence produce a subdued topography and smooth image texture.

The Upper Triassic (class 4) is composed of red fine grained sandstones and minor basaltic intrusions. The lithology is light toned and the texture is coarse with a medium roughness. The high reflectance is probably due to the red sandstones having high reflectance in bands 5 and 6 of the LANDSAT MSS, the basaltic intrusions must not

contribute a significant part to the tone, otherwise a much darker lithology would be expected. The texture is similar to the Middle Triassic, which is unsurprising, since sedimentation continued uninterrupted from the Middle Triassic to the Upper Triassic.

The Tertiary (class 3) is represented by a light to medium toned series of fine sandstones interbedded with limestones and tuffs (of intermediate composition). The overall light tone is characteristic of both sandstones and limestones, the tuffs will probably cause the slight darkening of this lithology. The texture is fine grained and rough which is probably due to the relatively fine grained nature of the sediments and their wide compositional differences, giving rise to differential erosion rates and hence a rough texture.

The Quaternary alluvial fans (class 2) are dark toned and very fine, very smooth texture. The dark tone is almost certainly due to them occurring at the foot of mountains and therefore in their shadow. The fine texture is probably due to the low spatial resolution of the imagery, it is also probably an effect of the shadow.

The Quaternary river alluvium (class 1) is a medium toned lithology with a very coarse grained, very smooth texture. The tone is to be expected as it is made up of a mixture of all the consolidated sediments in the region. The smooth texture is due to the sediment forming on a monotonous peneplain

3.5.3 Definition of Training Areas

Five training areas were defined for each of the test sites, one for each class. In addition five verification sites (one for each class) were defined for the purpose of measuring the classification accuracy (see chapter 5). The training areas and verification areas were chosen to be in different parts of the class outcrop. Both training areas and verification sites were in the form of large contiguous areas so as to obtain an accurate representation of the texture of each class.

3.6 Summary

Two test sites in semi arid northwest Argentina have been identified for which multisensor data are available. The landscape and lithologies present in both the test sites has been described. Test site 1 has a suite of rocks dating from the Palaeozoic, to recent alluvium. The test site is dominanted by sedimentary lithologies, but with some pyroclastics. Low to medium grade regional metamorphism has affected all lithologies

(with the exception of the Quaternary) to a greater or lesser extent. Test site 2 is dominated by rocks which are comparatively young in age (Middle Triassic to Quaternary). A wide variety of sediments occur and well defined folds are present which affect the structure of the lithologies present in this test site.

The photomorphic attributes of each lithology (that is, the tone and texture of each lithology) can be explained in terms of the composition and structure of each lithology. For example, alluvial fans which occur in the shadows of mountain belts are likely to be darker toned than alluvium occurring in an outwash plain. And coarse grained, quartzose sediments are more likely to form coarse textures than fine grained, pelitic sediments.

Chapter 4
Image Data

4.0 Introduction

The three separate types of satellite imagery used for this study namely LANDSAT MSS, TM and SIR-A and their characteristics are described in this chapter. Also discussed are the pre-processing steps carried out to produce all the images in the same co-ordinate system. The two test sites in northwest Argentina used in this study are shown figure 4.1. Finally a principal components analysis is undertaken in each of the two test sites and the results are discussed.

4.1 LANDSAT MSS Data

The characteristics of LANDSAT MSS are well described in Watkins and Freden (1979) and in Short (1982), some points should be noted. The MSS has four bands named 4, 5, 6 and 7 on LANDSAT's 1, 2 and 3, but these are called bands 1, 2, 3 and 4 on LANDSAT's 4 and 5. The bands correspond to the 0.4-0.5 μm, 0.5-0.6 μm, 0.6-0.7 μm and 0.7-1.1 μm regions of the electromagnetic spectrum respectively. The instantaneous field of view in all bands is 80 m by 80 m, the pixels are sampled by the sensor at the rate of approximately 56 m in the across track direction and 79 m in the along track direction. Since the average image is 185 km by 185 km the average number of pixels in an image is 3240 in the x direction by 2340 in the y direction. The data are quantised to six bits; that is 64 grey levels (a scale of 0 to 63), bands four five and six are then scaled to seven bits (0 to 127), while band seven is left as six bit data.

The LANDSAT MSS scene used for this project was a LANDSAT 2 scene 249/081 acquired at Sioux Falls, South Dakota on 5th October 1975, with a solar elevation of 44 degrees and a solar azimuth of 063 degrees. The image is centred on a point 68 degrees 37 minutes west by 30 degrees 8 minutes south, which covers a large part of north west Argentina and northern Chile (see figure 4.2). Plate 4.1 shows a standard false colour composite of the full scene (that is, band 4 displayed as blue, band 5 displayed as green and band 7 displayed as red). The red area in the scene centre is the city of San Jose de Jachal, in the far western part of the image the white snow capped mountains of the high Chilean Andes are visible.

Figure 4.1 Location of test sites

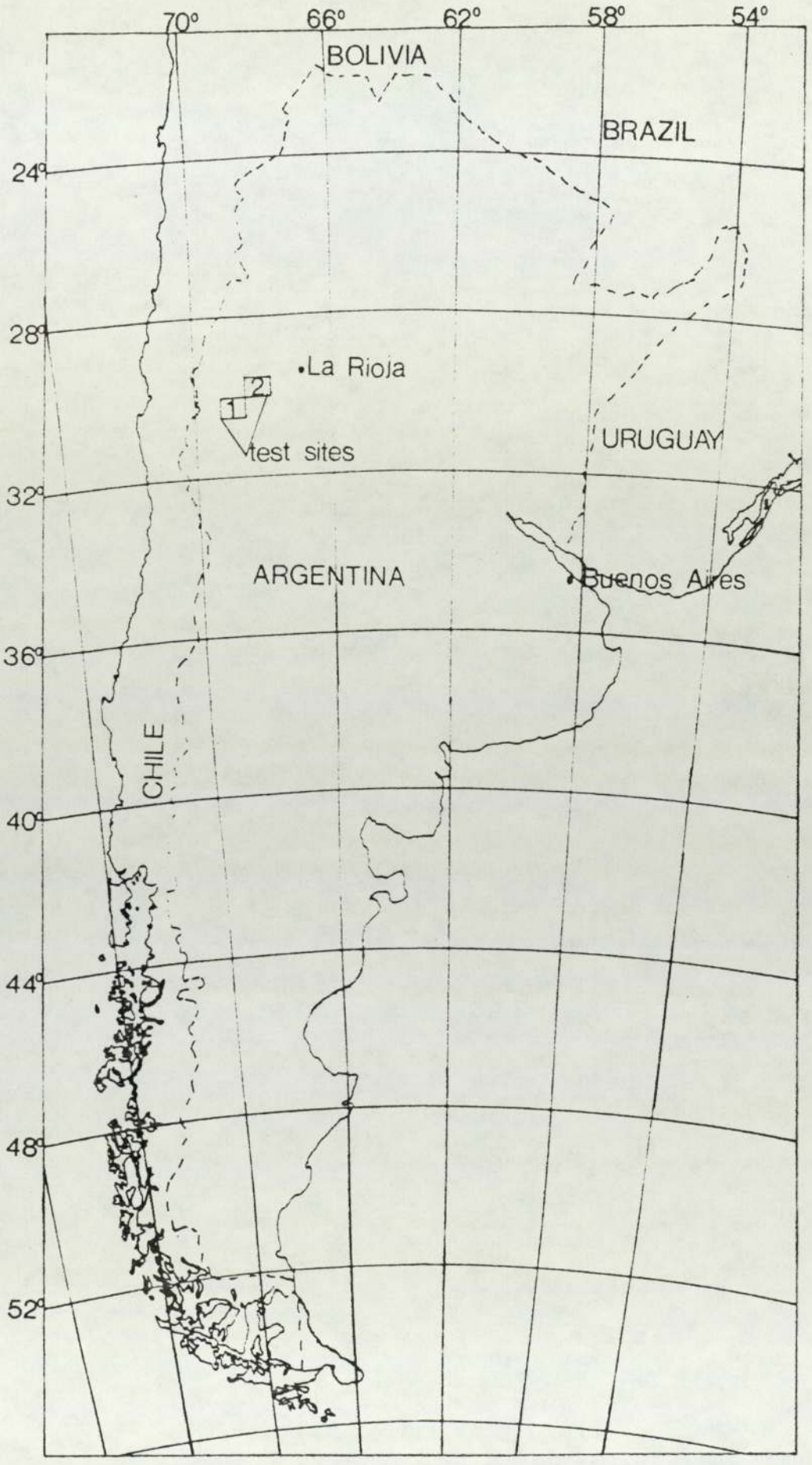

Plate 4.1 LANDSAT 2 MSS false colour composite of scene 249/081

Plate 4.1 LANDSAT 2 MSS false colour composite of scene 249/081

4.1.1 Pre-processing of LANDSAT MSS Data

Because of the sensor characteristics of LANDSAT MSS imagery certain pre-processing of the data is necessary. The pre-processing used in this study was of three sorts; the first part involved replacing missing lines (or dropped lines). The second part of the pre-processing involved making the rectangular pixels of the image square, the final part was to deskew the image.

Missing lines are caused when the MSS sensor fails to record data for part of a particular scan line. They can be simply removed by replacing the missing line by the average of the pixel above with the pixel below the missing line. Some six missing lines had to be removed in this way. To square the image some 900 lines must be added (because the average image has 3240 pixels by 2340 lines). It has been suggested that the lines may be added by the formula given in equation 4.1 (Hord, 1982).

3 LI , 1 N , 3 LI , 1 N , 2 LI, 1 N, 3 LI, 1 N , 2 LI, 1 N *equation 4.1*

Where LI is a line of image and N is an added line.

This has the effect of giving the image approximately square pixels with nominal dimensions of 60 m by 60 m. This has two advantages, firstly when the image is viewed, the horizontal dimension is the same scale as the vertical scale. Secondly the 60 m pixels can easily be registered with TM imagery which has 30 m by 30 m pixels. The second part of the pre-processing, that is the deskewing of the image, is necessary because the image takes 25 seconds to acquire and the earth rotates below the sensor so that the area imaged on the ground is not a square but a parallelogram. The amount of skew is latitude dependent, but at many latitudes the skew is approximately constant, and can be modelled by a standard shift. A simple algorithm was used to correct the imagery by offsetting each group of 12 lines by an extra pixel. This means that image base is a full 270 pixels offset from the top of the image, and the image has a total width of 3509 pixels. After this pre-processing the image can be used as a base map at scales of up to 1: 250 000 (Mather, 1987). This MSS image was then used as the base map on which to coregister the other data sources.

4.2 LANDSAT TM Data

The LANDSAT 5 TM 232/081 used in this study was a quarter scene (quadrant two) acquired by EOSAT on 27th April 1986, the location of the TM data are shown in figure 4.2. The characteristics of the data are well described in Engel and Weinstein (1983) and a special issue of the IEEE transactions of Geoscience and Remote Sensing (1984), but some points should be noted here. The sensor has seven bands stretching from blue wavelengths of the electromagnetic spectrum to the thermal infra red. The sensor includes a band which covers the middle infra red (2.08 μm- 2.35 μm). This band was placed on the sensor by the recommendation of geologists on the GEOSAT working committee, this is because of the clay absorption features which occur in this part of the electromagnetic spectrum (Rothery, 1983). The TM data has square pixels with a resolution of 30 m in the six reflective bands, that is bands 1 to 5 and band 7: band 6 (the thermal infra red band) has a resolution of 120 m. The data are quantised to eight bits (0 to 255). The orbit of LANDSAT 5 is similar to the orbit of LANDSAT 2 in that it is sun synchronous. The altitude of the orbit of LANDSAT 5 is 700 km (compared with 900 km for LANDSAT's 1, 2 and 3), the repeat cycle is therefore 16 days compared with 18 days of LANDSAT 2.

Malila et al. (1984) listed the following differences of TM data over MSS data acquired by LANDSAT's 1, 2 and 3.

Spatial Specifications

a) 30 m resolution versus 80 m resolution.
b) Improved platform stability.

Spectral Specifications

a) Narrower spectral bandwidths.
b) Additional spectral regions (blue-green, middle infra red, thermal infra red).

Temporal Specifications

a) Repeat cycle of 16 days versus 18 days.
b) Repeat coverage of overlap zone (seven days versus next day).

Radiometric Specifications

a) Improved signal to noise ratio.
b) Increased dynamic range (eight bits versus six bits).

4.2.1 Geometric Rectification of TM data

Registration of LANDSAT TM data to MSS was achieved by interpolating the MSS onto a 30 m by 30 m grid (so that the pixels of the MSS scene were of the same size as the pixels of the TM). A number of control points (common to both images) were then selected and registration was achieved using a least squares model of the form

$$X = A + Bx + Cy + Dxy \qquad \textit{equation 4.2}$$

$$Y = E + Fx + Gy + Hxy \qquad \textit{equation 4.3}$$

where X and Y are the new pixel co-ordinates; x and y are the original pixel co-ordinates and A, B, C, D, E, F, G and H are constants. The registration was achieved using eight ground control points and this yielded a root mean square (RMS) error of 0.85 pixels, or about 25 m (see table 4.1).

Table 4.1 To give the control points for the least squares model for geometric rectification of LANDSAT TM to LANDSAT MSS data and the associated errors.

POINT	REAL X	REAL Y	PRED X	PRED Y	ERROR
1	209.0	135.0	209.6	135.9	0.5
3	422.0	121.0	421.9	120.1	0.9
4	389.0	216.0	389.3	217.1	1.1
5	431.0	232.0	431.0	232.7	0.7
6	234.0	320.0	232.8	319.8	1.2
7	362.0	357.0	362.4	356.2	0.9
8	71.0	327.0	71.5	327.2	0.6

RMS ERROR FOR WHOLE SET IS 0.9 PIXELS

Table 4.2 To give the equation coefficients for the least squares model for geometric rectification of LANDSAT TM data to LANDSAT MSS data.

EQUATION COEFFICIENTS	
X	Y
-29.4	-74.5
1.0	2.8E-02
2.6E-02	1.0
-4.0E-05	-5.8E-05

This RMS error was felt to be satisfactory in the absence of man made features to use as ground control points. The second order model seems to be satisfactory because of

the good visual match between the coregistered scenes. A nearest neighbour interpolation was used in order to maintain the radiometric fidelity of the data.

4.3 Radar Data

The details of radar are probably less well known than those of passive sensors such as LANDSAT MSS and TM, but are well described by Trevett (1986), and some points should be noted here. The name of the radar data used in this research is Shuttle Imaging Radar (or SIR-A) this is a synthetic aperture radar (SAR), which produces high resolution images of the earth's surface. The radar generates a high peak frequency modulated power signal which is radiated through an array antenna towards the surface of the earth. Part of the returned echo is collected by the antenna and detected by the receiver, and recorded onto an optical film in the form of a hologram. This 'signal' film is then processed by an optical correlator where the synthetic aperture image is formed. The image is a two dimensional representation of the surface scattering, which is a function of the surface physical properties of an object; that is slope, roughness and dielectric constant (Sabins, 1978).

4.3.1 Characteristics of Radar Images

Visible and near infra red sensors such as LANDSAT MSS and TM provide information about the surface composition of surficial material. Thermal infra red sensors provide information about the thermal properties of the near surface layer. Radar sensors provide information about surface and sub-surface physical properties because, radar scattering is strongly controlled by the small scale roughness, surface vegetation, and man made structures. The tone of radar images is related to the average backscattering cross-section σ; and is given by

$$\sigma = \phi\ (\lambda, \theta, P, \phi, \tau_1, \tau_2, V) \qquad \textit{equation 4.4}$$

where λ is the wavelength, θ is the incidence angle, P is the polarisation of the incident wave, ϕ is the complex dielectric constant (dominated in most cases by the water content and density); τ_1 is the surface roughness; τ_2 is the sub-surface roughness and V is the complex volume scattering coefficient in heterogeneous media. Because of all these variables, the value of the backscattering cross- section is not available for most geological materials. In particular the values of V and τ_2 are the most difficult to quantify.

Approximate observations can be made about the likely radar response of a material. For example, a surface is said to be radar 'smooth' if it reflects the incident wave specularly in a single direction away from the receiver. A radar 'rough' surface is one which scatters the energy of an incident wave equally in all directions (diffuse scatterer). A surface may be rough for dome wavelengths and smooth for other wavelengths. According to the Rayleigh criteria this cross over point from a smooth to rough reflector is given by

$$h = \frac{\lambda}{8\sin\theta} \qquad \textit{equation 4.5}$$

where h is the scale of irregularities on the surface of the reflector λ is the wavelength (in the case of SIR-A 23 cm) and θ is the incidence angle of the radar (in the case of SIR-A 43 degrees). If we substitute these values into the equation the value of h is approximately eight cm, which is in good agreement with the observed occurrences of the SIR-A sensor (Elachi et al., 1982). Peake and Oliver (1971) modified the Rayleigh criterion to define surfaces that were clearly smooth (dark) from those which are rough (bright).

for a smooth surface $S \leq \frac{h}{25\cos\theta}$ *equation 4.6*

while for a rough surface $R \geq \frac{h}{4.4\cos\theta}$ *equation 4.7*

where S and R are the mean height of the irregularities of the surface.

4.3.2 Applications of Satellite Radar Data

The SIR-A experiment was specifically designed for geological applications and data were gathered over a number of geologically interesting sites in North Africa, North and South America and Central Asia: some of the results were described by Elachi et al. (1982). The radar has the advantage over passive sensors in that it can in certain favourable circumstances penetrate surficial material (especially if the surface is very dry). For example a SIR-A image of the Eastern Sahara Desert in the Sudan showed a huge previously unknown drainage system, some 250 km to the east of the Nile and flowing to the south rather than the north, this drainage system is covered in by up to five metres of sand McCauley et al. (1982).

Since radar images are so different from those of data sources in other parts of the electromagnetic spectrum, it seems appropriate to use them as an uncorrelated dimension in classification. This is not always the case, the radar is very sensitive to topography, therefore landforms may play a greater role in classification than surface properties. Because this is the case the practice of using coregistered radar data sets to modulate the brightness of images has been adopted by many researchers. Blom and Daily (1982) use LANDSAT MSS data modulated by SEASAT SAR data; this has the effect of sharpening the LANDSAT data. Topographic features are enhanced by the radar data, and variations in backscatter due to surface properties control the brightness of the colours. This gives the image substantially more lithological information than either the MSS on its own or the radar on its own.

4.3.3 Geometric Rectification of Radar Data

The radar imagery used in this study was flown on the second space shuttle flight in November 1981. The radar had a 23 cm wavelength (L- band), HH polarisation and an inclination of 38- 40 degrees with a spatial resolution of 40 m. The data are supplied as a photographic roll 125 mm wide and up to 30 m long. The swath width is 50 km which corresponds to the 40 m pixel being represented by 100 μm on the image. The image was scan digitised by Joyce Loebl using a drum scanning laser digitiser with a 100 μm aperture. Image registration to the MSS base image was by means of least squares fit model to common control points. A first order model was used of the type given in equations 4.1 and 4.2 in which eight control points were found for each test site, an RMS error of 1.2 pixels was found for test site 1 (or about 75 m), and 1.5 pixels (or 90 m) for test site 2. This type of model seems justified because of the small coefficients of xy (of the order of 10^{-4} or smaller). The control points for each geometric correction is given in tables 4.3 and 4.5, the coefficients of X and Y are given in tables 4.4 and 4.6. The RMS error was felt to be satisfactory because of the lack of prominent image control points. A nearest neighbour interpolant was used because of the rapid spatial variation of grey tone in radar images (its speckle): other interpolants such as bilinear were found to produce a very blurred output image because of this speckle.

Table 4.3 To give the control points for the least squares model for geometric rectification of SIR-A to LANDSAT MSS data and the associated errors, for test site 1.

POINT	REAL X	REAL Y	PRED X	PRED Y	ERROR
1	515.0	584.0	514.9	583.4	0.6
2	471.0	573.0	470.0	572.9	1.0
3	518.0	579.0	514.9	578.4	0.6

4	406.0	660.0	405.6	659.4	0.8
5	1169.0	1079.0	1168.4	1078.4	0.8
6	1264.0	1001.0	1264.5	1001.4	0.6
7	525.0	670.0	527.0	671.8	2.7

RMS ERROR FOR WHOLE SET IS 1.2 PIXELS

Table 4.4 To give the equation coefficients for the least squares model for geometric rectification of SIR-A data to LANDSAT MSS data, for test site 1.

EQUATION COEFFICIENTS	
X	Y
2356.5	637.9
-1.9	-6.2E-02
-1.3	0.6
1.5E-03	-3.5E-04

Table 4.5 To give the control points for the least squares model for geometric rectification of SIR-A to LANDSAT MSS data and the associated errors, for test site 2.

POINT	REAL X	REAL Y	PRED X	PRED Y	ERROR
1	231.0	816.0	233.3	815.2	2.4
2	221.0	815.0	221.7	815.6	0.9
3	876.0	907.0	875.2	906.6	0.8
4	873.0	675.0	873.4	675.3	0.5
5	173.0	327.0	172.1	326.2	1.2
6	144.0	388.0	144.9	389.5	1.8
7	89.0	612.0	87.9	610.7	1.7
8	151.0	907.0	149.5	907.8	1.7

RMS ERROR FOR WHOLE SET IS 1.5 PIXELS

Table 4.6 To give the equation coefficients for the least squares model for geometric rectification of SIR-A data to LANDSAT MSS data, for test site 2.

EQUATION COEFFICIENTS	
X	Y
-575.9	-409.3
1.0	0.6
-0.5	1.3
-7.7E-05	-1.8E-04

4.4 Preliminary Analysis of Data

A preliminary analysis of the data was undertaken by means of principal components analysis for each of the two test sites and for the three different data sources. The results are given in the following section.

Table 4.7 Principal components analysis of the 4 bands of LANDSAT MSS data for test site 1

Variance- covariance matrix

32.2	47.9	49.6	19.2
47.9	76.3	79.8	31.7
49.6	79.8	95.7	39.9
19.2	31.7	39.9	18.6

Eigen Values	Percent of Variance	Eigen Vectors				
210.7448	94.61	0.37	-0.49	0.67	0.42	Band 4
9.4641	4.24	0.59	-0.50	-0.62	-0.12	Band 5
1.3929	0.62	0.66	0.53	0.29	-0.44	Band 6
1.1404	0.51	0.27	0.48	-0.29	0.78	Band 7
		PC1	PC2	PC3	PC4	

Table 4.8 Principal components analysis of 4 band LANDSAT MSS data and SIR-A data for test site 1

Variance- covariance matrix

32.2	47.9	49.6	19.2	-6.9
47.9	76.3	79.8	31.7	-10.3
49.6	79.8	95.7	39.9	-8.8
19.2	31.7	39.9	18.6	-2.6
-6.9	-10.3	-8.8	-2.6	191.4

Eigen Values	Percent of variance	Eigen Vectors					
219.05	52.90	0.33	0.17	-0.49	0.67	0.42	Band 4
183.10	44.22	0.52	0.28	-0.50	-0.62	-0.12	Band 5
9.42	2.28	0.58	0.33	0.53	0.29	-0.44	Band 6
1.39	0.33	0.23	0.14	0.48	-0.29	0.78	Band 7
1.14	0.27	-0.48	0.88	-0.01	0.00	0.00	SIR-A
		PC 1	PC 2	PC 3	PC 4	PC 5	

Table 4.9 Principal components analysis of test site 2 four MSS bands

Covariance matrix

30.6	47.1	53.0	19.3
47.1	115.3	115.5	51.5
53.0	115.5	157.0	52.7
19.3	51.5	52.7	24.7

Eigen Values	Percent of variance	Eigen Vectors
295.48	90.19	0.27 0.11 0.94 0.19 Band 4
20.58	6.28	0.60 0.65 -0.16 -0.43 Band 5
10.45	3.19	0.70 -0.70 -0.11 -0.04 Band 6
1.09	0.33	0.27 0.27 -0.29 0.88 Band 7
		PC1 PC2 PC3 PC4

4.10 Principal components analysis of test site 2, four bands of MSS and coregistered SIR-A

Covariance matrix

30.6	47.1	53.0	19.3	4.4
47.1	115.3	115.5	51.5	16.8
53.0	115.5	157.0	52.7	18.9
19.3	51.5	52.7	24.7	7.8
4.4	16.8	18.9	7.8	171.4

Eigen Values	Percent of Variance	Eigen Vectors
300.98	60.31	0.26 -0.07 0.11 0.94 0.19 Band 4
165.98	33.26	0.59 -0.12 0.65 -0.16 -0.43 Band 5
20.58	4.12	0.69 -0.14 -0.70 -0.11 -0.04 Band 6
10.40	2.08	0.27 -0.05 0.27 -0.29 0.88 Band 7
1.10	0.22	0.20 0.98 0.00 0.02 0.00 SIR-A
		PC1 PC2 PC3 PC4 PC5

Table 4.11Principal components analysis of the six reflective TM bands for test site 2

Covariance matrix

457.7	235.7	379.8	331.3	550.3	380.5
235.7	130.6	219.1	193.3	315.7	225.6
379.8	219.1	400.2	357.6	572.3	427.0
331.3	193.3	357.6	325.9	520.8	387.2
550.3	315.7	572.3	520.8	1241.9	649.4
380.5	225.6	427.0	387.2	649.4	497.8

Eigen Values	Percent of variance	Eigen Vectors
2674.77	87.58	0.36 0.43 -0.72 0.28 0.23 -0.17 Band 1
254.99	8.35	0.21 0.21 -0.17 -0.11 -0.54 0.76 Band 2
103.07	3.37	0.37 0.31 0.18 -0.45 -0.48 -0.55 Band 3
15.97	0.52	0.33 0.24 0.26 -0.51 0.65 0.29 Band 4
3.26	0.11	0.64 -0.75 -0.14 -0.03 -0.01-0.01 Band 5
2.04	0.07	0.41 0.21 0.58 0.67 -0.01 0.04 Band 7
		PC1 PC2 PC3 PC4 PC5 PC6

Table 4.12 Principal components analysis Six reflective bands TM and coregistered SIR-A data

Covariance matrix

457.7	235.7	379.8	331.3	550.3	380.5	-56.2
235.7	130.6	219.1	193.3	315.7	225.6	-39.0
379.8	219.1	400.2	357.6	572.3	427.0	-73.3
331.3	193.3	357.6	325.9	520.8	387.2	-66.0
550.3	315.7	572.3	520.8	1241.9	649.4	-127.9
380.5	225.6	427.0	387.2	649.4	497.8	-79.2
-56.2	-39.0	-73.3	-66.0	-127.9	-79.2	174.6

Eigen Values	Percent of variance	Eigen Vectors						
2689.42	83.30	0.36	0.44	0.13	-0.70	0.28	0.23	-0.18 Band 1
255.75	7.92	0.21	0.21	0.01	-0.17	-0.10	-0.53	0.77 Band 2
161.33	5.00	0.37	0.31	-0.05	0.17	-0.45	-0.49	-0.54 Band 3
101.16	3.13	0.33	0.24	-0.05	0.25	-0.51	0.65	0.28 Band 4
15.78	0.49	0.64	-0.75	0.14	-0.13	-0.03	-0.01	-0.01 Band 5
3.21	0.10	0.41	0.21	-0.07	0.58	0.67	-0.01	0.04 Band 7
2.02	0.06	-0.08	0.09	0.98	0.18	-0.04	-0.02	0.01SIR
		PC1	PC2	PC3	PC4	PC5	PC6	PC7

In both test sites with the MSS data, more than 90% of the scene variance is accounted for by the first principal component (PC). In each case this first PC is made up of a positive contribution from all four bands, also in both cases the last PC accounts for less than 0.5% of the scene variance, this is in accordance with the findings of Chen and Collins (1982). Inspection of the imagery shows that the fourth PC is dominated by random noise. The principal component of the coregistered MSS and SIR-A images shows that addition of the SIR-A band significantly alters the amount of scene variance in the first PC. The first PC accounts for only 50 to 60% of the variance, while the second PC accounts for 30 to 40% of the variance. The first PC is made up largely of the reflected data, while the second PC is dominated by the SIR-A channel. Again the final PC consists of random (and therefore uncorrelated) noise. The six band TM first PC accounts for slightly less than 88% of the scene variance and is made up of positive contributions from all bands. The last three components account for less than one percent of the total scene variance and are dominated by noise. The addition of SIR-A data has a less marked effect than on the MSS data: the first PC accounts for over 83% of variance and again the last three components are dominated by noise.

It can be seen from the eigen vectors that LANDSAT MSS has highly correlated bands, this is to be expected because, we have seen in chapter 2 that the bands on LANDSAT MSS are poorly positioned for distinguishing geological materials. In test site 1 only the first two components are significant, the last two being dominated by noise. The first two components are strongly influenced by contributions from bands 5 and 6. In test site 2, the first three components are significant, the fourth again being dominated by noise. Again the first two components are dominated by a contribution from bands 5 and 6. The reason for this dominance may be because of the presence of Fe^{2+} (ferrous) minerals (such as, limonite, goethite and haematite) in the surficial layers. These minerals have a strong reflectance in bands 5 and 6, and relatively low reflectance in bands 4 and 7 of LANDSAT MSS (Drury, 1986a). This theory is further supported by the first component of the TM data which has a strong contribution from band 5, where the ferrous ion is also strongly reflective. The TM image has bands with a lower correlation then the bands of the MSS. This is to be expected, as it has been shown that the selection of bands for the TM was taken so that geological materials could be distinguished (Henderson and Swann, 1983)

The addition of SIR-A data makes a significant difference to the distribution to the variance of the data set, forming a new uncorrelated component. The striking difference of the SIR-A to the MSS is not surprising when it is considered that the MSS reflects differences in the surface composition of a material, while the SIR-A is reflecting differences in topography, surface roughness and water content (see section 4.3.1). Therefore, the addition of the SIR-A band, adds a significant amount of information to the understanding of these scenes.

4.5 Summary

Three different types of satellite data have been described, the pre-processing required to produce the data in the same co-ordinate system have been described and discussed. Rectification of TM data to MSS data was possible using fewer than ten control points, and produced RMS errors of less than a pixel. Rectification of scan digitised SIR-A data produced RMS errors of less than two pixels, using fewer than ten control points. A preliminary analysis of the data by means of a principal components analysis showed that the MSS bands had high correlation. The TM data also had highly correlated bands, but much less so than the MSS. Finally, the SIR-A data formed a band that was uncorrelated with both the MSS and the TM.

Chapter 5
Image Classification

5.0 Introduction

Image classification is a method whereby pixels are assigned to classes (in this case lithological classes) by the computer according to the vector which describes each pixel in the image. There are two distinct types of image classification, these are 1) unsupervised classification and 2) supervised classification.

5.1 Unsupervised Classification

Unsupervised classification techniques are based on automatic clustering techniques. A pixel represents a vector of measurements (in feature space) of a particular area on the ground, these measurements can indicate its reflectance in a particular waveband, its topographic height or any other spatially related attribute. Pixels which belong to a class will fall into clusters in feature space (if the chosen feature vector discriminates between the classes). If each of the clusters in the feature space are associated with a lithology then it should be possible to partition (classify) the imagery to produce a lithological map.

The difficulty is defining what is meant by cluster in terms explicit enough for the computer. A method of selecting a nucleus and building up around it could be used. The problem is the n (the number of pixels) can make this computationally expensive. For example, among 1000 pixels there are nearly half a million distances between pairs.

Kendall (1980) outlines a possible clustering technique which involves the following steps:-

1. Decide on some number of clusters (q), say 20, as an upper limit to the number of clusters in which we are interested.

2. Determine in p-dimensional feature space q cluster centres in some arbitrary way, say by spacing them at set intervals.

3. Consider the pixel values one at a time and allocate them to the nearest centre- thus 20 clusters are defined.

4. The centre of gravity of each cluster is defined.

5. The pixels are considered one at a time. A pixel is moved to another cluster if such a move reduces the overall sum of deviances of the two clusters. If a pixel is moved in this way, the new centre of gravity's are computed and replace the former ones.

6. The set of pixels is rescanned until no observation is moved to a new cluster. At this point having arrived at q clusters in such a way that the sum of deviances from the centres of gravity cannot be reduced by a pixel moving from one cluster to another.

7. A set of clusters is chosen for merging. Their combination should be such that it minimizes the increment in the deviances from their new cluster mean. All pairs of clusters are considered, the one chosen has the smallest increment in deviance. The calculation then proceeds to q-2, q-3 clusters in turn. At each stage the new cluster centres are computed, the distance between cluster centres, the sums of deviances of pixels from their respective cluster centres is calculated.

Thus a solution identifying q, q-1, q-2 etc clusters is defined. Duda and Hart (1973) design a clustering algorithm based on this procedure and according to Ramapriyan et al. (1985) it has been widely used in remote sensing. The choice of which solution best describes the themes in the image has then to be made, and this can be a subjective business. The unsupervised approach is often used in unexplored regions where little or no ground data are present. It may also be used prior to a supervised classification to show the likely position of classes in the feature space and to show whether spectral classes coincide with ground cover classes.

5.2 Supervised Classification

In supervised classification the interpreter defines training areas for the classifier. Each training area should be indicative of one of the themes in the image. The classifier calculates statistics from the training areas to find the spectral properties of each of the classes in the image.

There are three commonly used multispectral classifiers these are: (1) the parallelepiped, (2) the minimum distance to means, and (3) the maximum likelihood. Recently two other different types of classifier have been proposed, these have the merits of being

computationally simple, and are the decision tree classifier and the spectral shape classifier.

5.2.1 Parallelepiped Classifier

This is computationally the simplest and fastest of the commonly used multispectral classifiers and according to Curran (1985) is the most popular. The class minimum and maximum are calculated in each of the p bands of data. A pixel is assigned to a class if it falls within these boundaries in every band (see figure 5.1).

Figure 5.1 The decision boundaries for the parallelepiped classifier

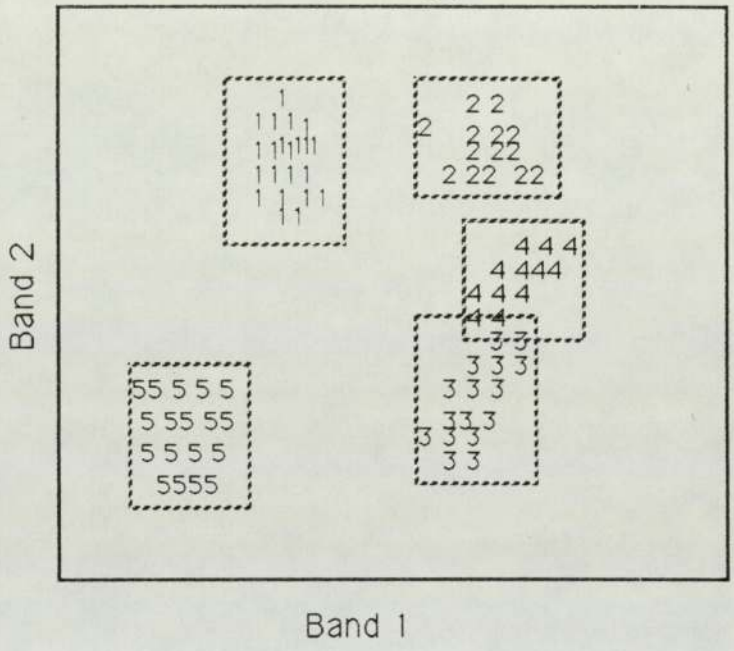

If the lowest value of a pixel in the training area of class C in band k is given by Lowck and the highest is given by Highck, then a pixel (i, j) of brightness Bvijk is placed in this class, if, and only if

Lowck < Bvijk < Highck. *equation 5.1*

This form of classifier gives rise to a box shaped decision surface (hence the name parallelepiped) with the decision surface parallel to the axes. Thus it is possible that a rotation of axes, such as a principal components transform or canonical analysis prior to classification, might improve the accuracy of the classifier.

Problems may arise when boxes overlap, these overlaps occur when spectrally similar classes have been chosen or when there is a high degree of correlation between the bands. Commonly if overlaps occur a pixel is placed in the first class that was defined,

though a more satisfactory method might be to reclassify such pixels according to a minimum distance rule.

5.2.2 Minimum Distance to Means Classifier

This is a computationally relatively simple and widely used classification algorithm (Jensen, 1986). Here the mean value of each q classes is calculated for p bands, this gives q different points in p- dimensional feature space (the mean vector). A pixel is assigned to the class mean to which it is closest. The distance can be the euclidean distance or a round the block distance (Swain and Davis, 1978) (see figure 5.2) .

Figure 5.2 The decision boundaries for the minimum distance to means classifer.

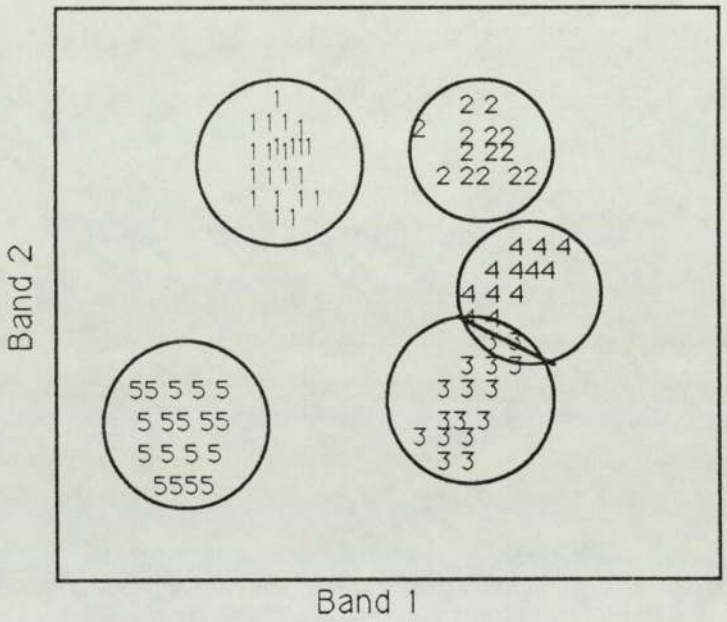

Computation of Euclidean distance from a pixel (i, j) of brightness Bvijk in band k and brightness Bvijl in band l from a mean vector Uckl for class C is given by,

$$\text{Dist} = \sqrt{[(Bvijk-\mu ck)^2+(Bvijl-\mu cl)^2]}. \qquad \textit{equation 5.2}$$

A threshold limit which prevents pixels which fall a great distance from the mean can be used. This gives the decision boundary a circular shape in two dimensions and a spherical shape in three dimensions (see figure 5.2).

5.2.3 Maximum Likelihood Classifier

This is the most computationally expensive classifier and usually the most accurate (Tomlins, 1981). The mean for each class is calculated and so is the variance-

covariance matrix, on the assumption that the data for each class are normally distributed. With this information the spread of pixels around the vector can be described using a probability function. To classify a pixel X into a class C, the maximum likelihood decision rule computes the value P_c the probability of X belonging to class C, this is given by,

$P_c > P_i$ where i=1,2,3.....,m possible classes

and

$$Pc = [-0.5\text{Log}_e(\det(V_c))]-[0.5(X-\mathbf{M}_c)^T(V_c^{-1})(X-\mathbf{M}_c)]. \qquad \textit{equation 5.3}$$

where det V_c is the determinant of the covariance matrix V_c and V_c^{-1} is the inverse of the covariance matrix, $\mathbf{M}_c$ is the mean vector of class C and T is the transpose. Pixels are allocated to the class to which they have the highest probability of belonging.

A threshold can be used to stop pixels with a low probability of belonging to a class from being classified. This gives the decision boundary ellipse shape in two dimensions (see figure 5.3).

Figure 5.3 The equiprobablity boundaries of the maximum likelihood classifier.

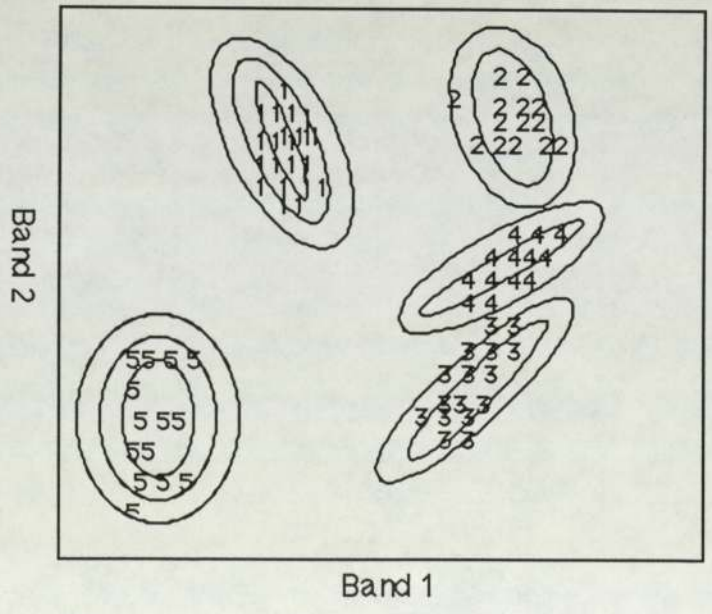

A slight alteration to the maximum likelihood decision rule can be made which takes into account the probability of a pixel of a certain class occurring in the scene. For

example if a large part of the scene covers the sea, then water can be given a higher probability of occurring than some other classes in the image. This is known as the Bayes decision rule, in which a pixel is placed into class C if and only if,

$$P_c(ac) > P_i(ac) \quad i=1,2,3.....m \text{ possible classes}$$

and

$$P_c(ac) = Log_e(ac)-[0.5Log_e(det(V_c))]-[0.5(X-\mathbf{M}_c)^T(V_c^{-1})(X-\mathbf{M}_c)]. \quad \textit{equation 5.4}$$

Thus the rule is identical to the maximum likelihood rule except that it does not assume that all classes are equally probable (Hord, 1982). Strahler (1980) uses prior probabilities to successfully incorporate the effects of relief and other terrain characteristics to improve classification accuracy.

5.2.4 Decision Tree Classifier

The decision tree classifier is a computationally simplest of the multispectral classifiers, the basic concepts were described by Swain and Hauska (1977), Baur et al. (1981) and Belward and DeHoyos (1987). In this classifier the means and standard deviations for each training area are plotted for each band, these are called coincident spectral plots (see figure 5.4). Decision rules for each class are calculated by simply setting upper and lower limits for each class in the most appropriate bands.

In Figure 5.6, class 4 can be identified by its low mean in band 4, and class 3 can be identified by its low means in bands 5 and 7. A set of decision rules can be generated which describe all the classes in the image. Unfortunately in most cases the geological materials used in this study do not have sufficiently good spectral differences to allow simple unambiguous decision rules to be generated. Therefore in an attempt to overcome this shortcoming rules were used which employed multiple Boolean 'AND's'. Rules of the type given in equation 5.5 were used.

'IF B1 < 10 AND B2 > 20 AND B3 < 15 THEN class= 1' *equation 5.5*

where B1, B2 and B3 are the brightness values of any pixel in bands 1, 2 and 3 respectively.

Figure 5.4 Coincident spectral plots for the five class means ± one standard deviation, LANDSAT MSS and SIR-A of test site 1

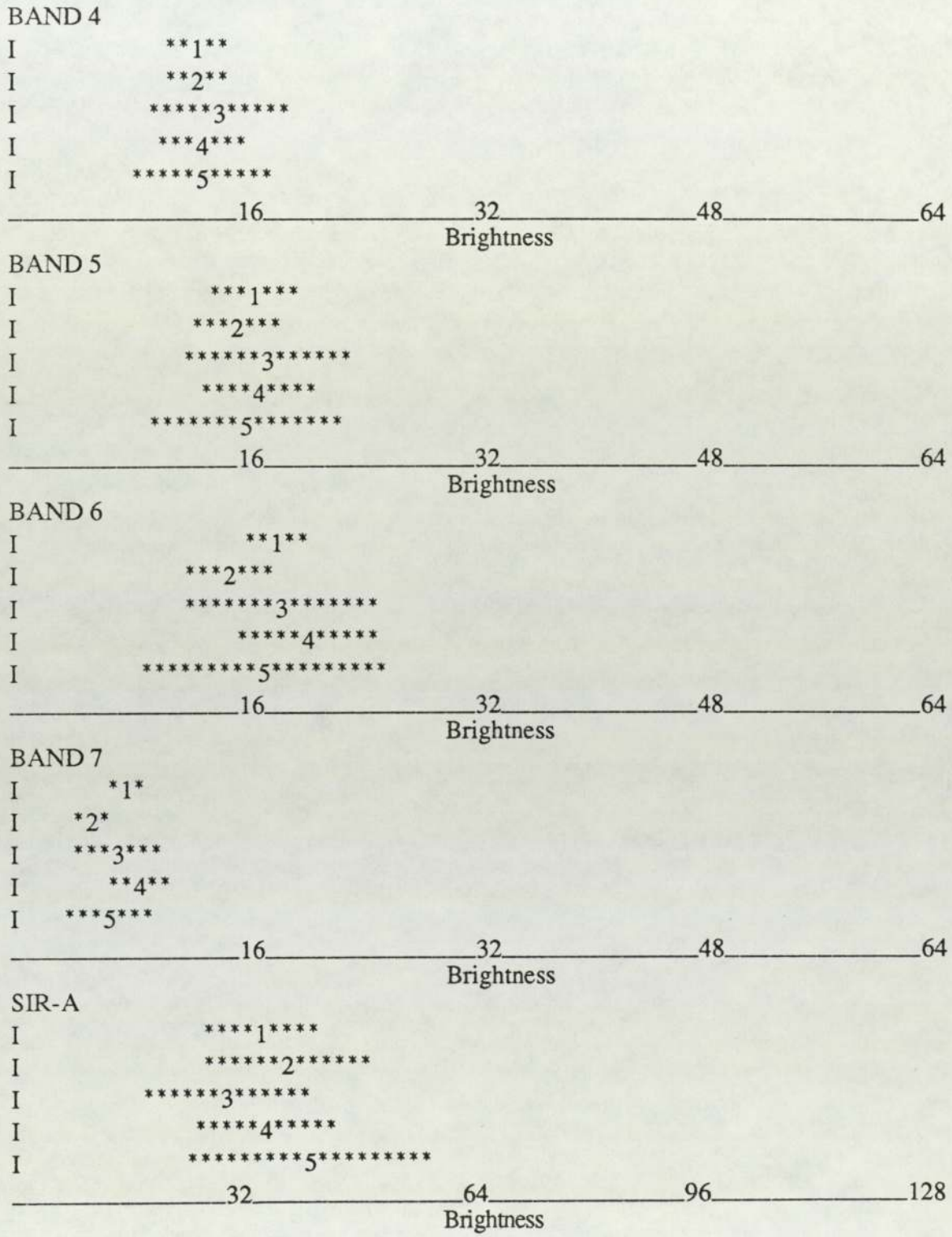

Figure 5.5 Coincident spectral plots of class means ± one standard deviation, LANDSAT MSS and SIR-A of test site 2

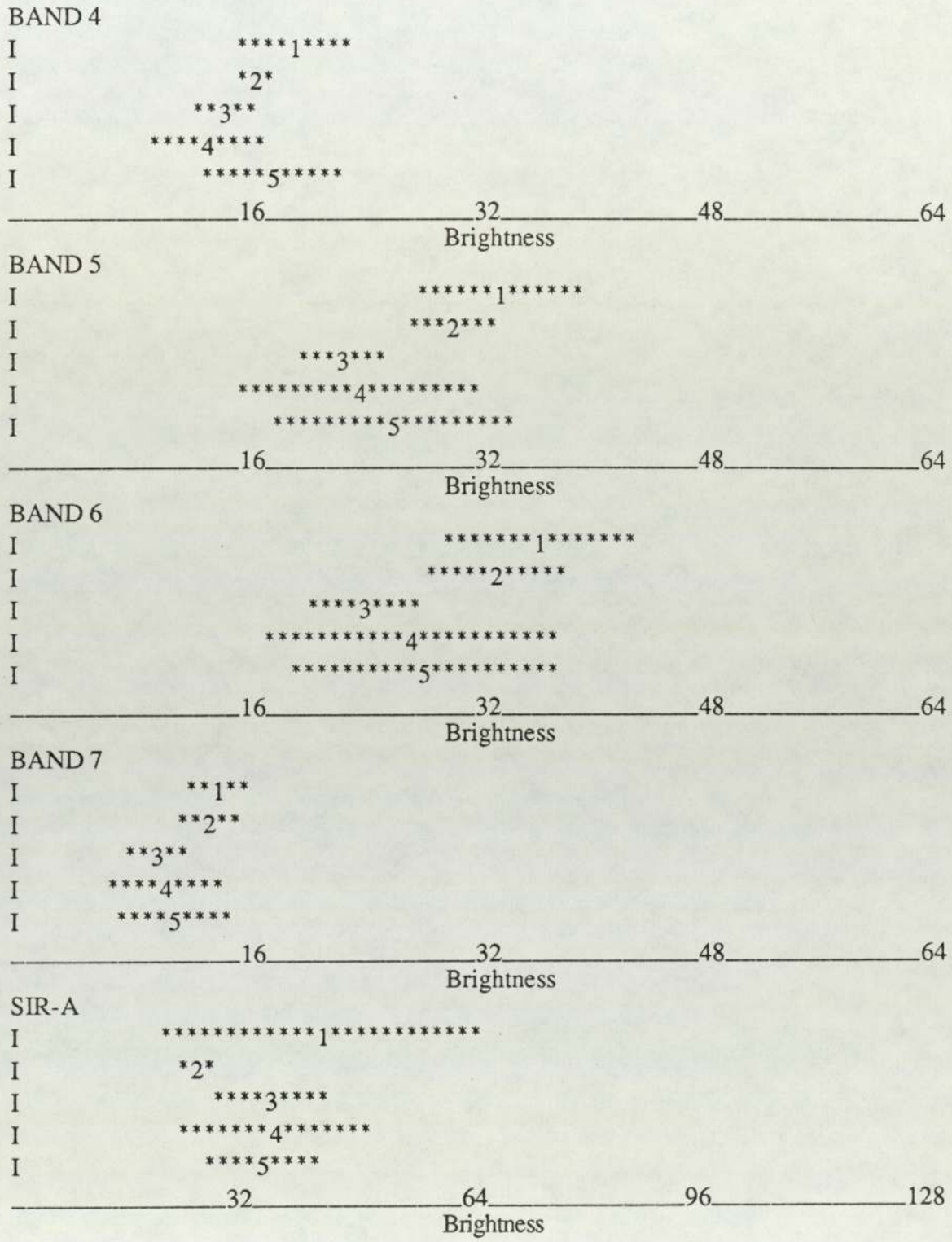

Figure 5.6 Coincident Spectral plots of class means ± one standard deviation, LANDSAT TM for test site 2

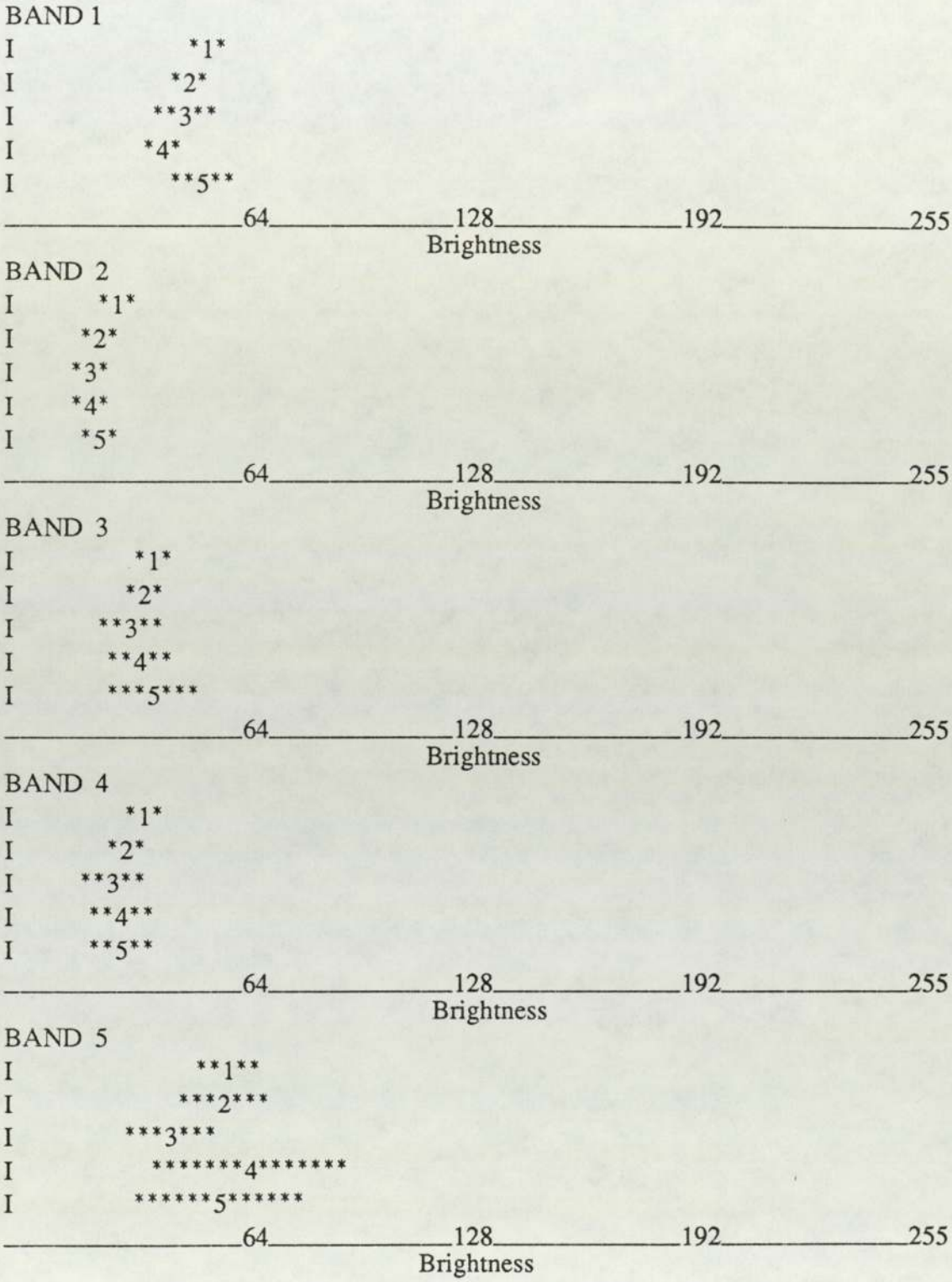

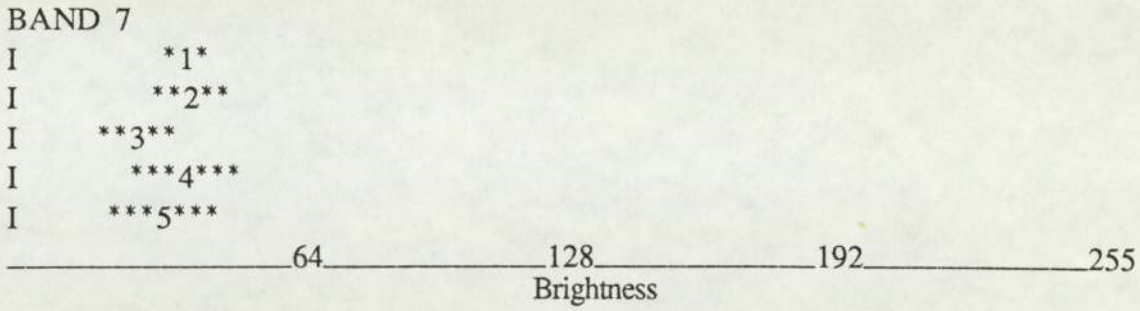

The decision rules used in this study are given in Figures 5.7 to 5.9. The decision rules can be generated either manually or automatically, and according to Lee and Richards (1985) "There may be value in allowing the operator to design the decision tree manually".

Figure 5.7 The decision tree classifier for test site 1 LANDSAT MSS and SIR-A

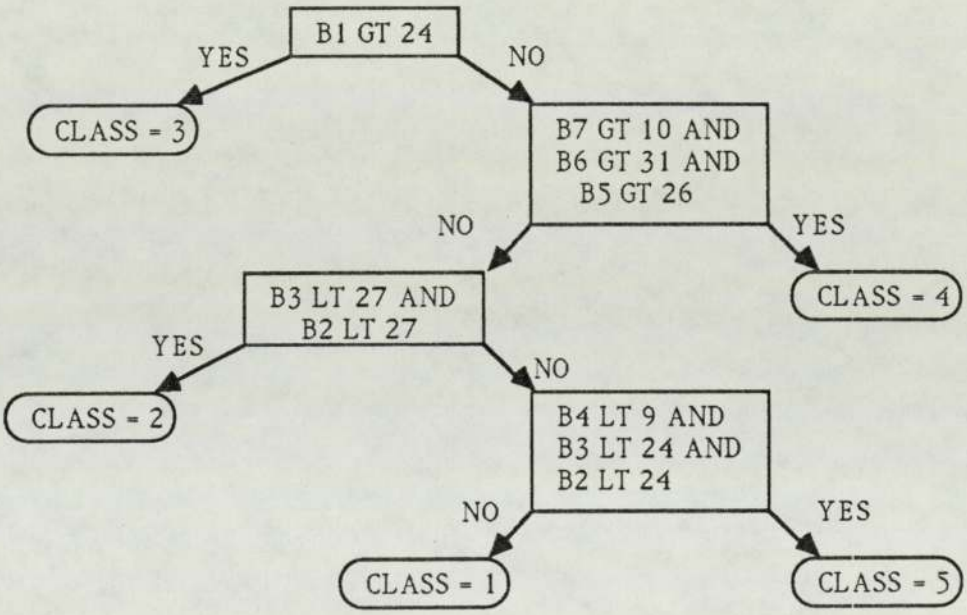

Figure 5.8 decision tree classifier for test site 2 LANDSAT MSS and SIR-A

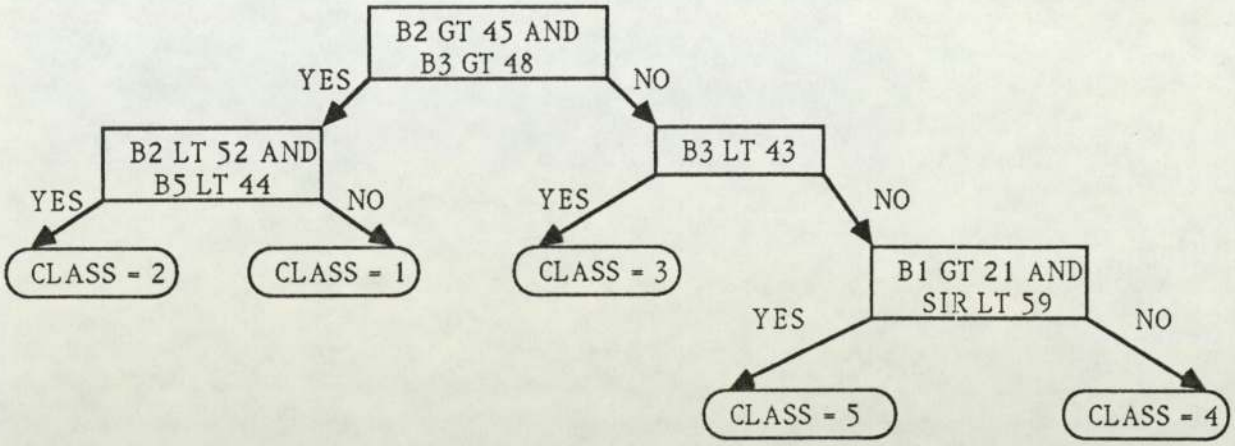

Figure 5.9 decision tree classifier for site 2 using TM data.

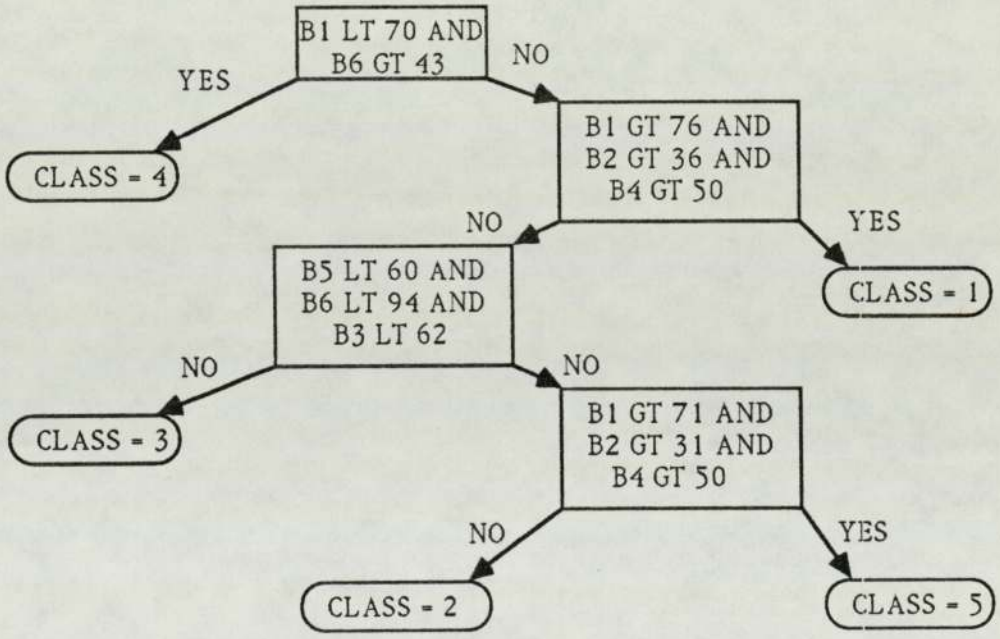

Belward and Hoyos (1987) test the decision tree classifier for crop cover estimation in southern England, they compare the classifier with a conventional maximum likelihood classifier (see section 5.2.3). They found that the maximum likelihood classifier had an average classification accuracy of 57.2% and took 150 minutes of computer while the decision tree classifier achieved an accuracy of 64.8% and took no computer time (it did take some 40 minutes to generate the decision rules). An automatic technique might use Quinlan's ID3 induction algorithm (Quinlan, 1983). ID3 takes objects of a known class (that is, training area data), and produces a decision tree that correctly classifies all given classes. There is a strong similarity between decision tree classification

techniques and the use of production rule based systems used in the field of artificial intelligence.

5.2.5 Spectral Shape Classifier

The spectral shape classifier is a computationally inexpensive algorithm which is useful for highly dimensioned data sets, such as are becoming increasingly common in remote sensing. The spectral shape classifier is described by Pendock (1987), but little work has been reported on its effectiveness.

The basis of this classifier is that each pixel in the image consists of n measurements (spectral or textural), and each measurement has one of the three characteristics with respect to the other measurements of the same pixel. It is either 1) a local minimum, 2) a local maximum or 3) neither a local maximum or minimum (it has an intermediate value): this is shown in figure 5.10. These characteristics thus describe the shape of the spectral curve for themes within the image. A classification is produced by representing these characteristics in an n digit number ternary word (a flow chart for the spectral shape classifier is given in appendix 1).

Figure 5.10 To illustrate the spectral shape classifier.

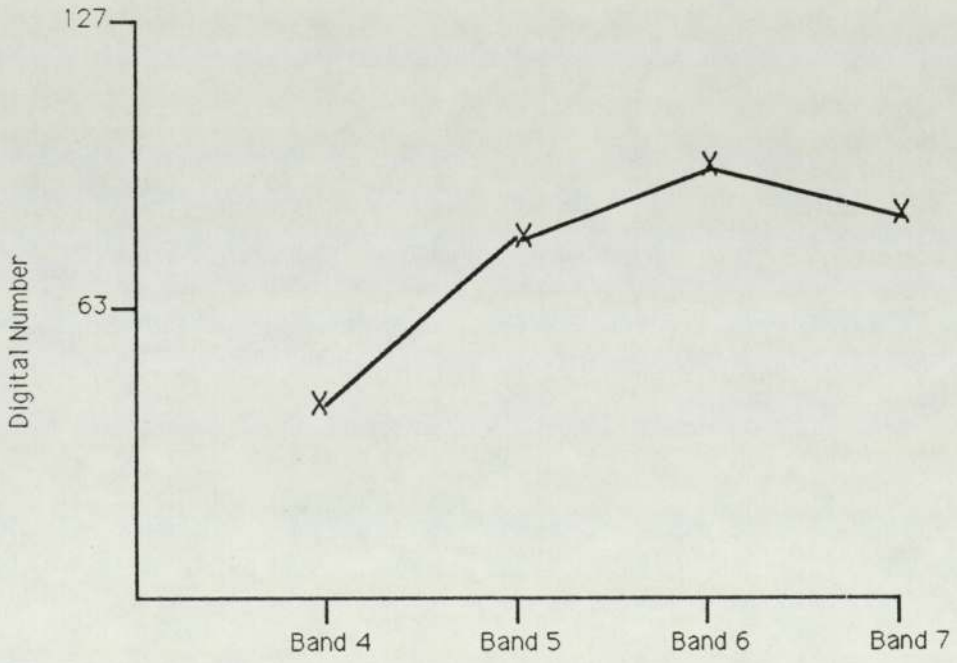

The classification criteria are:

1) If measurement j is a local maximum, digit number j = 0

2) If measurement j is a local minimum, digit number j = 2

3) If measurement j is a neither a minimum or a maximum, digit number j = 1

So the spectral shape classifier assigns the ternary number 2102 to our spectral shape in figure 5.10 which is 20 as a decimal number. Thus the classifier can simply and quickly reduce highly dimensioned data sets to a single number.

Pendock (1987) uses the classifier as an unsupervised algorithm. The classifier can, however, be adapted in the following way, to make it a supervised classifier (Oldfield et al., 1988). A histogram is constructed of the spectral shapes for each training area. The histogram is normalised by dividing the number of times a spectral shape occurs by the number of pixels in the training area. Each pixel in the whole image is then placed in the class which has the maximum frequency of occurrence for that pixels spectral shape. In this way a large majority of the pixels are classified. The remaining pixels can be placed into the nearest histogram occurrence to their peculiar shape. The flow chart for this type of classifier is given in Appendix 1.

An extension of the idea might be to subdivide the intermediate class into positive slopes and negative slopes. Thus the spectral shape is represented by an n digit number quaternary word. The advantage of this type of classifier is that it is computationally efficient, as the number of computations increases linearly with the number of bands.

5.3 Measurement of Classification Accuracy

It is necessary to have some idea of what accuracy remote sensing classification maps can obtain. For example, the overall classification accuracy of landuse maps should generally be 85%, and the accuracy of each of the classes should be similar (Anderson et al., 1976). This sort of figure might well also be applicable to lithological maps.

Perhaps the simplest way of measuring classification accuracy is to compare each of the training areas classified compared with its assumed true class. Unfortunately, the locations of the training sites are biased by the analyst. Because of this bias, the classification accuracy of pixels found in the training sites is generally higher than in the remainder of the map. This is hardly surprising since these were the actual data points that were used to train the classifier. This method of testing the accuracy seems to have little merit. An alternative is to define a number of test locations for each class which are not used to train the classifier. It is important that sufficient pixels are defined to test the accuracy of each class and also that the test areas are randomly distributed

throughout the image. In order to do this some analysts use random number generators to define test sites (Jensen, 1986).

Most studies employ an error matrix (also called a confusion matrix or a contingency table) to graphically show the distribution of error (see figure 5.11). The rows of the matrix are the true class, the columns are the class assigned by the classifier. The entries in the matrix represent the frequency of true class i being given a class j by the classifier. Thus the leading diagonal elements represent correctly classified data, and the off diagonal elements of the represent the misclassified data. An important property of the error matrix is its ability to show errors of commission (over classification of a class) and errors of omission (under classification). The errors of commission are horizontal and the errors of omission are vertical.

Figure 5.11 An Error Matrix

Ground data \ Classified As	1	2	3	4	5
1	78	1	12	4	5
2	3	82	10	2	3
3	4	3	62	20	13
4	12	10	1	73	2
5	3	4	15	1	77

A gross classification accuracy (this the most commonly quoted figure) can be obtained by dividing the sum of the leading diagonal elements in the matrix by the total number of elements in the matrix.

Thus in figure 5.11 there are 78 + 82 + 62 + 73 + 77 = 372 leading diagonal elements out of a total of 500 elements, there is a gross classification accuracy of:

(372/500)*100 % or 74.4%. *equation 5.6*

Congalton and Mead (1983) suggest a statistic which was originally developed by Cohen (1960). This can be derived from the error matrix, and is the kappa or khat statistic. This measures the proportionate reduction in error achieved by a classifier as compared with the error of a completely random classifier: it has the range of 0 to 1. Thus a value of 0.75 would indicate that the classifier was avoiding 75% of the errors that a totally random process would have produced. (Lillesand and Kiefer, 1987). This test was recommended as a standard for remote sensing data by Rosenfeld and Fitzpatrick-Lins (1986). The widespread use of the kappa statistic has been impeded by the incorrect formulation of the statistic, Hudson and Ramm (1987) and Congalton (1987), and its incorrect coding in the software supplied by Congalton. For these reasons the statistic was not used in this study.

5.4 Image Classification in Geology

Few studies (if any) have been undertaken on the accuracy of geological maps; but an accuracy in the region of say 85-90% would seem to be the minimum acceptable. Computer based classification using stratigraphic units in LANDSAT MSS scenes have achieved relatively low and generally unacceptable accuracies, typically in the 40-60% range in semi-arid terrains (Short, 1984).

Geological mapping has been undertaken for many decades using stereo aerial photography, and accuracy in the region of 80-90% is often achieved especially in arid and semi-arid regions (Short, 1982). In many ways a satellite image can be thought of as a small scale, low resolution aerial photograph. Hence they cannot pick out certain geological details, such as the dip of stratigraphic formations and subunits whose thickness are smaller than the spatial resolution of the sensor. A major question therefore arises, of what is the accuracy level which can be achieved with satellite imagery.

Siegal and Abrams (1976) in the Coconinno Plateau of Arizona used LANDSAT MSS data with supervised and unsupervised classification algorithms, but found consistently low accuracy (40-55%) regardless of the method. Siegal, in Siegal and Gillespie (1980) found higher accuracy using Thematic Mapper Simulation data because the spectral range of these data is better suited to lithological discrimination.

Limits to the accuracy of classification based solely on spectral properties are because of the nature of geological maps; firstly because geological maps depict stratigraphy. Remotely sensed images and derivative maps can recognise only relative ages, and then

only if suitable control units such as cross cutting relationships are present. Secondly bedrock is usually mapped by extrapolation of surficial outcrops based on structural data from the outcrop. Because of the low spatial resolution and the lack stereoscopy (except for SPOT and some SIR-B) structural relationships cannot be measured. Therefore satellite classification maps can indicate only the distribution of surficial material.

Because of the above limitations, there may be a fundamental upper limit to the accuracy obtainable with satellite data. This may be a fundamental nature of the ground target (that is, geology). However spectral classifiers do not use all the available information about a lithology. Later chapters will show how spatial (textural) and contextual information can now be used to mimic the human interpreter and therefore possibly increase classification accuracy.

5.5 Image Classification of Test Sites

To train and test the classifier in each of the two test sites, a series of training areas and test areas for each class were defined (two training areas and two test areas for each class). The means, variance-covariance and coincident spectral plots for each class were derived from the training area data. The test areas were used to generate error matrices to test the classification accuracy of each type of classifier. The normalised accuracy is generated by dividing the number of pixels classified as a certain class by the total number of pixels in that test area. In this way it is possible to compare small test areas (those with few pixels) directly with classes where it is possible to define large test areas (those with many pixels). The results of minimum distance, decision tree and maximum likelihood classifications are given in tables 5.1 to 5.3. The leading diagonal of the confusion matrix (that is the correctly classified pixels), are expressed as a fraction of 1.0. Also given in the final column is the overall classification accuracy as a percentage.

Table 5.1 normalised accuracy (fraction of 1.0) and average classification (%) for test site 1. LANDSAT MSS and SIR-A.

MINIMUM DISTANCE TO MEANS						
	Class 1	Class 2	Class 3	Class 4	Class 5	Average
4 bands MSS	0.41	0.67	0.15	0.77	0.08	41.83
4 bands MSS + SIR-A	0.38	0.36	0.62	0.50	0.58	42.76
DECISION TREE						
	Class 1	Class 2	Class 3	Class 4	Class 5	Average
4 bands MSS + SIR-A	0.86	0.33	0.09	0.59	0.36	44.71
MAXIMUM LIKELIHOOD						
	Class 1	Class 2	Class 3	Class 4	Class 5	Average
4 bands MSS	0.61	0.94	0.26	0.74	0.49	60.70
4 bands MSS + SIR-A	0.64	0.94	0.39	0.76	0.50	64.32

Table 5.2 normalised accuracy (fraction of 1.0) and average classification (%) for test site 2. LANDSAT MSS and SIR-A.

MINIMUM DISTANCE TO MEANS						
	Class 1	Class 2	Class 3	Class 4	Class 5	Average
4 bands MSS	0.45	0.66	0.40	0.18	0.37	41.01
4 bands MSS + SIR-A	0.57	0.46	0.70	0.23	0.37	46.76
DECISION TREE						
	Class 1	Class 2	Class 3	Class 4	Class 5	Average
4 bands MSS + SIR-A	0.50	0.31	0.86	0.24	0.44	46.84
MAXIMUM LIKELIHOOD						
	Class 1	Class 2	Class 3	Class 4	Class 5	Average
4 bands MSS	0.55	0.49	0.62	0.74	0.60	59.82
4 bands MSS + SIR-A	0.77	0.54	0.62	0.80	0.69	68.60

Table 5.3 normalised accuracy (fraction of 1.0) and average classification (%) for test site 2. LANDSAT TM and SIR-A.

MINIMUM DISTANCE TO MEANS						
	Class 1	Class 2	Class 3	Class 4	Class 5	Average
6 bands TM	0.73	0.34	0.68	0.44	0.22	48.15
6 bands TM + SIR-A	0.75	0.43	0.67	0.46	0.25	51.17
DECISION TREE						
	Class 1	Class 2	Class 3	Class 4	Class 5	Average
6 bands TM + SIR-A	0.38	0.55	0.51	0.44	0.57	49.08
MAXIMUM LIKELIHOOD						
	Class 1	Class 2	Class 3	Class 4	Class 5	Average
6 bands TM	0.86	0.59	0.41	0.89	0.81	71.14
6 bands TM + SIR-A	0.87	0.58	0.43	0.92	0.81	73.01

The best case results for image classification of test 1 using MSS with SIR-A data and of test site 2 using both MSS with SIR-A data and, TM with SIR-A data are given in maps 5.1, 5.2 and 5.3 respectively, in each case these are maximum likelihood classified images.

Map 5.1 Maximum likelihood classification of test site 1 using LANDSAT MSS and SIR-A data

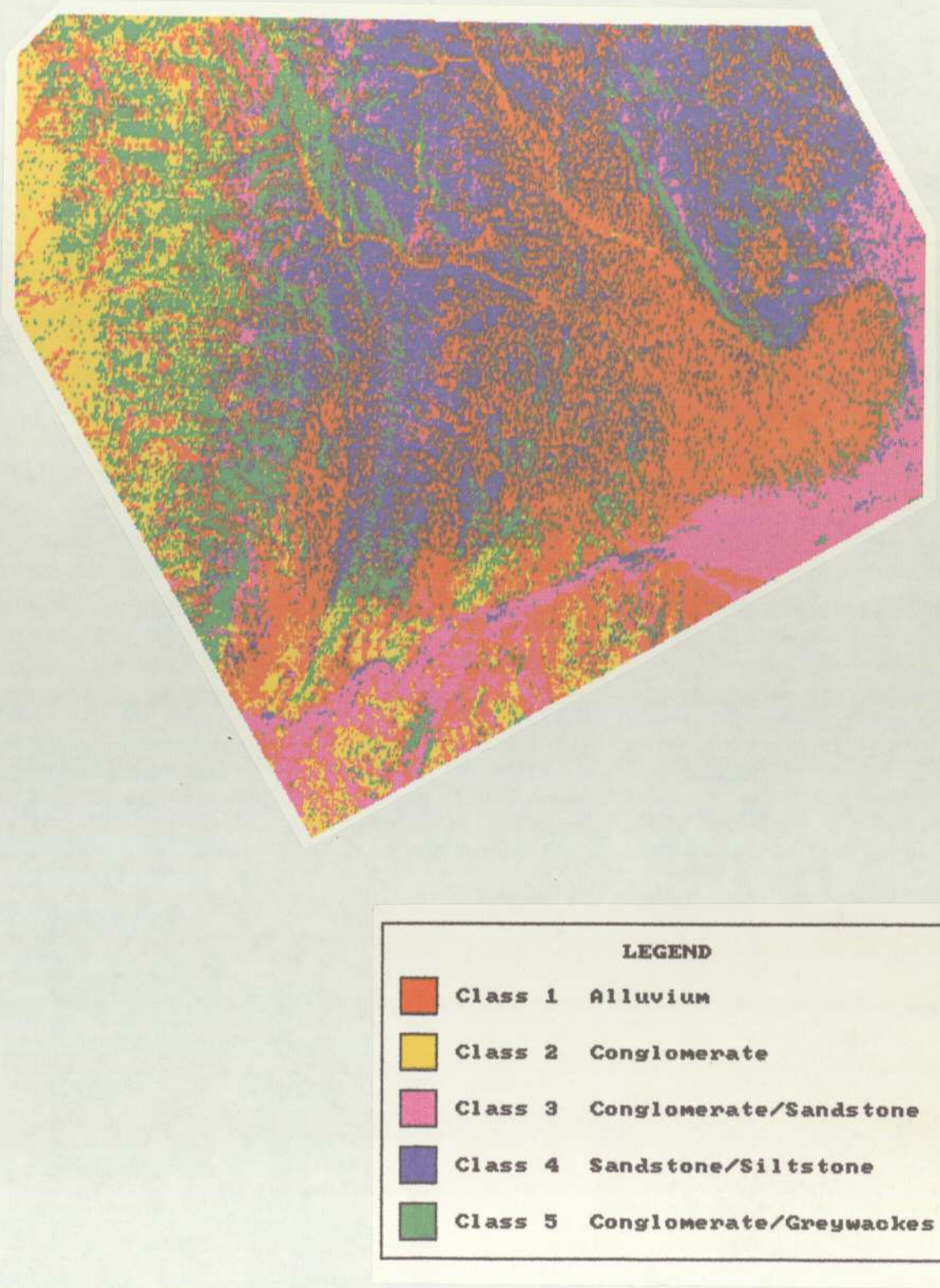

Map 5.2 Maximum likelihood classification of test site 2 using LANDSAT MSS and SIR-A data

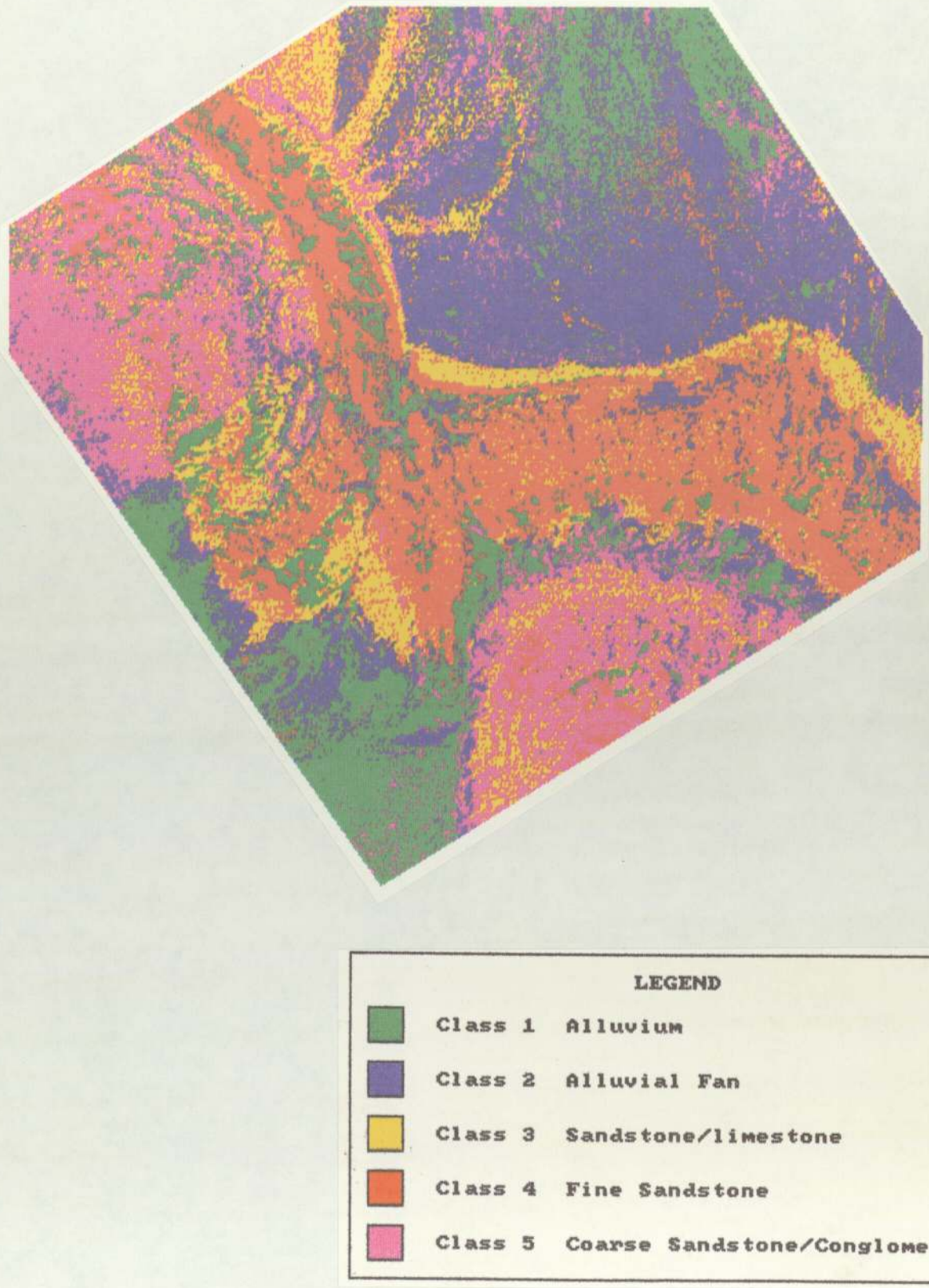

Map 5.3 Maximum likelihood classification of test site 2 using LANDSAT TM and SIR-A data

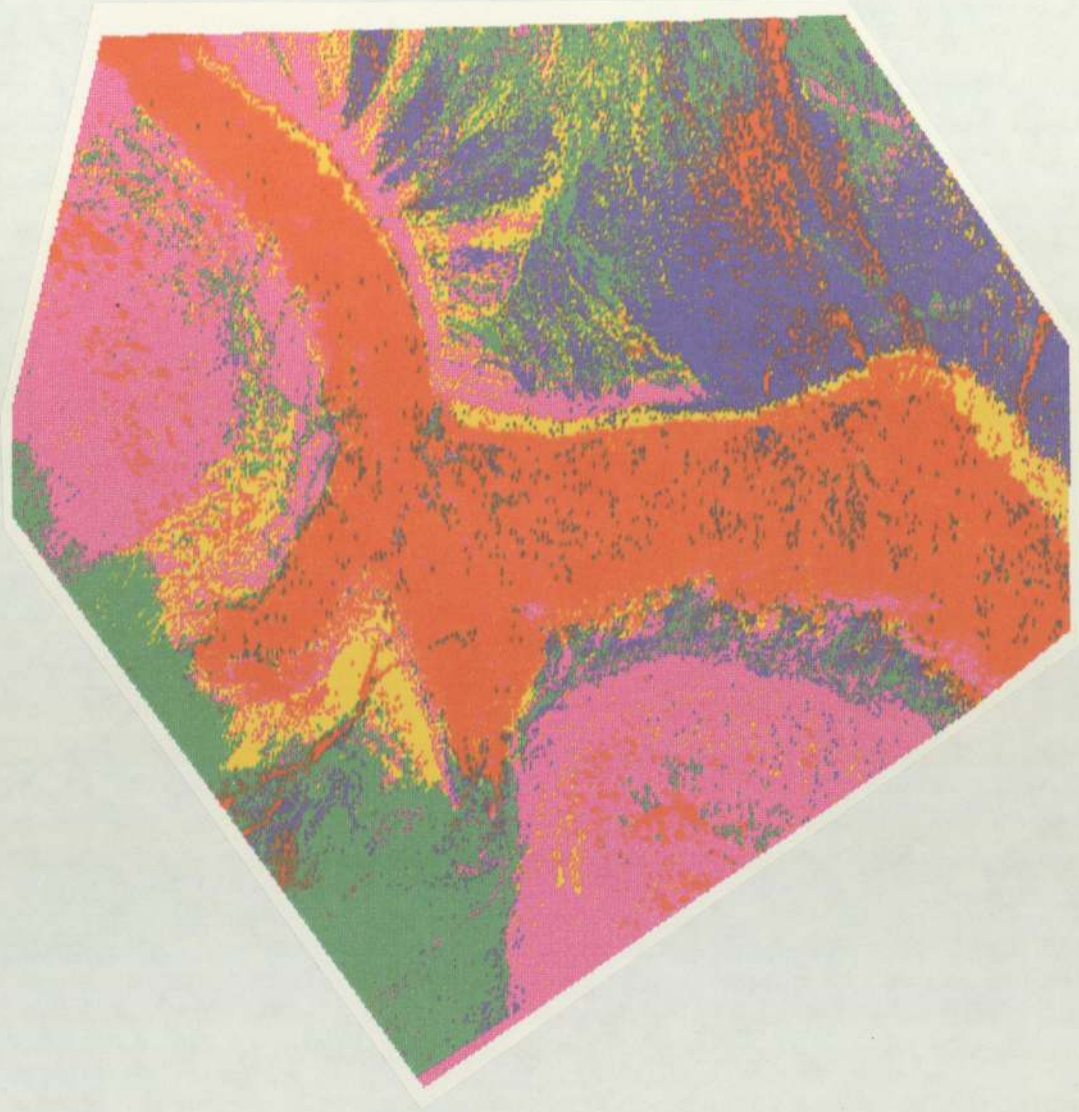

In test site 1 the minimum distance and the decision tree classifier show disappointing results for classes 3 and 5 (both classes are confused with classes 2 and 4). This is explained when regard is paid to the coincident spectral plots for these classes (figure 5.7), which shows these classes have very much higher standard deviations than the other three classes in the image. The slight improvement in the accuracy with the addition of the SIR-A band is due to the increase in accuracy of these two classes, but these gains are at the expense of lowering the accuracy of the other three classes.

The minimum distance and decision tree classifier for test site 2 perform poorly for class 4 (being confused with class 2), with the LANDSAT MSS and SIR-A data, but they perform relatively well with the TM data. Again the reason seems to be the high standard deviation of class 4 in both the MSS and the SIR-A data. The TM shows a much lower standard deviation for this class and consequently it has a much higher accuracy. Overall the TM performs significantly better then the MSS, with results up by between 5 and 10 % for each class.

The maximum likelihood results for test site 1 shows higher accuracies in all classes over the minimum distance and decision tree classifiers (by between 10 and 20 % for each class). However, class 3 again shows a disappointingly low result (being confused with classes 2 and 4). The addition of the SIR-A adds nearly 4 % to the overall accuracy, most of this gain being due to the increase for class 3.

The maximum likelihood results for the test site 2 using MSS shows higher accuracies for all classes over the minimum distance and the decision tree classifiers (again between 5 and 10 % for each class). The addition of the SIR-A band also increases accuracy by a significant amount (nearly 9 %), the increase being spread over all classes. The TM for this test site showed higher accuracies for each class over both the MSS and the combined SIR-A and MSS. The addition of the SIR-A to the TM increases accuracy by under 2 %

5.6 Timing of Classifiers

The timings of each of the classifiers relative to the fastest classifier are given in Figure 5.11. The fastest classifier is the decision tree classifier, and most of the time for this algorithm is taken up by input/output operations. The maximum likelihood classifier show a disproportionate increase in time taken for the increase in classification accuracy: the seven band maximum likelihood classifier being nearly 60 times slower than the decision tree classifier. Caution should be taken when using these figures, as

the decision tree classifier requires the interpreter to define the decision rules, a process which can be both time consuming and subjective.

Figure 5.12 Timings against classification accuracy of the various classifiers .

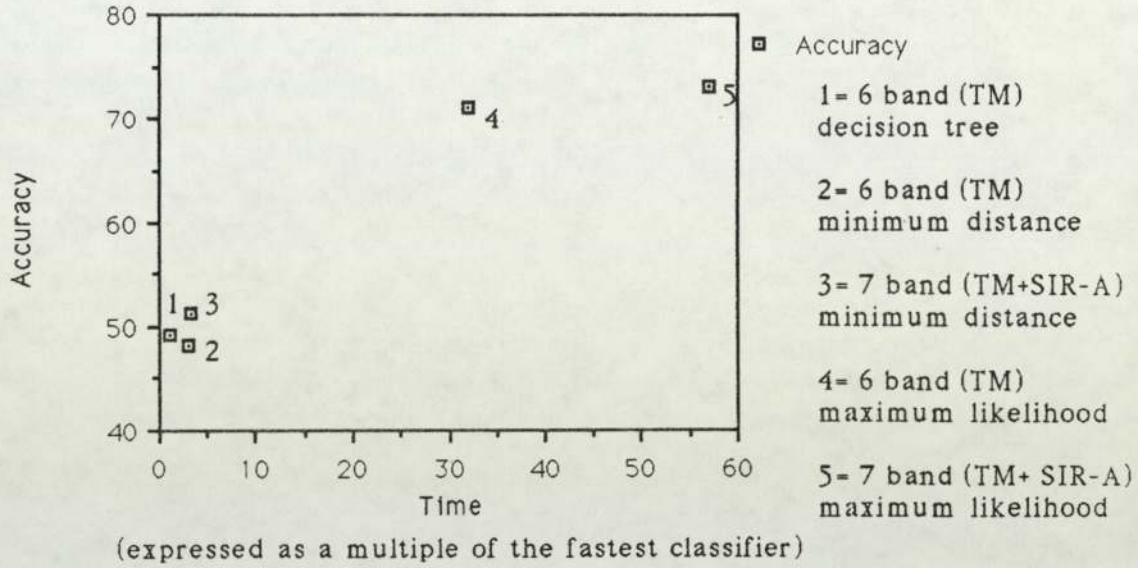

(expressed as a multiple of the fastest classifier)

5.7 Summary

Five different supervised classification algorithms have been described in detail. The results of these classifiers on the two study sites show that the addition of SIR-A to multispectral image data such as MSS or TM can significantly improve the classification accuracy. In terms of accuracy the minimum distance and decision tree classifier perform poorly when compared with the maximum likelihood classifier. The maximum likelihood classifier, however, is very much more expensive computationally than either the minimum distance or the decision tree classifier. This may be of less importance as new, faster processors (possibly with parallel architecture) become available.

Chapter 6
Texture

6.0 Introduction

The compositional data conveyed by the single pixel of a sensor does not carry enough information to uniquely identify the lithology at that point. For example, a sandstone and a granite may have similar mineralogical compositions: quartz, feldspar and a mafic (often a mica), and can therefore have similar spectral characteristics, but they are very different lithologies. The regular bedding and strong, regular jointing of a sandstone give rise to a different texture to the strongly, irregularly jointed granite, therefore the rock types can be distinguished. Furthermore, rocks that are lithologically similar have dramatically different weathering characteristics and therefore they have quite different surface spectral signatures. On the other hand rocks that are dissimilar may have similar photomorphic weathering characteristics (Shih, 1983). Therefore it is desirable to use more information than just the spectral data to discriminate rock types. Texture is an important characteristic of many types of imagery. This is particularly so in the case of geological remote sensing using LANDSAT MSS data which, as was shown in section 2.4.1 has poorly positioned spectral bands to discriminate lithologies. In this chapter discrimination and measurement of textural features will be described.

Texture can be seen in all types of images, from those derived from satellite down to microscopic images of rock thin sections. However, despite the importance of image texture no precise definition exists. A dictionary definition of texture might be "something composed of closely interwoven elements". This definition has some merits and gives some insight into the nature of texture. Blom and Daily (1982) define image texture as 'the spatial variation of image tone..', a similar definition is given by Haralick et al. (1973) who goes on to say that 'textural features contain information about the spatial distribution of tonal variations'. Therefore, even though no precise definition of texture exists, some insight into the nature of this property can be obtained by these rule of thumb descriptions. There is no need to precisely define the property in order to assign some measure to it. Intuitively some understanding of texture is given by simple adjectives used to describe it such as, coarseness, smoothness or roughness.

Two approaches to texture analysis have been followed, namely structural analysis and statistical analysis. The former depends on finding certain textural primitives (texels) and using these texels to cover (or tessellate) a region of an image (Ballard and Brown, 1982). Statistical techniques use a wide variety of statistical models in order to quantify

the amount and type of texture present in an image. Structural analysis has proved to be useful in regular or man-made textures such as tiling or cloth or brickwork, where relatively simple texels are present and they tessellate a plane in a relatively simple fashion. In natural textures such as images from satellites, statistical techniques are more widely used than structural techniques. This is because the structural primitives are not easily modelled and their tessellation is complex.

6.1 Textural Properties

Several separate properties of texture can be measured and according to Tamura et al. (1978) these include:-

1) Coarseness; this is perhaps the most fundamental property of texture and received much of the early investigation, for example Rosenfeld and Troy (1970) and Hayes et al. (1974). Sometimes texture is simply meant as the coarseness, when two textures differ only in scale the magnified one is said to be coarser.

Coarseness is related to the spatial frequency, those textures rich in high spatial frequencies are called fine textured. Those textures rich in low spatial frequency are named coarse textures (see figure 6.1).

Figure 6.1 Fine and coarse textures

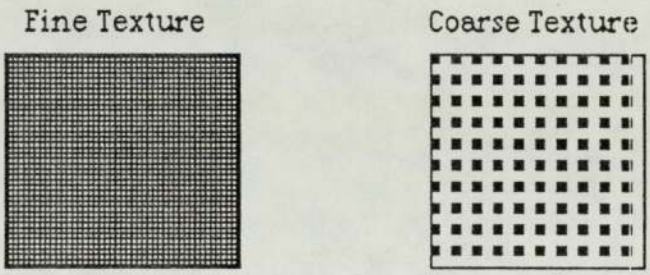

2) Roughness; this is the property related to the total energy of changes in the grey levels of the image. A low energy texture (smooth) will have small amplitude grey level changes, while a high energy texture (rough) will have high amplitude grey level changes (see figure 6.2).

Figure 6.2 Smooth and rough textures

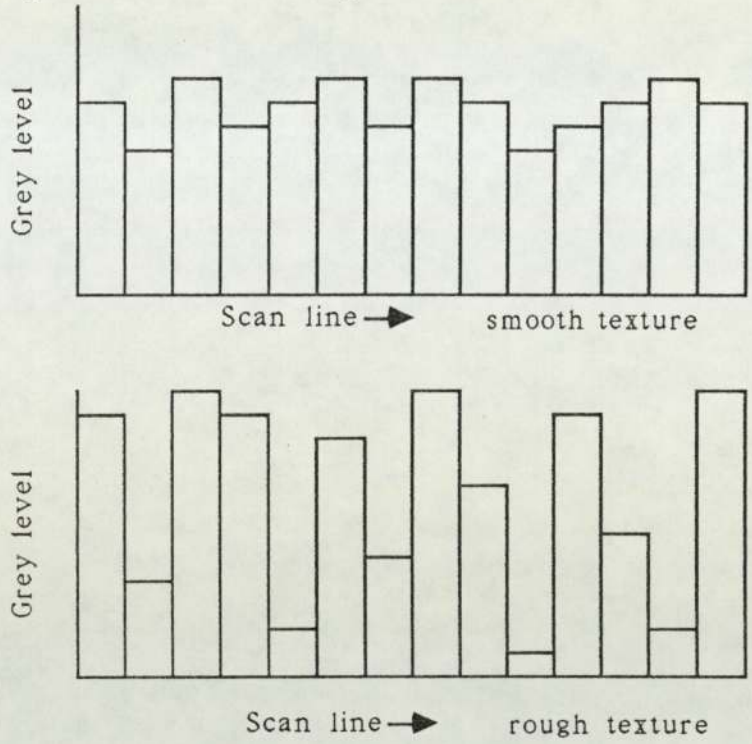

3) Directionality; this is a property over a given region, it involves both the element shape and placement rules. The orientation of the texture pattern does not matter. That is, two patterns which differ only in the orientation should have the same degree of directionality. Figure 6.3 shows a directional and a non-directional texture pattern.

Figure 6.3 Directional and non-directional texture.

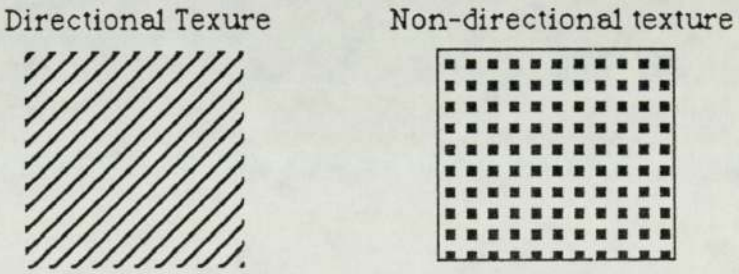

Many different statistical texture measures have been suggested and the following section describes some of them, especially those which have been applied to remotely sensed images.

6.2 First Order Texture Measures

With first order texture measures the pixel (i, j) being considered is directly replaced by some measure of the pixels around it. The properties are calculated in a small kernel in an exactly analogous way to a convolution filtering. Measures may include mean, variance, skewness and kurtosis etc. Kernel sizes are usually small (rarely larger than thirteen by thirteen) and the kernel is invariably square.

Irons and Petersen (1981) compute the local properties in a three by three pixel window for eleven texture measures from each of the four LANDSAT MSS bands. However using an unsupervised clustering technique they were unable to associate any of the classes with terrain types in the image. Hsu (1977) and Hsu (1978) use 23 texture measures for land use mapping of digitised aerial photography. He claims an accuracy in the region of 85-90%. Trendl (1972) uses a laplacian filter to create a texture band. Maurer (1974) uses several first order texture measures on digitised colour aerial photographs in an attempt to discriminate land use types: he concludes that very high accuracies possibly over 95% may be possible. Shih and Schowengerdt (1983) claim success for first order texture measures. Blom and Daily (1982) use mean and variance measures on co-registered SEASAT synthetic aperture radar (SAR) and LANDSAT MSS data. They find the technique useful for increasing classification accuracy. Farr (1983) shows that from SAR imagery, band pass filtering techniques can be used to derive geomorphological information related to drainage density and slope.

6.3 Textural Edgeness

Rosenfeld and Troy (1970) and Rosenfeld and Thurston (1971) conceive of texture not in terms of spatial frequency but in terms of edge per unit area. Rosenfeld and Thurston use the Roberts gradient (the sum of the absolute value of the differences between diagonally opposite neighbouring pixels). Thus a measure of the texture for any sub-image can be obtained by computing the Roberts gradient image for the sub-image, and from it determining the average value of the gradient in the sub-image.

Trendl (1972) measures edgeness by filtering the image with a three by three averaging filter and a three by three laplacian filter. The two values of tone and roughness obtained from the low and high frequency filtered image can be used as textural features.

6.4 Fourier Transform

As previously stated the texture coarseness of an image is related to the spatial frequency. The Fourier transform can be used for texture analysis because it is a technique which measures the spatial frequency of an image.

Fourier transforms can be performed both optically and digitally. Gramenopoulos (1973) recognises terrain types using ERTS-1 MSS imagery of an arid area, and claims an accuracy in the region of 80%. Ramapriyan (1972) uses spatial frequency analysis to examine remotely sensed data. Lendaris and Stanley (1969) use the power spectrum of black and white photography to differentiate between two land use classes: man-made and non man-made in which they claim an accuracy of 98.8%. Indebetouw and Bernado (1981) use an optical Fourier transform using a coherent light source. The light source used has a relatively simple spectra: each line of the spectra is used to highlight a particular spatial frequency in the image. Thus textures corresponding to certain spatial frequencies are highlighted. Blom and Daily (1982) filter images in the Fourier domain and use these as textural bands. They claim that these increase the classification accuracy of their classifier. Evans and Stromberg (1983) use a low pass filtered image followed by a Fourier transform to produce textural bands from SIR-A data of San Rafael Reef, Utah. They use classification maps based on topography and surface roughness to provide a means of relating these parameters to lithology and geomorphology.

6.5 Second Order Texture Measures

There are a number of texture measures which have been described as second order, that is the texture measure is computed from an intermediate texture feature. Second order texture measures include the autocorrelation function, the grey level run length matrix (GLRLM), the so called neighbouring grey level dependency matrix (NGLDM), and the spatial grey level dependency matrix (SGLDM).

6.5.1 Autocorrelation

The autocorrelation function is a feature which measures the size of the texel. The autocorrelation function can be understood with the aid of a simple thought experiment (Haralick, 1979). Imagine two image transparencies on top of one another illuminated with a uniform light source. Measure the average light transmitted by the transparencies. Now rotate one transparency relative to the other and measure the transmitted light as a function of rotation. A graph of these measurements is the two-

dimensional autocorrelation. The autocorrelation is closely related to the power spectrum; they are Fourier transforms of one another.

If the texels of an image are relatively large, then the autocorrelation will drop off slowly with distance. If the texels of the image are small, the autocorrelation will drop off quickly. The autocorrelation function will fall and rise in a periodic manner.

6.5.2 Grey Level Run Length Matrix

A grey level run is defined as a set of consecutive co-linear pixels having the same grey level value. The length of the run is the number of pixels in the run. For a given image or sub-image, a grey level run length matrix can be computed in four different directions. The matrix element (i,j) specifies the number of times that the image contains a grey level j of run length i pixels, see figure 6.4.

Figure 6.4 The four grey level run length matrices which can be calculated from an image.

Image

0	1	2	3
0	2	3	3
2	1	1	1
3	0	3	0

(0, 1) Run Length

Grey Level	1	2	3	4
4	0	0	0	
1	0	1	0	
3	0	0	0	
3	1	0	0	

(-1, 1) Run Length

Grey Level	1	2	3	4
4	0	0	0	
4	0	0	0	
0	0	1	0	
3	1	0	0	

(1, 0) Run Length

Grey Level	1	2	3	4
2	1	0	0	
4	0	0	0	
3	0	0	0	
3	1	0	0	

(1, 1) Run Length

Grey Level	1	2	3	4
4	0	0	0	
4	0	0	0	
3	0	0	0	
5	0	0	0	

This type of texture measure was described by Galloway (1975), who suggested five different measures of texture which can be computed from these run length matrices

(see appendix 2). Some advantages of this method include the fact that the number of calculations is directly proportional to the number of pixels in the image and only two lines of the image need to be held in core at any one time. Galloway illustrated that an accuracy of about 83% for six land use classes (taken from digitised aerial photography) was possible using this method.

6.5.3 Neighbouring Grey Level Dependency Matrix

The NGLDM was first suggested by Sun and Wee (1983), it measures the number of neighbouring pixels with the same grey level as the pixel being examined. The whole of the image array is scanned and an intermediate array shown in figure 6.5 is constructed which has a description of each grey level and the number of equal valued neighbours that pixel has. Thus in figure 6.5 the (3, 3) position of the image has a value of five, it has one nearest neighbour of value five, so the intermediate array is assigned a value of (5, 1) at this position. A two dimensional histogram is then constructed which shows the NGLDM number against grey level. A large value of the NGLDM number in the two dimensional histogram means a smooth image, while a small value of the NGLDM number in the histogram means a rough texture.

Figure 6.5 Computation of the NGLDM

Image

4	4	6	5	4	3
4	4	5	3	0	1
3	3	5	0	0	1
2	0	7	3	3	2
0	0	7	7	3	3
0	1	6	6	2	2

Nearest Neigbour intermediate array

(4, 3) (5, 2) (3, 0) (0, 2)

(3, 1) (5, 1) (0, 2) (0, 2)

(0, 2) (7, 2) (3, 2) (3, 3)

(0, 3) (7, 2) (7, 2) (3, 3)

2-d histogram

NGLDM number

Grey level	0	1	2	3	4	5	6	7	8
0	0	0	4	1	0	0	0	0	0
1	0	0	0	0	0	0	0	0	0
2	0	0	0	0	0	0	0	0	0
3	1	1	1	2	0	0	0	0	0
4	0	0	0	1	0	0	0	0	0
5	0	1	1	0	0	0	0	0	0
6	0	0	0	0	0	0	0	0	0
7	0	0	3	0	0	0	0	0	0

Sun and Wee (1983) describe five texture measures analogous to those of Galloway (1975), which can be calculated from the NGLDM. The advantages of the NGLDM are two-fold, firstly the measures are angularly independent (they change little under rotation of the image). Secondly, as the features are invariant under linear grey level transformation, it is possible to identify two images which have the same texture but different grey tone. Sun and Wee claim a classification accuracy of 79.4% for one texture feature, and an accuracy of 85.0% using two of these texture measures. Little work has been performed on the effectiveness of this texture measure, possibly because of its computational complexity and possibly because the measure may be noise sensitive.

6.5.4 Spatial Grey Level Dependency Matrix

The SGLDM method, also known as the co-occurrence method was first described by Haralick et al. (1973). This is a method which measures the co-occurrence of a pixel of brightness i, against some neighbouring pixel of brightness j. Thus the (i, j)th pixel in the co-occurrence matrix is the number of times a grey level value i occurs adjacent to a grey level j in the sub-image (see figure 6.6). The co-occurrence matrix is square with dimensions Ng by Ng, where Ng is the number of grey levels in the image.

Figure 6.6 The four nearest neighbour (d=1) co-occurrence matrices

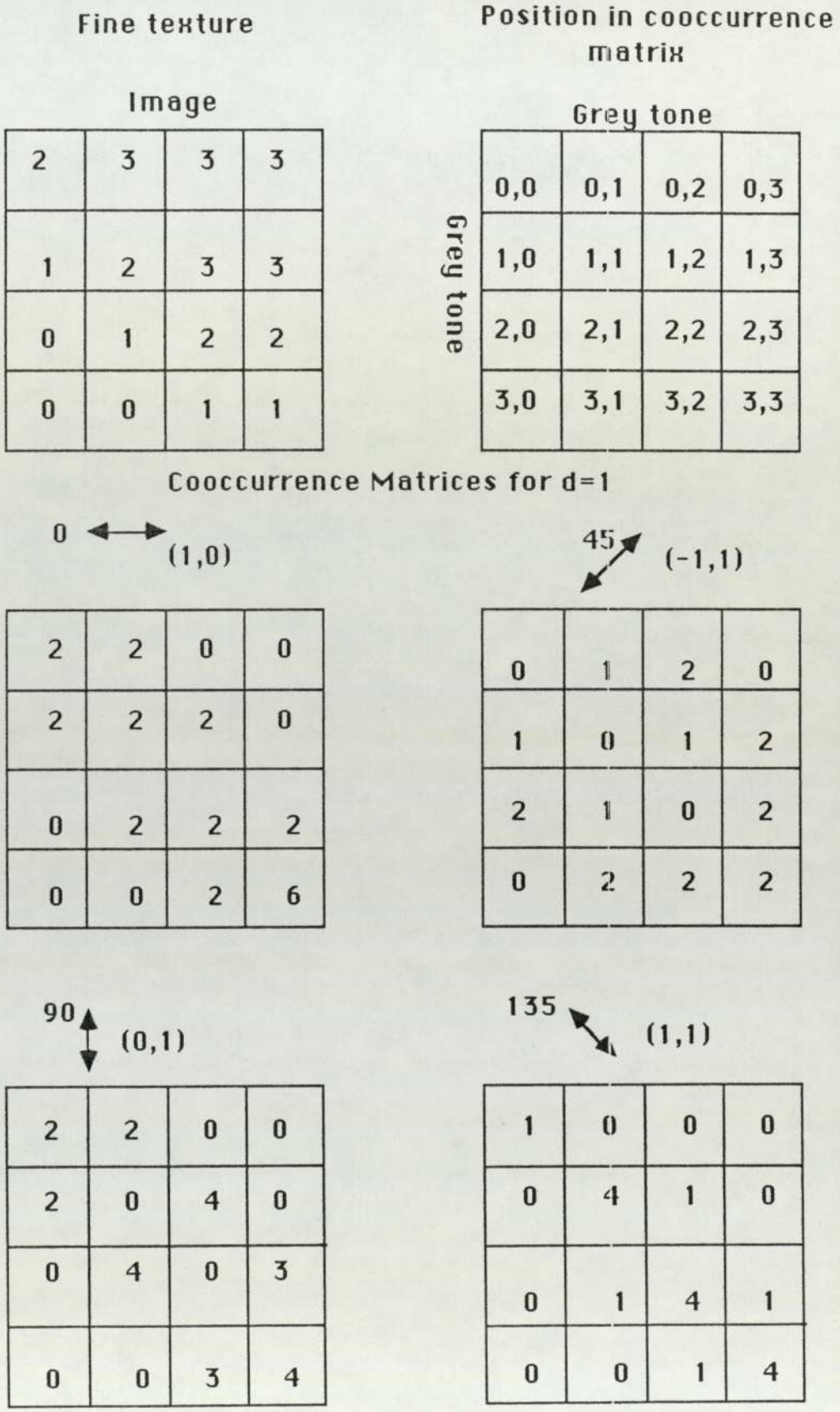

2	3	3	3
1	2	3	3
0	1	2	2
0	0	1	1

0,0	0,1	0,2	0,3
1,0	1,1	1,2	1,3
2,0	2,1	2,2	2,3
3,0	3,1	3,2	3,3

2	2	0	0
2	2	2	0
0	2	2	2
0	0	2	6

0	1	2	0
1	0	1	2
2	1	0	2
0	2	2	2

2	2	0	0
2	0	4	0
0	4	0	3
0	0	3	4

1	0	0	0
0	4	1	0
0	1	4	1
0	0	1	4

The matrix can be measured for immediately adjacent pixels in any one of four directions (see figure 6.6), or can be measured for pixels separated by two or more pixels, again in multiple directions. However, since texture by its very nature is a local property, it does not seem helpful to measure the co-occurrence of pixels separated by distances of more than a few pixels because their semi-variance and hence there textural value must be low.

Smooth textures will have large values close to the main diagonal of the matrix as similar grey levels occur next to each other in smooth textures. Rough textures will have high values far from the leading diagonals as very dissimilar grey levels occur next to each other. Some fourteen texture measures were described by Haralick (these are analogous to those described by Galloway (1975)) but according to Brunner and Veck (1985) only five of these measures are in common usage. A full list of these is given in Appendix 3, but they include the following which are commonly used.

1) Angular Second Moment, this is the simple sum

$$\sum_i \sum_j \{p(i,j)\}^2 \qquad \textit{Equation 6.1}$$

it is smallest when all entries are small that is when all the entries are equally probable. It is largest when one entry is non zero and all the rest are zero. Thus with an image of white noise where all grey level values are equally probable it will give a small value. Fine textures will produce smaller values than coarse textures.

2) Entropy, this refers to the concept of entropy drawn from information theory, not true entropy, though the two have the same formula. It measures the degree of dispersion of the co-occurrence matrix, being largest when all the values of the co-occurrence matrix are equal and smallest when they are unequal. It is calculated by the following formula.

$$-\sum_i \sum_j p(i,j) \log(p(i,j)) \qquad \textit{Equation 6.2}$$

Neither the entropy nor the angular second moment is sensitive to whether the co-occurrence matrix has high values close to, or far from, the main diagonal of the matrix, they are affected only by the spread of values in the whole matrix. Therefore they cannot distinguish coarse texture from fine textures.

3) Contrast, this weights the matrix element with its squared distance from the main diagonal. The value of the function is large when there are large entries far from the

diagonal, and small when all zero elements of the matrix are close to the main diagonal. When all grey level values are equal the contrast becomes zero, this corresponds well with the definition of contrast, which states that a region with no variation has zero contrast. Contrast is calculated by the following equation:

$$\sum_{n=0}^{Ng-1} n^2 \{ \sum_{i=1}^{Ng} \sum_{j=1}^{Ng} p(i,j) \} \qquad \textit{Equation 6.3}$$

4) Inverse Difference Moment, this is similar to contrast but the elements are weighted according to an inverse value of the absolute value of i-j, with an added factor to prevent the function having possible zero denominators. It is small for an area with fine texture, and large for an area with coarse texture. It is given by the following formula:

$$\sum_{i} \sum_{j} \frac{1}{1 + (i-j)^2} p(i,j) \qquad \textit{Equation 6.4}$$

where $n = |i-j|$, and $p(i,j)$ is the value of the (i, j)th position of the co-occurrence matrix.

Haralick and Shanmugan (1973) used the SGLDM to characterise the texture present in digitised photomicrographs of five different reservoir sandstones. They trained the classifier using 143 samples; then on a further 100 samples they tested the accuracy of the texture measure. They found that 89 sandstones were placed in the correct sandstone class. Haralick and Bosley (1973) and Haralick and Shanmugan (1974) used combined spectral and textural data (derived from the SGLDM) for classifying land-use types in ERTS MSS (LANDSAT MSS) image of Monterrey, California. They found a correct classification rate of 83% for their seven land use classes. Chen and Pavlidis (1979) used the SGLDM in conjunction with a split and merge algorithm in order to segment a digitised photograph into textural similar areas. Using LANDSAT MSS imagery Anon (1979) used the SGLDM to classify sandstones which may be associated with uraniferous mineralisation. They found that the third principal component of the imagery had the lithological textural information which they were seeking. Shanmugan et al. (1981) used the SGLDM to characterise textures present in SEASAT SAR imagery. This was found to be a useful technique in spite of the fact that the image blocks used for calculate the co-occurrence matrix had nearly the same mean and standard deviation. Saraph and Inamadar (1982) use the SGLDM for various geological and land cover sites in the Goa region of India. They state that it is a useful tool for the geological interpretation of textures.

6.6 Fractal Based Texture Measures

Pentland (1984) describes the use of fractal based texture measures. The fractal dimension of a surface corresponds quite closely with the intuitive notion of roughness. Thus if a set of three dimensional relief models were created with the same three dimensional relief but with varying fractal dimension, then an increase in roughness would be seen. Pentland used the Brodatz textures (Brodatz, 1966) for establishing the usefulness of fractal based texture measures. Using 16 by 16 non-overlapping subregions a classification accuracy of 84.4% was obtained, as compared with 65% for correlation statistics.

6.7 Comparison of Texture Measures

With the bewildering variety of texture measures that are available it becomes necessary to carefully chose the ones which will probably be the most effective for the particular textures being studied. Two papers have addressed the problem of comparing texture algorithms. In an empirical comparison of first order statistics, second order statistics and Fourier features, Weszka et al. (1976) find that both first and second order statistics perform better than Fourier features. They use a data set consisting of 54 digitised aerial photographs with nine land use classes and 180 LANDSAT MSS image samples belonging to three geological terrain types. Good classification results were obtained on terrain samples representing the geological classes. This confirms the usefulness of texture features for geological remote sensing with satellite data, even in the absence of any spectral information. The study finds that the first and second order texture features perform equally well. They explain the apparent ineffectiveness of the Fourier transform method as being due to the transform treating the image as being periodic, even if it is not. Thus the transforms of terrain samples have high and low values in the horizontal and vertical directions arising from discontinuities between the left and right columns, and the top and bottom rows of the sub-image. The transform therefore does not satisfactorily model the important attributes of texture coarseness and texture roughness and hence achieves very limited success.

Conners and Harlow (1980) make a theoretical comparison of texture algorithms. This study shows that the first and second order measures used are innately more powerful than the Fourier texture measures. They also state that second order texture measures are more powerful than first order texture measures. They say the reason that Weszka et al. (1976) do not find this to be the case was because they use only five texture features which can be derived from the SGLDM, rather than the dozen or more that

could be used. They also find that of the second order texture measures the SGLDM method is more powerful than the GLRLM method. Two reasons for this are that:-

1) The GLRLM is very sensitive to noise, as any noise will tend to break up the run length into arbitrary lengths and therefore give an incorrect measure of texture.

2) The GLRLM does not measure the very important second order probabilities of the form P(i, j) i=j; that is the edge transition information.

Ulaby et al. (1986) use SAR imagery to compare various texture algorithms. They find that first order texture measures combined with tonal measures achieve a maximum classification accuracy of 72% for land cover types, but that this level of accuracy was obtainable only at the cost of significantly degrading the spatial resolution of the imagery. In contrast, second order statistics provided a classification accuracy of 88% with only a slight decrease in the spatial resolution of the imagery. A second study shows that the use of second order texture measures for five forest types improves classification accuracy from 75% for tonal data only, to 93% for tonal and textural data together.

The results show that Fourier features perform poorly compared with first and second order measures. Conners and Harlow (1980) show that second order texture measures perform better than first order texture measures, and this is further underlined by Ulaby et al. (1986). Conners and Harlow also show that the SGLDM texture measure is theoretically a more powerful second order texture measure than the GLRLM texture measure.

6.8 Results of Texture Analysis

During the course of this study four different types of texture measure were investigated for each of the two test sites (see chapter 4 for the description of each test site) these were: 1) first order measures, 2) edge measures, 3) grey level run length measures, and 4) spatial grey level dependency measures. Texture analysis was undertaken on the LANDSAT MSS and TM data, not the SIR-A data. This is because of the strong speckle on the radar data which would give rise to poor results using such simple statistical models. In each case three texture features were used to describe the texture of each image. The texture measures were derived by reference to the coincident spectral plots (figures 5.6 to 5.8) using the band of LANDSAT (MSS or TM) data which showed both the least atmospheric influence and the greatest separation of classes in each test site. The assumption was made that these bands would show the greatest separation of texture types. In each case it was found that the longest

wavelength available had these attributes, in the case of the MSS this was band 7 (near infra red 0.8 μm to 1.1 μm) and in the case of the TM it was band 7 (middle infra red 2.08 μm to 2.35 μm) .

1) First order texture measures; the three features used were a) the mean, b) the variance, and c) the logarithm of the variance. These three features were chosen for their simplicity of calculation.

2) Edge texture measures; the three features used were derived from convolution filtering of the input image, they were a) Sobel (magnitude only), b) Prewitt (direction only), and c) the Roberts gradient. These features were chosen because of their common use in digital image processing (Rosenfeld and Thurston, 1971 and Sutton and Hall, 1972).

3) Grey level run length; five different features in four different directions were suggested by Galloway (1975) which could be derived from this texture measure. To reduce the dimensionality of the data set the four different directions were averaged to produce a generalised run length matrix. This reduces the dimensionality by a factor of four and produces a generalised matrix. Because direction is dependent on the frame of reference (that is the direction it is viewed from), whereas texture is not dependent on this, therefore, a rotated texture should give the same texture measure as one which has not been rotated. The optimum three features were selected by performing a minimum distance to means classifier (because of its efficiency and because of the singular matrices produced by the relatively small training areas) using every combination of three out of the five texture features and finding the maximum accuracy. The results were as follows:

Test Site1 MSS	**Test Site 2 MSS**
1. Long Run Emphasis	1. Short Run Emphasis
2. Grey Level Nonuniformity	2. Grey Level Nonuniformity
3. Run Length Nonuniformity	3. Run Percentage

Test Site 2 TM

1. Short Run Emphasis
2. Long Run Emphasis
3. Run Length Nonuniformity

It is interesting to note that no one texture feature occurs in all three sets of imagery.

4) With the Spatial grey level dependency measures, there are many variables which can be altered. These include, the number of grey levels, the direction, the distance over which it is computed, and the fourteen features which Haralick et al. (1973) described. For the sake of convenience in terms of length of calculation and storage, the number of grey levels was restricted to 16 (giving 16 by 16 output array from a 8 by 8 input array). As in the case of the run length measure the average of four directions was used to produce a generalised co-occurrence matrix. It was decide that only distance one (nearest neighbour) features would be investigated, since it was felt that texture by its very nature is a local property, and hence distant neighbours should have little influence on the texture. A minimum distance to means classifier (for the reasons given earlier) was used on every three band combination of thirteen of the fourteen texture measures (maximal correlation coefficient was not investigated) to find the optimum band combination. The results were as follows.

Test Site 1 MSS

1. Angular Second Moment
2. Contrast
3. Difference Entropy

Test Site 2 MSS

1. Angular Second Moment
2. Inverse Difference Moment
3. Sum Entropy

Test Site 2 TM

1. Angular Second Moment
2. Entropy
3. Difference Entropy

It is interesting to note that in each case the angular second moment (ASM) was judged to be among the best three features for all types of imagery in both test sites. Also in each case at least one entropy based feature is present. This means that both the coarseness of the texture (derived from the ASM) and the roughness of the texture (derived from the entropy based features) are being measured.

In the tables 6.1 to 6.9 the following nomenclature is used to denote the texture measures investigated. FOT are first order texture measures (mean, variance, logarithm variance); EDGE are edge based texture features (Sobel, Prewitt, Roberts); GLRLM are three texture features based on the GLRLM (see previous discussion for which features are used); SGLDM are three texture features based on the SGLDM (see previous discussion for which features were chosen).

Table 6.1 classification accuracies for test site 1, using the minimum distance rule with MSS, texture bands and SIR-A data.

	Class 1	Class 2	Class 3	Class 4	Class 5	Average
4 bands MSS + EDGE	0.84	0.58	0.12	0.48	0.39	48.12
4 bands MSS + EDGE+SIR-A	0.74	0.55	0.58	0.35	0.34	51.06
4 bands MSS + FOT	0.74	0.19	0.49	0.29	0.49	48.32
4 bands MSS + FOT+SIR-A	0.95	0.19	0.49	0.29	0.49	48.32
4 bands MSS + GLRLM	0.76	0.93	0.29	0.16	0.45	51.89
4 bands MSS +GLRLM+SIR-A	0.75	0.86	0.38	0.20	0.48	52.16
4 bands MSS + SGLDM	0.23	0.71	0.39	0.11	0.66	42.06
4 bands MSS +SGLDM+SIR-A	0.23	0.71	0.47	0.60	0.60	42.36

In test site 1, in all but one case, the addition of texture measures to the minimum distance classifier has a small effect of increasing the accuracy of the classifier over the same classifier using only tonal properties (Table 6.1). The exception being the SGLDM features which actually decrease accuracy by some 6%. The addition of SIR-A data has a much greater effect in increasing classification accuracy the texture measures.

Table 6.2 classification accuracies for test site 1, spectral shape classifier, using LANDSAT MSS data, SIR-A data and texture data.

	Class 1	Class 2	Class 3	Class 4	Class 5	Average
4 bands MSS +3EDGE+SIR-A	0.08	0.78	0.01	0.91	0.19	39.82
4 bands MSS +3 FOT+SIR-A	0.90	0.83	0.02	0.98	0.09	56.31
4 bands MSS +GLRLM+SIR-A	0.10	0.83	0.00	0.97	0.09	40.22
4 bands MSS +SGLDM+SIR-A	0.54	0.86	0.01	0.89	0.12	49.09

The spectral classifier performs poorly for first order and edge based texture measures for test site 1 (Table 6.2), but it performs relatively well for second order texture measures. The SGLDM based features prove to be the most accurate, achieving results which are superior to those of the minimum distance to means classifier. In most cases the classifier classifies two or three classes very well, but it is unable to classify all five classes with any degree of consistency. It is able to discriminate classes 2 and 4 consistently well and classes 3 and 5 consistently poorly.

Table 6.3 classification accuracies for test site 1 using maximum likelihood rule for spectral data and minimum distance rule for texture data.

	Class 1	Class 2	Class 3	Class 4	Class 5	Average
4 bands MSS + EDGE	0.61	0.94	0.26	0.75	0.48	60.64
4 bands MSS + EDGE+SIR-A	0.64	0.94	0.39	0.76	0.50	64.32
4 bands MSS + FOT	0.63	0.94	0.26	0.72	0.47	60.15
4 bands MSS + FOT+SIR-A	0.64	0.94	0.39	0.75	0.49	64.26
4 bands MSS + GLRLM	0.61	0.94	0.27	0.48	0.50	55.90
4 bands MSS +GLRLM+SIR-A	0.64	0.94	0.39	0.65	0.50	62.36
4 bands MSS + SGLDM	0.60	0.94	0.24	0.76	0.51	61.12
4 bands MSS +SGLDM+SIR-A	0.64	0.94	0.39	0.76	0.50	64.40

Map 6.1 Maximum likelihood classification of test site 1 using LANDSAT MSS and SIR-A data, with SGLDM data classified according to minimum distance rule.

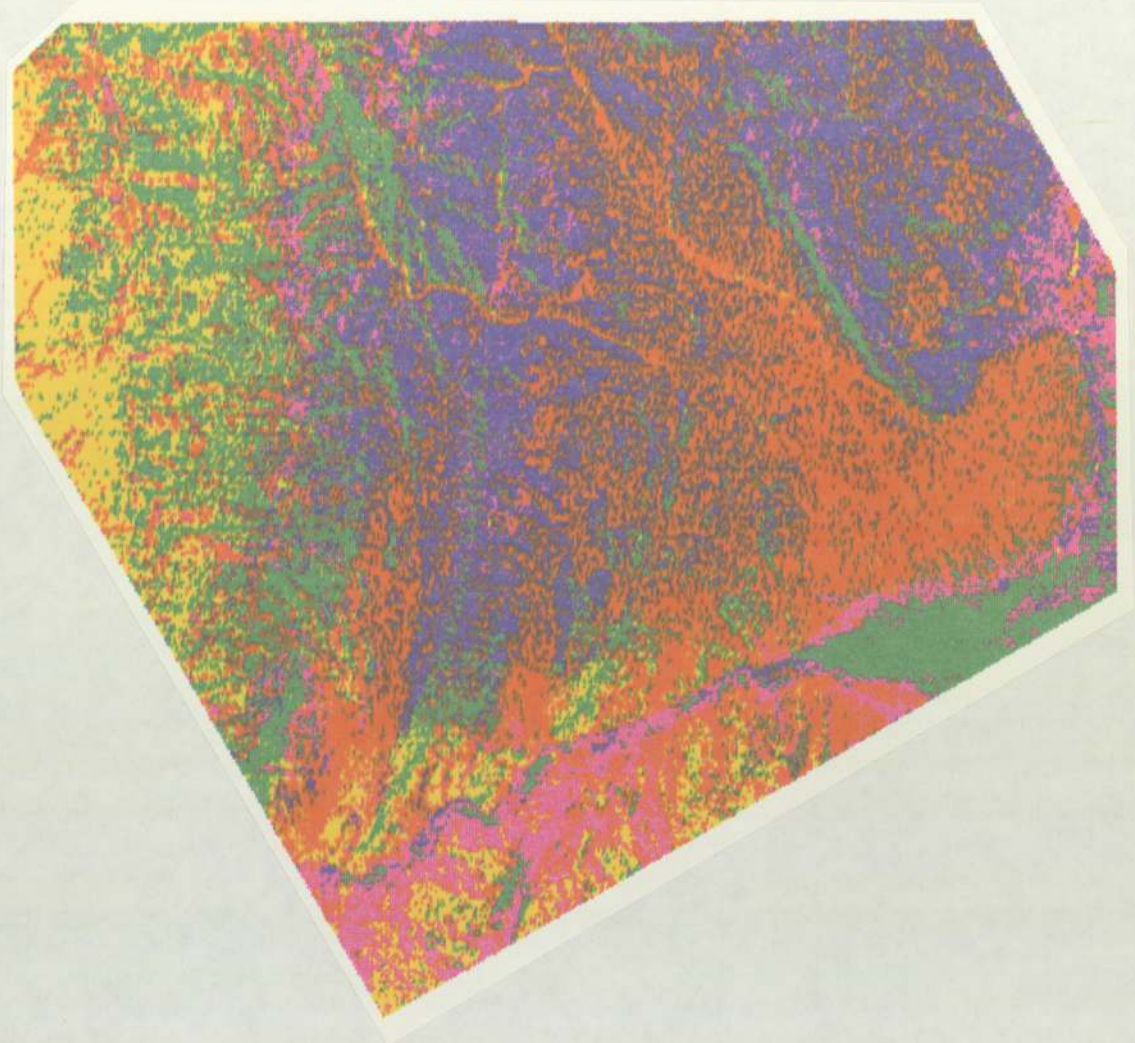

In the case of the maximum likelihood classifier it was not possible to simply add the texture bands to the tonal classifier because of the small size of the training areas used, this gave rise to singular matrices for the texture features because of the 8 by 8 pixel blocks used as the basis of the texture measures. Therefore a modified maximum likelihood rule was used. Thresholds were placed on the classifier so that pixels with a low probability of belonging to any class were left unclassified. These unclassified pixels were then, using only textural features placed in a class according to minimum distance rule. The assumption behind this is that the textural information is taken from a small region around each pixel and is therefore more representative than the tonal features which have proved inconclusive.

The maximum likelihood results for test site 1 are given in table 6.3, they show that the addition of texture features in the way previously described has little or no effect to the classification accuracy. Classification accuracy is not increased in any case by an amount which could be described as significant; the GLRLM features in fact decrease accuracy by some 5%. The best case is the addition of SGLDM texture measures and SIR-A data, this is shown in Map 6.1.

Table 6.4 classification accuracies for minimum distance algorithm for test site 2

	Class 1	Class 2	Class 3	Class 4	Class 5	Average
4 bands MSS + EDGE	0.50	0.64	0.58	0.16	0.38	45.30
4 bands MSS + EDGE+SIR-A	0.42	0.77	0.54	0.15	0.39	45.36
4 bands MSS + FOT	0.15	0.47	0.63	0.08	0.49	41.31
4 bands MSS + FOT+SIR-A	0.21	0.85	0.64	0.10	0.49	45.55
4 bands MSS + GLRLM	0.48	0.73	0.38	0.67	0.45	42.21
4 bands MSS +GLRLM+SIR-A	0.54	0.78	0.39	0.08	0.53	46.23
4 bands MSS + SGLDM	0.36	0.75	0.20	0.15	0.33	35.61
4 bands MSS +SGLDM+SIR-A	0.48	0.75	0.20	0.26	0.35	39.66

The classification accuracy for test site 2, using LANDSAT MSS and SIR-A data, again shows a slight decrease using texture measures for the minimum distance algorithm (Table 6.4). Again the SGLDM features lower the accuracy by a significant amount. Interestingly addition of SIR-A to the texture features increase the accuracy, this is the reverse of the case found when the SIR-A data is added to just the tonal features.

Table 6.5 classification accuracies for test site 2, spectral shape classifier using LANDSAT MSS data, SIR-A data and texture data.

	Class 1	Class 2	Class 3	Class 4	Class 5	Average
4 bands MSS +3EDGE+SIR-A	0.10	0.53	0.93	0.13	0.04	34.60
4 bands MSS +3 FOT+SIR-A	0.19	0.56	0.00	0.04	0.87	33.27
4 bands MSS +GLRLM+SIR-A	0.50	0.94	0.00	0.00	0.57	40.14
4 bands MSS +SGLDM+SIR-A	0.34	0.75	0.34	0.54	0.24	44.80

The results for the spectral shape classifier in test site 2 are given in table 6.5. They show that second order texture measures perform better than first order and edge based texture measures. Again the SGLDM based features perform better than the GLRLM based features. The classifier seems able to discriminate just two classes with any consistency, these are classes 2 and 5. In the best case example with the SGLDM texture features, the classification accuracy is comparable with the minimum distance to means classifier, furthermore it is able to distinguish all classes at greater than 20% accuracy (20% is what a random number generator would achieve).

Table 6.6 classification accuracies for test site 2 LANDSAT MSS and SIR-A data using maximum likelihood rule for spectral data and minimum distance rule for texture data.

	Class 1	Class 2	Class 3	Class 4	Class 5	Average
4 bands MSS + EDGE	0.55	0.46	0.63	0.72	0.62	59.34
4 bands MSS + EDGE+SIR-A	0.77	0.54	0.61	0.80	0.70	68.38
4 bands MSS + FOT	0.56	0.47	0.62	0.71	0.62	59.58
4 bands MSS + FOT+SIR-A	0.77	0.53	0.62	0.80	0.70	68.53
4 bands MSS + GLRLM	0.56	0.55	0.62	0.41	0.60	50.27
4 bands MSS +GLRLM+SIR-A	0.77	0.55	0.62	0.65	0.70	65.94
4 bands MSS + SGLDM	0.54	0.46	0.63	0.73	0.62	59.61
4 bands MSS +SGLDM+SIR-A	0.77	0.54	0.62	0.86	0.70	68.60

The addition of texture according to a minimum distance to means algorithm to the maximum likelihood classification of test site 2 using LANDSAT MSS data does not significantly alter the classification accuracy (Table 6.6). The best case is the addition of the SGLDM based texture features and SIR-A data, but the increases in accuracy are almost negligible, this best case is given in map 6.2.

Map 6.2 Maximum likelihood classification of test site 2 using LANDSAT MSS and SIR-A data, with SGLDM data classified according to minimum distance rule.

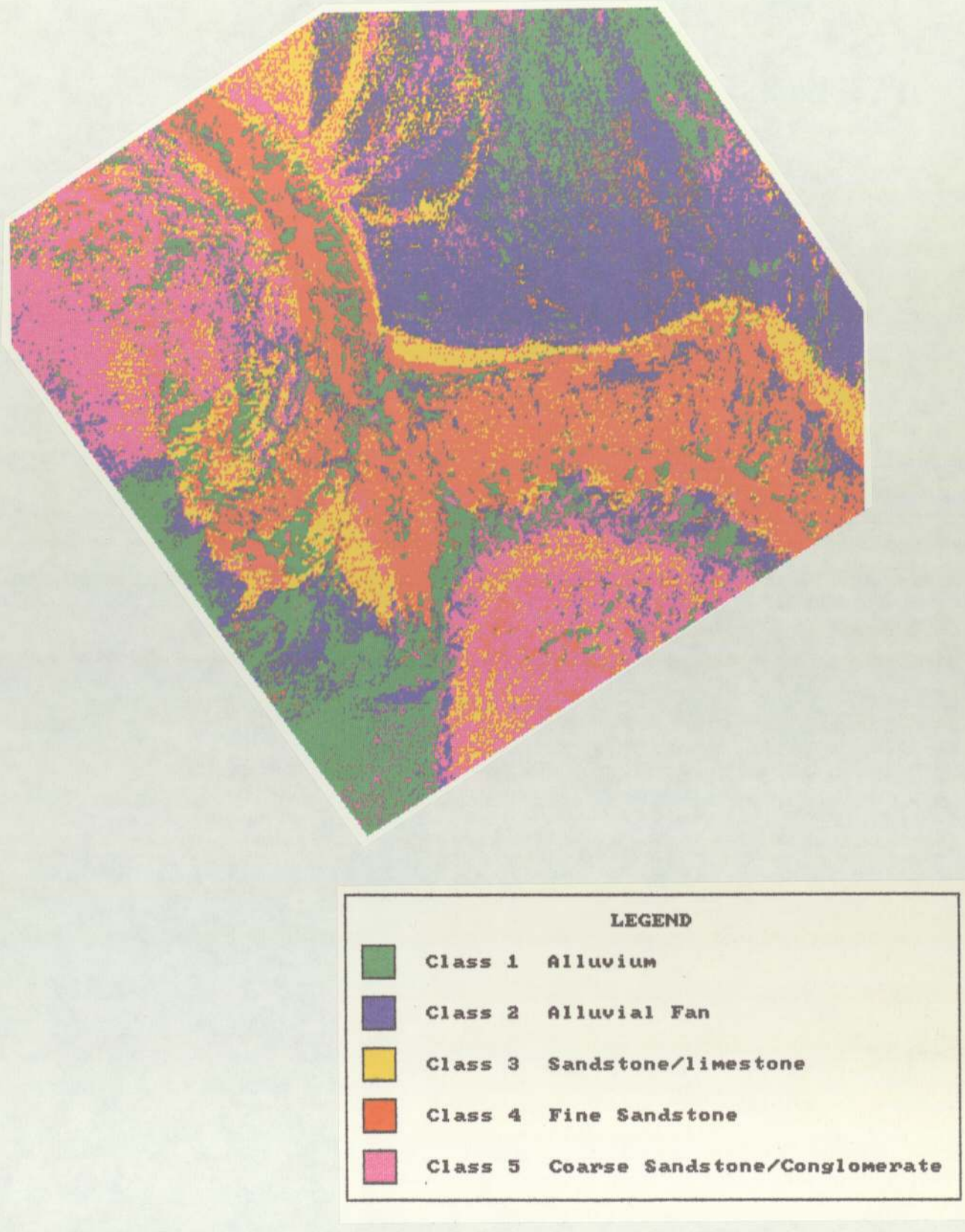

Table 6.7 Minimum distance to means classifier test site 2, using LANDSAT TM, SIR-A and texture data.

	Class 1	Class 2	Class 3	Class 4	Class 5	Average
6 bands TM +3 EDGE	0.77	0.65	0.55	0.56	0.29	56.37
6 bands TM +3EDGE+SIR-A	0.77	0.65	0.55	0.57	0.29	56.53
6 bands TM +3 FOT	0.73	0.32	0.80	0.51	0.28	52.70
6 bands TM +3 FOT+SIR-A	0.75	0.40	0.80	0.53	0.31	55.65
6 bands TM + GLRLM	0.60	0.26	0.52	0.88	0.48	54.91
6 bands TM +GLRLM+SIR-A	0.60	0.27	0.52	0.89	0.48	54.99
6 bands TM + SGLDM	0.64	0.44	0.77	0.82	0.58	65.14
6 bands TM +SGLDM+SIR-A	0.65	0.44	0.77	0.83	0.58	65.16

The addition of texture data to the minimum distance to means classifier for the TM data of test site 2 shows significant increases in the accuracy for all texture features (Table 6.7). Increases in accuracy occur for all classes and particularly for class 2, which previously had an accuracy of 34%. The largest increases in accuracy occur for the SGLDM based texture features (over 14% increase), while the lowest increase is for the GLRLM based features. Interestingly the addition of SIR-A data does not increase the classification accuracy of the LANDSAT TM and texture measures. It appears that most of the increase in accuracy of the textural features is the same increase that would be caused by the radar data.

Table 6.8 results for spectral shape classifier LANDSAT TM data with SIR-A and texture

	Class 1	Class 2	Class 3	Class 4	Class 5	Average
6 bands TM +3EDGE+SIR-A	0.06	0.82	0.50	0.55	0.04	38.14
6 bands TM +3 FOT+SIR-A	0.00	0.86	0.63	0.23	0.03	34.95
6 bands TM +GLRLM+SIR-A	0.72	0.19	0.23	0.00	0.27	28.22
6 bands TM +SGLDM+SIR-A	0.10	0.71	0.73	0.86	0.04	49.16

The results of the spectral shape classifier for the TM, radar and texture data are given in table 6.8, these show that the classifier generally produces poor results. Again (as in all previous cases) the SGLDM features produce the highest accuracy while the GLRLM features produce the lowest accuracy. In the case using the SGLDM measures, the overall accuracy is comparable with minimum distance results. Good accuracy is achieved for classes 2, 3 and 4, while classes 1 and 5 have very low accuracies, class one being confused largely with class 2 and class 4 being confused with class 5

Table 6.9 Maximum likelihood classifier for test site 2 using LANDSAT TM, SIR-A and texture data.

	Class 1	Class 2	Class 3	Class 4	Class 5	Average
6 bands TM +3 EDGE	0.92	0.64	0.41	0.93	0.85	75.14
6 bands TM +3EDGE+SIR-A	0.93	0.63	0.42	0.95	0.87	76.02
6 bands TM + GLRLM	0.91	0.61	0.29	0.93	0.78	70.20
6 bands TM +GLRLM+SIR-A	0.92	0.58	0.29	0.93	0.80	70.65
6 bands TM + SGLDM	0.95	0.69	0.42	0.95	0.89	77.73
6 bands TM +SGLDM+SIR-A	0.96	0.66	0.42	0.96	0.90	78.10

The TM for test site 2 has the same training areas as the MSS for test site 2, since the TM has pixels twice the size as the MSS each training area has twice as many pixels. It was therefore

Map 6.3 Maximum likelihood classification of test site 2 using LANDSAT TM, SIR-A and SGLDM texture data.

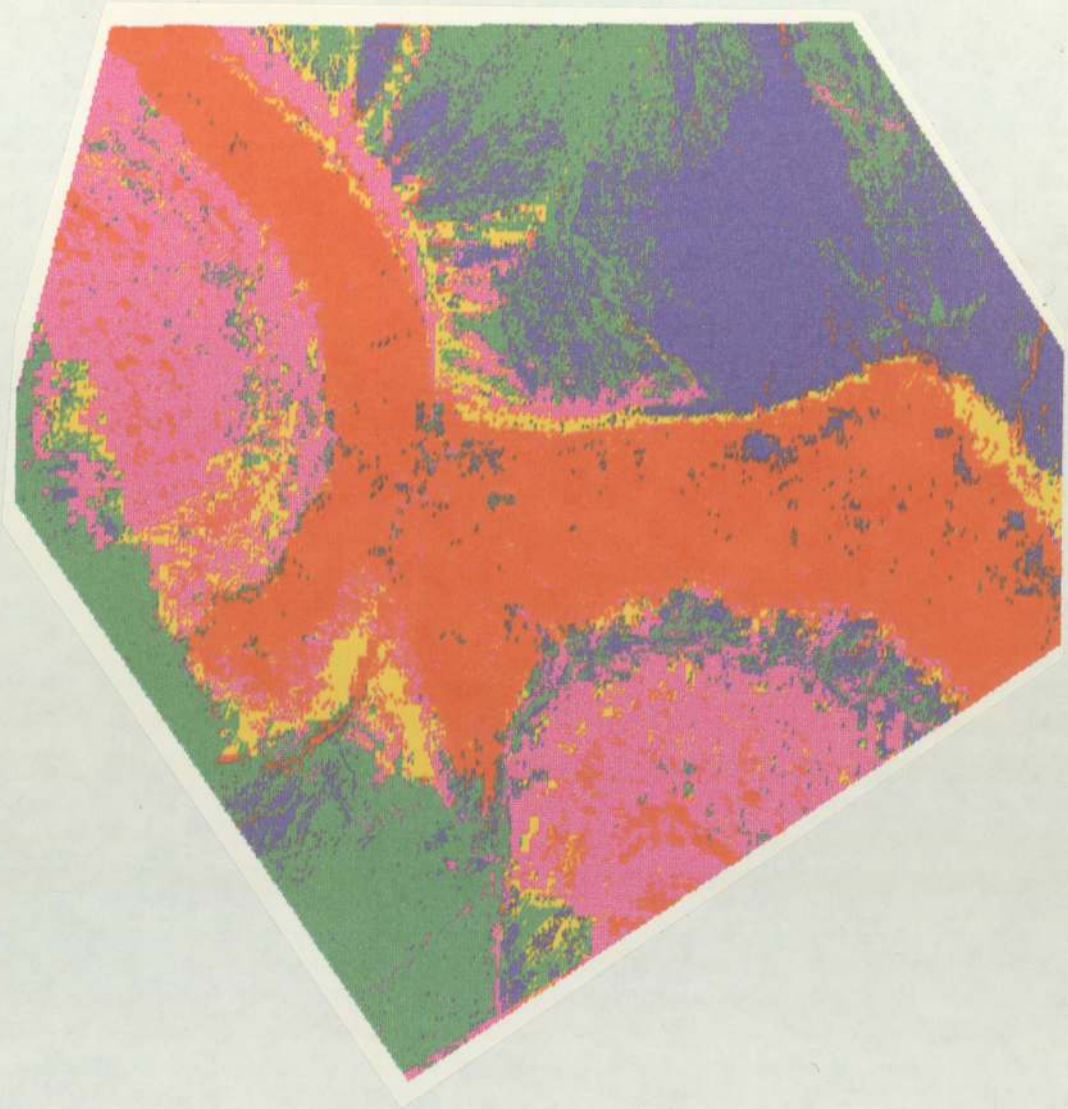

LEGEND

Class 1 Alluvium

Class 2 Alluvial Fan

Class 3 Sandstone/limestone

Class 4 Fine Sandstone

Class 5 Coarse Sandstone/Conglomerate

possible to simply add the texture bands to the maximum likelihood classifier in just the same way as adding spectral bands (except in the case of first order texture measures). The results are given in table 6.9. In the case of both the edge texture measures and the SGLDM texture measures significant increases in the classification accuracy are achieved (in the case of SGLDM this increase is of the order of over 6%). The GLRLM based features perform poorly when compared with the other texture measures. The best case occurs for six bands of TM with SGLDM texture measures and SIR-A data, this is shown in map 6.3.

6.9 Timings of Classifiers

The timings of classifiers with texture measures added relative to the accuracy is given in figure 6.4. The timings are given relative to the fastest classifier (the minimum distance) which took some 130 seconds on the VAX 8650 processor. The results show that the spectral shape classifier performs poorly when compared with the minimum distance or maximum likelihood, having lower accuracy than both and taking 1.5 times longer to calculate than the minimum distance classifier. The maximum likelihood classifier has a significantly higher accuracy than the minimum distance algorithm, but the classification time is increased by over 100 fold.

Figure 6.7 Timings versus accuracy for supervised classifiers using six bands of TM and SIR-A data and three SGLDM texture features

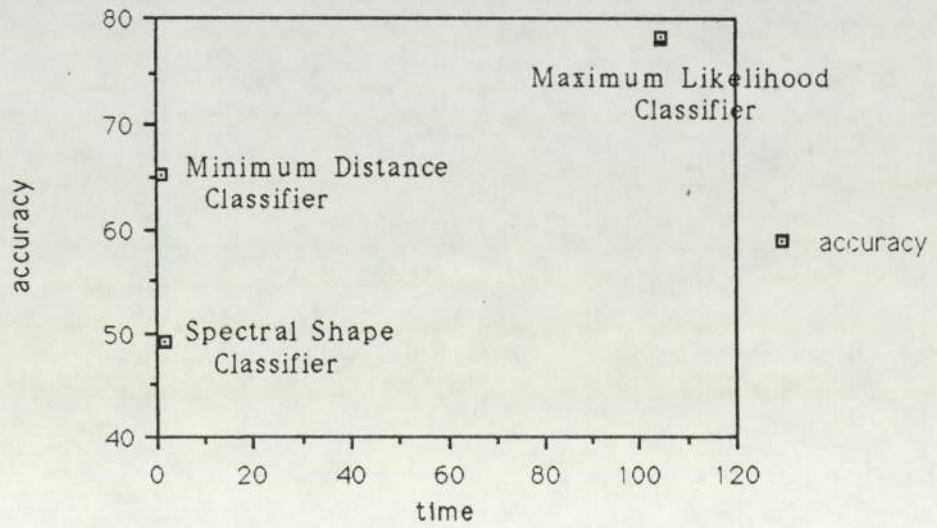

6.10 Summary

Several texture measures have been described which have been used in digital image processing. These texture features have received relatively little attention in the field of remote sensing. A review of literature has shown that second order texture measures are both theoretically and experimentally more powerful than first order or Fourier based texture measures.

The results from the Spectral shape classifier have been reported in this chapter, and have shown that in favourable circumstances this classifier can produce results which are comparable with the minimum distance to means classifier. In circumstances where the texture measures used in the classifier are poor, the results of the classifier are relatively disappointing.

Results for the TM show that in most cases the addition of texture measures does significantly increase the classification accuracy. The highest increase in classification accuracy being due to the second order SGLDM based texture measures (increases in accuracy of some 15% are reported). However, results for the LANDSAT MSS data show only small gains in accuracy, and in certain cases small falls using texture features. Furthermore, it was found that second order texture measures performed poorly when compared with first order texture measures. This is in direct contradiction with the literature but is probably due poor spatial resolution of the imagery used. The results for the TM are in agreement with the literature, the difference with the results for the MSS are therefore probably due to the increased spatial resolution of the TM over the MSS and also to the better positioning of the spectral bands on the TM sensor for discriminating lithology. It is probable that the resolution of the MSS is too low to discriminate distinctive textures in the lithologies of each test site with a near infra red band.

Chapter 7
Contextual Analysis

7.0 Introduction

Whereas texture refers to the spatial variation within a contiguous group of pixels, the context of a pixel refers to its spatial arrangement with pixels in the remainder of the scene. Thus contextual classification of any pixel can potentially involve the use of any other pixel or group of pixels in the image (Gurney and Townshend, 1983). Contextual information is not only pixel based property, it can also be a region based property, that is groups of pixels can be said to be out of context with their surroundings. Context conveys information about the size, shape and position of a pixel or group of pixels in an image. Human photo-interpreters have long exploited context very thoroughly using their knowledge of the world to increase the accuracy of classification. However, context has been defined in very imprecise terms and has received relatively little investigation. Furthermore, it is not immediately obvious which procedures utilise contextual information.

To take a geological example it might be expected that a sandstone class in an image will occur near other sedimentary rocks, and further away from igneous or metamorphic rocks. Clearly this will not always be true, but it is a useful piece of knowledge about the distribution of lithology in the real world. Similarly isolated pixels of one class completely surrounded by pixels of another class can be thought of as out of context with their surroundings.

A contextual decision rule can be applied at three different times to imagery, these are: prior to classification, in which case the spectral or textural properties of the other pixels can be considered. Secondly at the time of classification of the data, in which case the probability of a neighbourhood of pixels is taken into account. Finally contextual features can be used on data which has already been classified, and this is also known as spatial post processing. An example might be that some preliminary classification which is amended by some iterative technique, a process known as relaxation.

7.1 Contextual Properties

According to Gurney and Townshend (1983) there are four different types of spatial (contextual) relationship . These are:

1) Distance. Measures that take into account distance are relatively common, they work on the assumption that a pixel is likely to be associated with pixels of its own class and that isolated pixels which are separated by some distance from an object of their own class are likely to be misclassified. For example a pixel of water surrounded by other water pixels is more likely than a pixel of water surrounded by land.

2) Direction. Directional contextual operators work on the assumption that pixels are likely to be associated with pixels separated by some angular direction or are less likely to be associated with pixels at some angular direction. Both distance and direction can be applied to single pixels or objects and therefore these properties can be used either before or after classification.

Figure 7.1 Types of contextual relationship (after Gurney and Townshend, 1983)

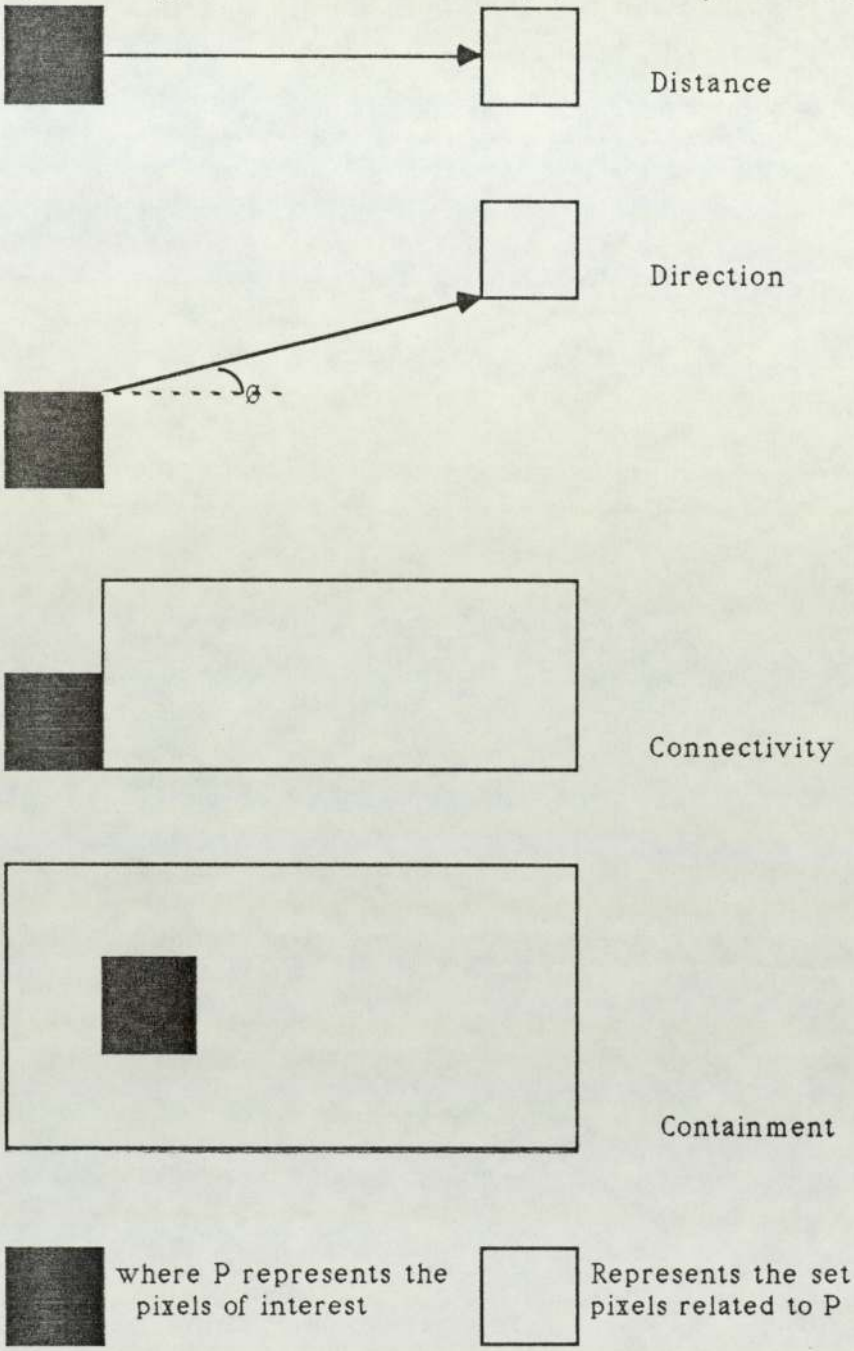

3) Connectedness. Connectedness is a property of objects which are normally associated with each other in an image. An example of connectedness might be a lava flow occurring immediately adjacent to a volcanic centre or a debris cone occurring at the break of slope at the base of a mountain range (see figure 7.1).

4) Containment. Containment is a property of objects which can be found to contain or, are contained by other objects. An example of containment might be an area

of lake surrounded by an area of shore deposits, this type of arrangement is especially common around playa lakes where seasonal flooding followed by droughts causes large rises and falls in lake area. Connectedness and containment apply to objects only and therefore can only, be used after some form of initial classification; that is after objects have been recognised and assigned to a particular class.

To these four properties perhaps two others should be added, namely, size and shape. These can be particularly important in certain remote sensing images, especially where the scale of the image is known with a high degree of certainty. A simple geological example of size as a contextual operator, might be the volcanic centres seen in the LANDSAT MSS image of northern Chile used by Oldfield and Elgy (1987) these are comparatively large (greater than 100 pixels in size), thus if a small number of pixels are assigned to this class than they could be said to be out of context. Generally the strictly reconnaissance geological units being classified in LANDSAT MSS imagery are unlikely to have a small areal outcrop, and such an approach is likely to be useful. Size is an example of a contextual feature which can only be measured an initial classification procedure.

The same volcanic vents have a distinctive circular to sub-circular shape, and these are surrounded by radial lava flows which have lobate shape peripheries. A further geological example of shape would be alluvial fan which almost always have a characteristic fan or conical shape. Furthermore, the three dimensional shape of an alluvial fan is even more characteristic. Objects can display two properties of shape, the first is the overall shape of the boundary, that is whether it is rough or smooth in outline. Secondly there is the overall body shape of the object. For example, a volcanic vent with radial lava flows will normally have a very irregular (rough) boundary, while an ephemeral lake will have a much smoother boundary, both the lake and the volcano often have a overall circular body shape. However, boundary pixels have the lowest likelihood of being correctly classified, therefore the roughness of an object is not a property which is likely to yield very much information about the object. The overall body shape is important and a 'fuzzy' representation of the shape, possibly in the form: is one dimension much greater than the other dimension of an object, or is it fan shaped or circular. It might be possible to model the shape of these features (for example in the way described by Davis, 1973) and thereby to increase the classification accuracy. However, many cases the measurement of shape requires a stereoscopic data set to give the three dimensional properties of the shape. Therefore, shape based contextual measures will become very important with stereoscopic satellite data, such as

SPOT, they are less useful for non-stereoscopic data, such as LANDSAT MSS and SIR-A used in this study, therfore no shape features were modelled.

7.2 Contextual Algorithms

A variety of contextual classifiers and reclassifiers are available which can provide improvements in accuracy beyond those achieved by simple 'per pixel' classifiers. Most pixel based reclassifiers are based on the use of windows of varying sizes similar to low pass filters. A widely based assumption is that pixels of a given class are likely to be surrounded by pixels of the same class. This assumption is made by Thomas (1980) and by Rothery (1983).

Wharton (1982) uses a simple mode filter (also known as a majority filter, Mather, (1987)) as a contextual post classifier, this is simply the most commonly occurring class in a N by M window, (where N and M are odd integers). In figure 7.2, where N=M=3, with four possible classes (1, 2, 3 and 4), the vector of component frequencies (that is the histogram) corresponding to the given window is 5 of class 1, 3 of class 2, 0 of class 3, 1 of class 4.

Figure 7.2 The mode filter (after Wharton, 1982)

1	2	2
2	1	1
4	1	1

The central pixel in figure 7.2 therefore remains a 1, since it is the most commonly occurring pixel in the window. This is an example of a contextual rule that can take place both before or after the classification procedure. Wharton claims that the inclusion of this postclassification filter improves the classification accuracy by up to 20% for his study, using high resolution aerial photography.

The median filter can be thought of as a simple smoothing contextual filter, as it removes isolated stray pixels which often tend to clutter classified images. These isolated pixels represent small scale variations or noise, which tend to lead to loss of general detail and are therefore undesirable on thematic maps. The advantage of the median is that it has an edge preserving effect as well as a smoothing effect, therefore

well defined edges are little altered. The effect of such filtering is investigated by Oldfield and Elgy (1987).

Davis and Peet (1977) use a smoothing technique based on the size of the classified objects in the image. For example, all connected regions in the image are identified, and any region smaller than a certain size are declassified (see figure 7.3). Thus in the example a minimal area of five pixels was chosen as minimum class size, the pixels of class three (enclosed by the dotted line) do not form a sufficiently large region and are therefore declassified. The pixels can then be reclassified according some form of mode filter as described above. This is a somewhat crude example, as different size thresholds could be set for each class depending on the prior knowledge on the size of the object being sought.

Figure 7.3 The minmal area replacement filter (after Davis and Fleet, 1977)

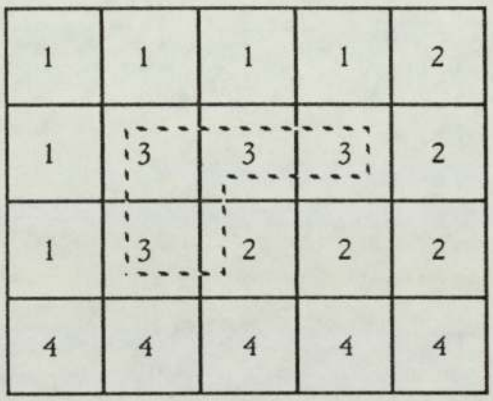

Related to the idea of a minimal area replacement is the idea that the largest errors of classification occur at the edges or boundaries of objects. Therefore a simple contextual rule would be to replace all boundary pixels and label them as unclassified. In figure 7.4 the area enclosed by the shading is a boundary area, where the boundary is interleaved and clearly misclassification is likely. A contextual operator could find all edge and boundary pixels and replace them as unclassified. This form of contextual rule would have the additional effect of replacing all isolated pixels. Following the first sweep to remove boundary pixels, the pixels could be reclassified according to some mode rule, as in the case of the minimal area replacement method.

Figure 7.4 The boundary pixels which would be declassified by the contextual boundary rule.

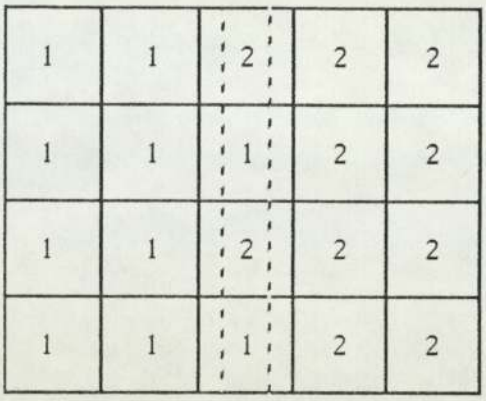

Thomas (1980) uses a simple 'gravitational' model using a pixel's nearest four neighbours after the classification procedure. This process reduces the classification noise which might occur due to the variable range of spectral signatures of an object, and due to the occurrence of mixed pixels (mixels) at the edge of objects.

Figure 7.5 To show the nearest neighbour matrix surrounding pixel 5. The ground level dimensions for squared MSS and for TM are given (after Thomas, 1980)

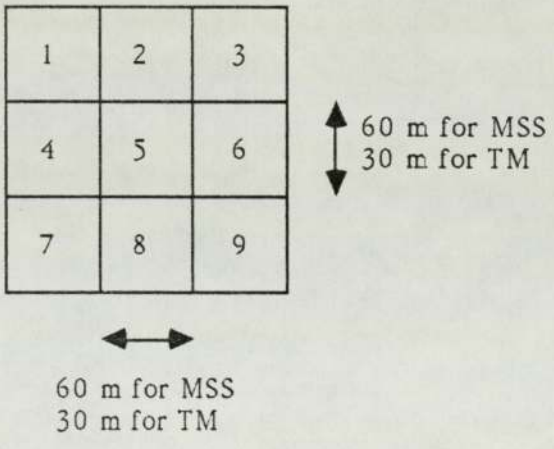

The proximity function Fj for each pixel is separately calculated by the following formula, only the non diagonal (even numbered) pixels are used.

$$Fj = \sum_{i} \frac{q_{(i)} \cdot q_{(5)}}{(d_{(i)}5)^2} \quad \text{For } i=2,4,6,8 \qquad \textit{equation 7.1}$$

where $d_{(i)}5$ is the ground distance (30 m for TM and 60 m for squared MSS data) between the centre of the ith pixel and the centre of the 5th pixel (see figure 7.5), $q_{(i)}$

and $q_{(5)}$ are weightings for the ith and 5th pixels respectively. If the ith pixel has been classified into the jth class then $q_{(i)}$ takes the value of two, otherwise it takes the value of zero. If the central pixel has been classified into the jth class, then $q_{(5)}$ (the central pixel) takes the value of two, otherwise it takes the value of one. The function is evaluated over i for each j, the results are compared. The central pixel is reclassified as a member of the class jmax corresponding to the maximum value of the proximity function. Thus the pixel is classified by a distance criterion, the model is in the form of a distance weighted inverse square law, hence the term gravitational is applied.

Tilton et al. (1982) and Swain et al. (1981) use a p dimensional context array which contains maximum likelihood probability functions of the surrounding (p-1) pixels. They derive the optimal class by finding an unbiased estimate of the context function; that is they find the maximum likelihood function not just for one pixel, but also for the surrounding pixels. Yu and Fu (1983) note that the spectral information surrounding a pixel is correlated with the central pixel being considered; this is called semi-variance (Curran, 1987). Yu and Fu use this spatial correlation to develop a recursive contextual classification. Haralick and Joo (1986) assign pixels to a class according to a large sized context array around the pixel being examined. The algorithm takes the form of a recursive neighbourhood operator involving a top down and a bottom up scan of the image. They claim that this increases classification accuracy by between three and eight percent. These are all examples of contextual rules which take effect at the time of classification.

It should be noted that there is a basic difference between statistical classifiers used prior to classification, from those used before or during the classification process. Before classification the image is represented by a statistical vector which defines some physical value of that pixel, such as its reflectance in a particular waveband. After classification the pixel is represented by a label which describes to which class a pixel has been assigned, or the likelihood of it belonging to that class. Therefore post-classification contextual analysis is a logical operation rather than a mathematical operation, whilst preclassification processing is a mathematical operation rather than a logical operation. This study has concentrated on logical operations because they are closer than are mathematical operations to the way a manual photo-interpreter uses contextual features.

7.3 Results of Contextual Analysis

In this section the results of contextual operators on the classification accuracy are given. In tables 7.1 to 7.10 the following nomenclature is used to describe the data used: FOT, first order texture measures (mean, variance and log variance). Edge, edge based texture measures (Roberts, Sobel and Prewitt). GLRLM, grey level run length based texture measures (see chapter 6 for which features were used in each test site). SGLDM, spatial grey level dependency matrix based texture measures (see chapter 6 for which features were used in each test site).

Table 7.1 contextual postclassification processing of minimum distance and decision tree analysis classifier results for Test site 1

Minimum Distance To Means									
	Median			Mode			Gravity	Edge	Minarea
	3 by 3	5 by 5	7 by 7	3 by 3	5 by 5	7 by 7			
4 bands MSS	43.56	43.67	43.53	43.32	44.76	42.01	42.76	44.84	43.53
4 bands MSS + SIR-A	44.57	44.87	47.01	45.46	48.97	51.82	42.65	48.14	45.88
4 bands MSS + 3 Edge	56.09	60.42	62.78	54.87	56.70	57.66	48.45	56.65	52.91
4 bands MSS + 3 Edge+SIR	61.38	65.44	67.44	60.82	63.94	64.80	51.06	62.41	56.75
4 bands MSS + 3 FOT	45.21	47.01	53.37	43.48	43.34	42.28	44.12	45.00	44.26
4 bands MSS + 3 FOT + SIR	48.75	48.81	50.10	47.60	46.26	45.33	48.50	48.77	48.42
4 bands MSS + 3 GLRLM	54.20	55.49	56.66	54.49	56.18	57.49	52.84	55.13	52.63
4 bands MSS +GLRLM+SIR	54.76	56.27	56.75	54.53	55.30	55.10	53.13	55.30	53.30
4 bands MSS + SGLDM	42.34	42.88	43.34	41.97	42.52	42.91	42.44	42.42	42.47
4 bands MSS +SGLDM+SIR	42.91	43.27	44.71	42.59	42.86	43.81	42.87	42.64	42.71
Decision Tree									
4 bands MSS + SIR	48.06	48.76	49.64	47.39	49.63	50.50	45.22	48.65	46.22

Table 7.2 contextual postclassification processing results of spectral shape classifier results for test site 1 using MSS, SIR-A and texture data.

Spectral Shape Classifier									
	Median			Mode			Gravity	Edge	Minarea
	3 by 3	5 by 5	7 by 7	3 by 3	5 by 5	7 by 7			
4 bands MSS + 3 Edge+SIR	39.76	39.59	39.88	41.91	41.05	40.44	39.48	42.14	42.33
4 bands MSS 3 FOT + SIR	57.92	58.90	59.10	56.31	59.01	59.36	56.42	60.34	58.59
4 bands MSS +GLRLM+SIR	40.38	40.18	40.05	40.46	39.91	39.40	39.17	42.68	41.51
4 bands MSS +SGLDM+SIR	50.48	50.45	50.23	50.38	49.81	49.39	49.02	52.13	51.28

Table 7.3 contextual postclassification processing results of maximum likelihood classifier of MSS, SIR-A and texture data for test site 1

Maximum Likelihood Classifier									
	Median			Mode			Gravity	Edge	Minarea
	3 by 3	5 by 5	7 by 7	3 by 3	5 by 5	7 by 7			
4 bands MSS	65.44	66.10	64.84	68.06	69.76	68.80	59.57	68.70	63.97
4 bands MSS + SIR-A	69.87	71.40	70.77	71.03	72.16	71.17	63.29	72.54	68.64
4 bands MSS + 3 Edge	65.34	65.92	64.41	68.03	69.71	68.68	59.50	68.53	63.86
4 bands MSS + 3 Edge+SIR	69.87	71.34	70.66	71.03	72.16	71.11	63.29	72.50	68.64
4 bands MSS + 3 FOT	66.41	68.48	67.66	68.21	70.62	69.87	59.24	69.11	64.20
4 bands MSS + 3 FOT + SIR	69.98	71.61	71.11	71.13	72.21	71.31	63.26	72.54	68.60
4 bands MSS + 3 GLRLM	59.99	60.49	58.99	62.55	64.41	63.95	54.95	62.80	59.17
4 bands MSS +GLRLM+SIR	68.39	70.52	69.81	70.19	71.27	69.84	61.61	71.85	67.58
4 bands MSS + 3 SGLDM	66.74	67.52	66.36	69.00	70.77	69.54	59.96	69.53	64.63
4 bands MSS +SGLDM+SIR	70.12	71.62	70.97	71.29	72.66	71.69	63.33	72.62	68.90

Map 7.1 Optimal product for test site 1 using maximum likelihood classified MSS and SIR-A tonal and textural data followed by a 5 by 5 mode filter

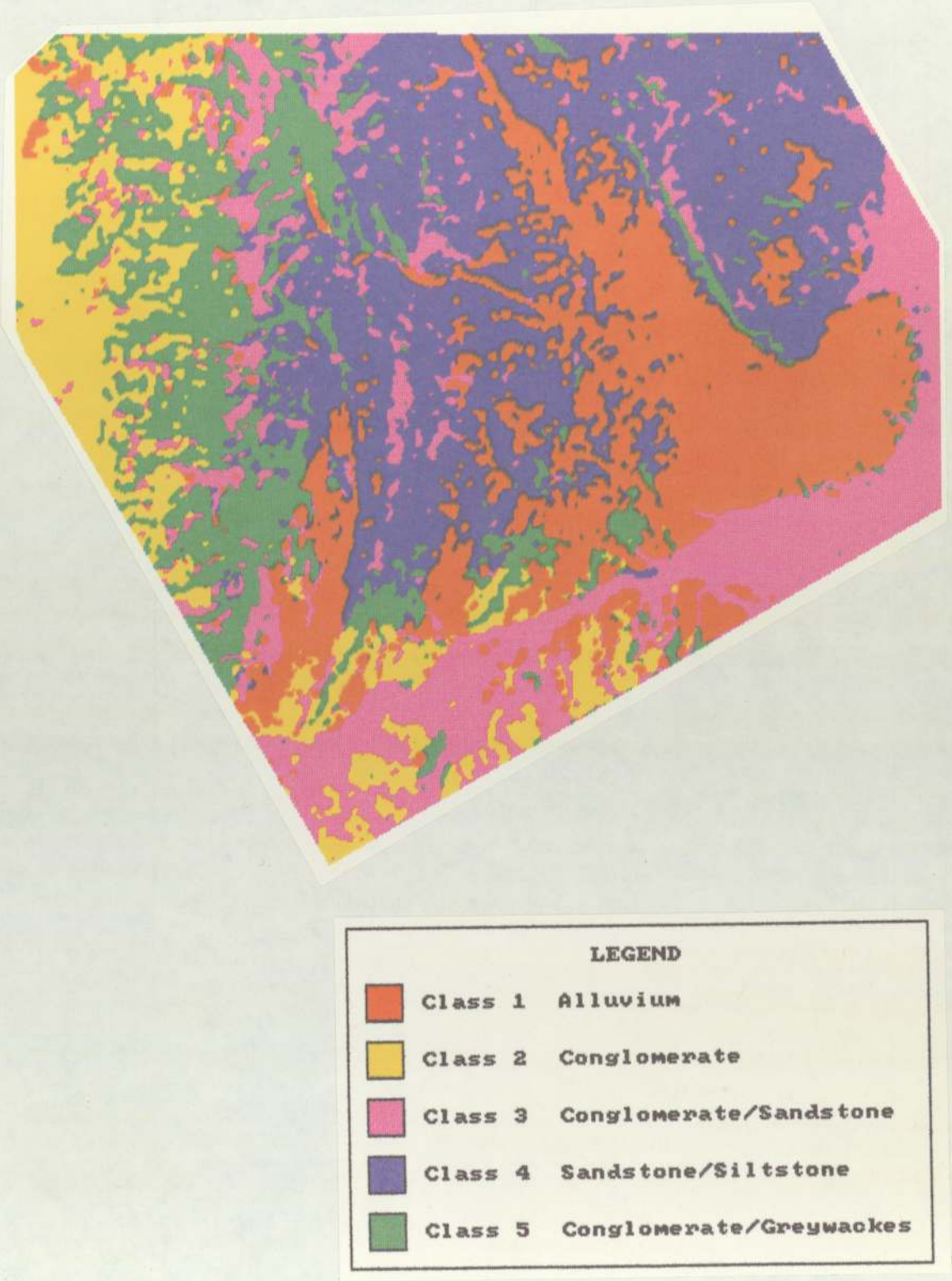

Table 7.4 contextual postclassification processing of maximum likelihood classifier results, MSS, SIR-A and texture data for test site 2.

Maximum Likelihood Classifier									
	Median			Mode			Gravity	Edge	Minarea
	3 by 3	5 by 5	7 by 7	3 by 3	5 by 5	7 by 7			
4 bands MSS	40.73	39.24	38.12	41.88	42.34	43.47	40.85	39.74	41.25
4 bands MSS + SIR-A	48.78	49.47	48.74	48.35	49.54	49.90	47.08	47.75	47.67
4 bands MSS + 3 Edge	47.29	45.65	44.61	47.30	48.58	46.26	44.78	48.31	46.88
4 bands MSS + 3 Edge+SIR	47.25	44.00	40.65	46.26	45.50	45.10	44.06	46.93	46.15
4 bands MSS + 3 FOT	41.65	42.50	43.30	40.71	39.49	38.10	42.07	40.43	41.45
4 bands MSS + 3 FOT + SIR	45.74	46.62	47.37	45.12	44.43	43.73	45.97	44.79	45.65
4 bands MSS + 3 GLRLM	41.97	41.35	41.37	42.89	43.18	43.92	42.53	41.68	42.30
4 bands MSS +GLRLM+SIR	45.86	45.24	44.88	46.30	46.88	47.58	46.08	45.78	46.27
4 bands MSS + 3 SGLDM	35.04	35.08	35.19	34.49	34.05	34.00	35.57	34.41	35.48
4 bands MSS +SGLDM+SIR	38.78	38.19	39.98	37.97	37.21	37.04	38.66	38.30	39.45
Decision Tree									
4 bands MSS + SIR	49.44	51.33	53.32	48.57	49.81	50.31	46.50	47.44	47.32

Table 7.5 contextual postclassification processing results of spectral shape classifier for test site 1 using MSS, SIR-A and texture data.

Spectral Shape Classifier									
	Median			Mode			Gravity	Edge	Minarea
	3 by 3	5 by 5	7 by 7	3 by 3	5 by 5	7 by 7			
4 bands MSS + 3 Edge+SIR	32.38	31.45	31.45	32.87	30.99	29.63	33.92	33.02	34.25
4 bands MSS 3 FOT + SIR	32.37	31.61	31.09	31.83	31.50	31.44	32.80	32.01	32.67
4 bands MSS +GLRLM+SIR	39.24	37.97	37.23	38.92	38.11	38.10	38.00	39.30	39.79
4 bands MSS +SGLDM+SIR	43.67	43.48	43.29	42.74	42.57	42.08	42.76	44.35	44.48

Table 7.6 contextual postclassification processing results of maximum likelihood classifier results MSS, SIR-A and texture data for test site 2

Maximum Likelihood Classifier									
	Median			Mode			Gravity	Edge	Minarea
	3 by 3	5 by 5	7 by 7	3 by 3	5 by 5	7 by 7			
4 bands MSS	63.66	64.36	64.90	65.80	66.81	68.59	59.90	64.99	63.02
4 bands MSS + SIR-A	72.42	72.78	72.29	73.25	74.67	75.25	67.10	74.00	71.85
4 bands MSS + 3 Edge	63.13	63.59	64.13	65.55	66.85	68.54	59.39	65.00	63.37
4 bands MSS + 3 Edge+SIR	72.20	72.69	72.38	72.63	73.99	74.37	66.73	73.86	71.86
4 bands MSS + 3 FOT	63.92	64.62	65.18	65.61	66.95	69.38	59.54	65.19	63.24
4 bands MSS + 3 FOT + SIR	72.56	73.13	72.42	73.27	74.74	75.22	67.02	74.18	71.90
4 bands MSS + 3 GLRLM	50.58	50.78	50.70	52.50	52.81	54.72	50.36	51.52	51.42
4 bands MSS +GLRLM+SIR	70.28	71.75	71.44	72.22	75.09	75.06	64.55	72.52	69.56
4 bands MSS + 3 SGLDM	63.69	64.61	65.42	65.38	66.61	68.54	59.67	65.47	63.24
4 bands MSS +SGLDM+SIR	73.39	72.97	72.36	73.21	74.64	76.51	67.08	74.08	71.94

Map 7.2 Optimal product for test site 2 using maximum likelihood classified MSS and SIR-A tonal and textural data, followed by a 7 by 7 mode filter

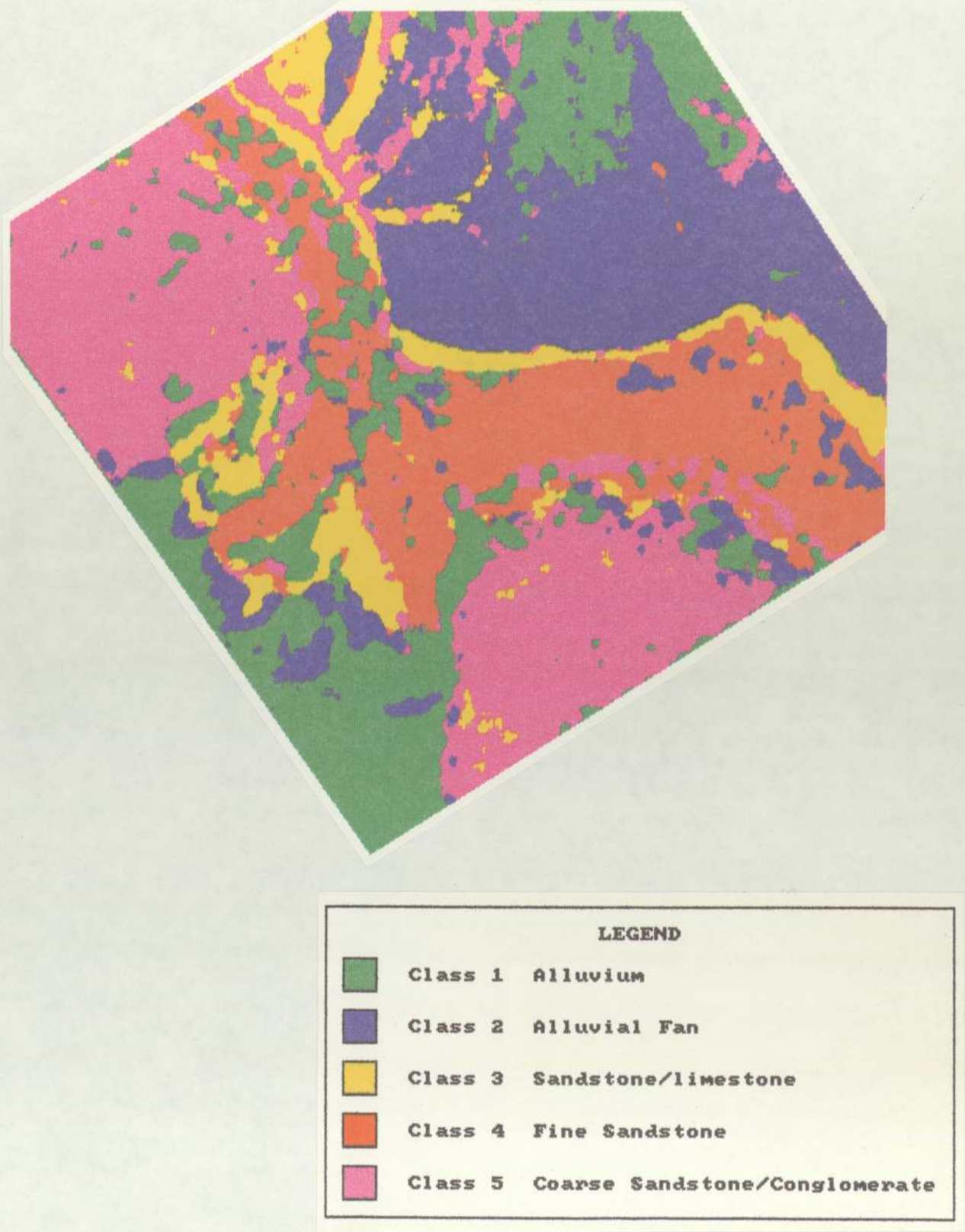

Table 7.7 contextual postclassification processing results of minimum distance to means and decision tree classifier of TM, SIR-A and texture data for test site 2

Minimum Distance To Means									
	Median			Mode			Gravity	Edge	Minarea
	3 by 3	5 by 5	7 by 7	3 by 3	5 by 5	7 by 7			
6 bands TM	48.95	49.60	50.31	52.14	54.16	56.91	48.15	52.11	50.38
6 bands TM + SIR-A	52.18	52.95	54.04	55.05	57.94	60.04	51.17	54.94	53.27
6 bands TM + 3 Edge	60.81	63.93	65.70	64.92	68.81	71.50	56.36	63.87	60.09
6 bands TM + 3 Edge+SIR	60.97	63.90	66.01	65.17	68.88	71.69	56.53	63.81	60.39
6 bands TM + 3 FOT	54.65	55.96	56.52	56.70	59.26	60.80	52.70	57.13	55.59
6 bands TM + 3 FOT + SIR	57.95	59.41	60.34	59.73	62.91	64.39	55.66	60.52	58.46
6 bands TM + 3 GLRLM	56.91	58.47	60.06	56.42	57.42	58.76	54.91	57.09	55.71
6 bands TM +GLRLM+SIR	57.08	58.44	60.30	56.52	57.47	58.93	54.99	57.22	55.80
6 bands TM + 3 SGLDM	68.01	71.08	73.16	68.35	71.71	74.12	65.14	69.09	67.12
6 bands TM +SGLDM+SIR	68.07	70.95	73.08	68.32	71.69	74.16	65.15	69.01	67.08
Decision Tree									
6 bands TM + SIR	51.76	51.44	51.10	55.36	56.15	57.20	49.08	53.36	51.32

Table 7.8 contextual post classification processing of spectral shape classifier results, using TM, SIR-A and texture data

Spectral Shape Classifier									
	Median			Mode			Gravity	Edge	Minarea
	3 by 3	5 by 5	7 by 7	3 by 3	5 by 5	7 by 7			
6 bands TM + 3 Edge+SIR	42.90	45.42	46.62	41.11	42.46	43.26	38.14	41.55	39.62
6 bands TM 3 FOT + SIR	35.86	36.54	35.91	35.71	34.90	34.04	34.95	34.37	34.70
6 bands TM +GLRLM+SIR	28.79	29.17	29.09	29.85	30.91	31.27	28.22	29.33	28.50
6 bands TM +SGLDM+SIR	50.84	52.55	53.78	50.48	51.95	52.82	49.18	50.32	49.79

Table 7.9 contextual postclassification analysis of maximum likelihood results for TM, SIR-A and texture data of test site 2

Maximum Likelihood Classifier									
	Median			Mode			Gravity	Edge	Minarea
	3 by 3	5 by 5	7 by 7	3 by 3	5 by 5	7 by 7			
6 bands TM	76.85	78.47	78.85	76.93	78.16	78.87	70.71	77.34	74.55
6 bands TM + SIR-A	77.19	78.65	80.29	77.29	78.27	79.06	73.01	77.49	75.38
6 bands TM + 3 Edge	78.70	80.27	81.19	78.77	79.90	80.54	75.14	79.56	77.17
6 bands TM + 3 Edge+SIR	78.88	80.00	80.72	78.88	79.72	80.14	76.02	81.17	77.75
6 bands TM + 3 GLRLM	74.60	76.39	77.57	74.89	76.12	76.99	70.20	75.18	72.62
6 bands TM +GLRLM+SIR	74.42	76.28	77.27	74.57	76.53	77.05	70.36	75.16	72.90
6 bands TM + 3 SGLDM	79.87	80.52	81.32	79.87	80.36	80.43	77.73	80.23	79.00
6 bands TM +SGLDM+SIR	80.11	80.69	81.42	80.52	80.34	80.29	77.77	80.36	79.19

Map 7.3 Optimal product for test site 2 using maximum likelihood classified TM and SIR-A data tonal and textural measures, followed by a 7 by 7 median filter

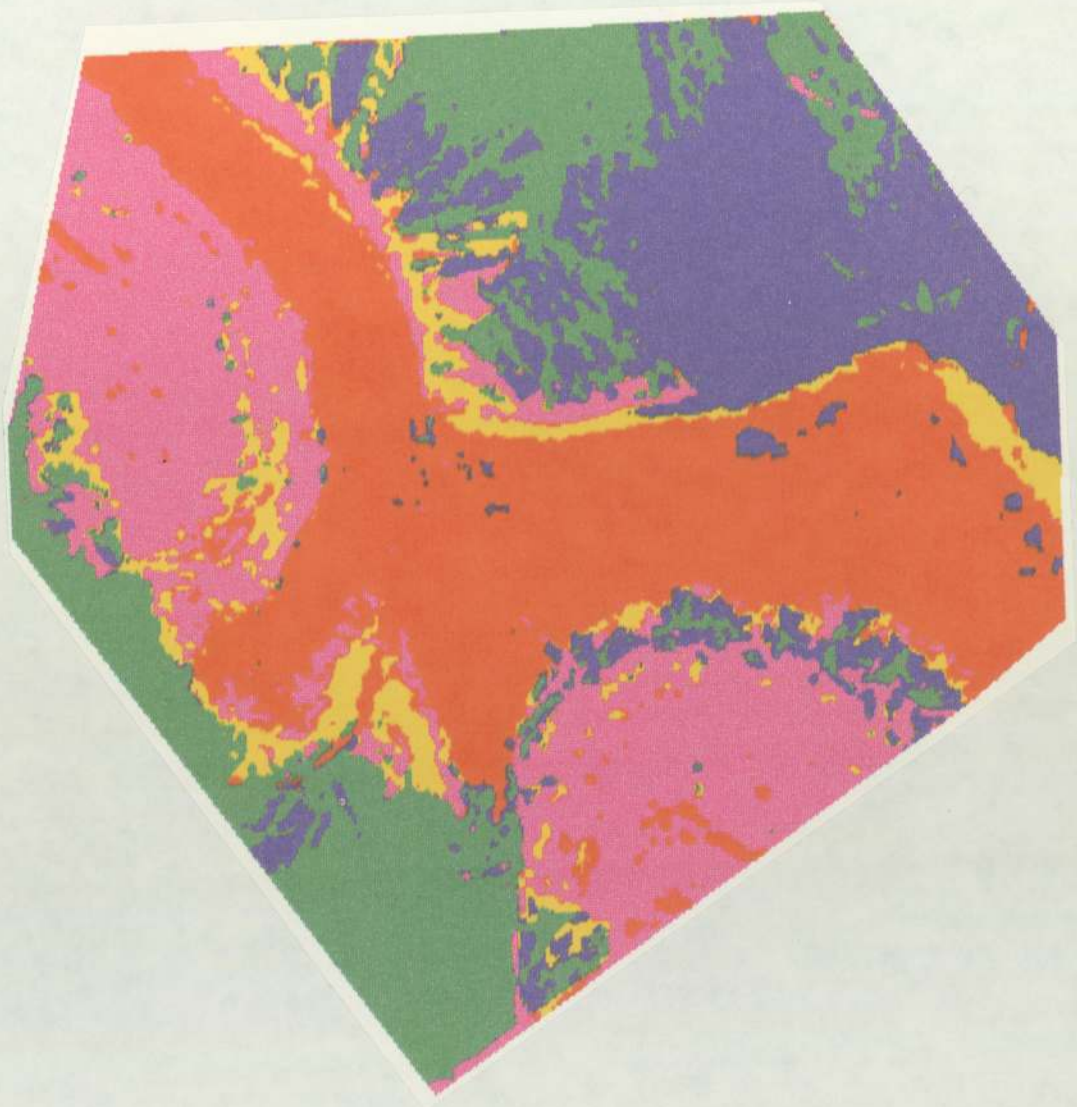

LEGEND

Class 1 Alluvium

Class 2 Alluvial Fan

Class 3 Sandstone/limestone

Class 4 Fine Sandstone

Class 5 Coarse Sandstone/Conglomerate

Table 7.10 contextual analysis of Swain and Tilton maximum likelihood classification

Contextual Maximum Likelihood									
	Median			Mode			Gravity	Edge	Minarea
	3 by 3	5 by 5	7 by 7	3 by 3	5 by 5	7 by 7			
Test Site 1									
4 bands MSS	74.98	76.03	76.31	74.14	74.37	73.97	72.54	75.18	74.02
4 bands MSS + SIR-A	78.93	80.31	80.57	77.88	78.53	77.46	76.47	79.09	78.08
Test Site 2									
4 bands MSS	67.23	67.95	68.36	67.72	68.54	69.29	67.27	68.49	67.43
4 Bands MSS + SIR-A	73.80	74.28	74.54	74.23	73.78	74.05	73.58	75.02	74.38
6 bands TM	77.89	78.60	79.36	77.77	78.38	78.85	77.39	78.29	77.53
6 bands TM + SIR-A	78.16	78.91	79.56	77.98	78.39	78.82	77.59	78.45	77.68

The following points can be noted from tables 7.1 to 7.9, using contextual spatial post processing techniques. In nearly all cases, the use of such techniques increases the classification accuracy; the exception being cases where the initial accuracy is very low (for example some of the spectral shape classifier results, tables 7.2 and 7.5). The best contextual operators appear to be the simplest, such as the median or mode filter. Increases in the accuracy for the 7 by 7 median or mode filter are as high as 8%, and average in the region of 5%. Increases in the accuracy of the edge replacement and minimal area replacement are as high as 6%, and average about 4%. The gravity filter produces increases in the region of 1 to 2%. The larger the size of the window used for these operators, generally the greater the increase in accuracy. For example the 5 by 5 filter increases accuracy by about 2% more than a 3 by 3, and the 7 by 7 filter increases the accuracy by about 1% more than a 5 by 5 window. The larger increase in accuracy given by the larger kernel windows appears to be because larger windows produce more smoothing than smaller windows and greater reduction of isolated 'out of context' areas.

The gravitational filter described by Thomas (1980) performs poorly when compared with other contextual features, it would appear that more work needs to be carried out on the use of appropriate thresholds for this operator.

The minimal area replacement method of Letts (1979) and the boundary replacement methods work reasonably well, with the boundary replacement method consistently out performing the minimal area replacement method. The reason for this method working well are probably two fold: firstly isolated pixels which probably represent some form of noise in the data are declassified. Secondly, boundary pixels which usually consist of pixels from two or more classes, that is they are mixed pixels (or mixels) and are declassified. Therefore, the likelihood of these pixels being assigned the true class according to per pixel features is relatively small. All post classification contextual features (especially the boundary replacement method) use information from the local neighbourhood to increase the likelihood of these mixels being placed in their correct class.

The best results obtained for the contextual operators used in this research for LANDSAT MSS and TM in each of the two test sites is given in maps 7.1, 7.2 and 7.3. These show that for each study area that the classified output has a much smoother appearance than either of the classifications shown in chapters 5 and 6 for the corresponding test site. As expected isolated pixels have been removed and the output generally appears much more like the lithological maps given in the lithological maps 3.1 and 3.2.

The contextual algorithm suggested by Swain (1979) differs from the other contextual features tested here (see table 7.10), in that it takes place at the classification stage not after classification. It is therefore possible to carry out further contextual postclassification processing. The results for this operator work well compared with all the other contextual features tested. In the case of test site 1, this contextual feature using LANDSAT MSS and SIR-A data followed by median filtering, produces the highest accuracy of any band combination for this test site.

A note of caution should be sounded here, as the increase in accuracy noted may be more apparent than real. The verification areas used to test the accuracy of the classifications utilised large areas which were all of one class. Clearly any technique which removes isolated pixels from such areas will increase the accuracy whether the removal is justified or not. A case in point are the pixels which are classified as alluvium in test site 2 in the south of the image (see plates 6.3 and 7.3). This alluvium

is not shown on the geological map, and its removal or reduction by contextual postclassification techniques would no doubt increase the classification accuracy. However, there is good reason to believe that alluvial cover is present in this area as a large river system (which is shown on the map) passes through the exact spot where the alluvial cover is shown on the output classified image.

7.4 Summary

Simple contextual techniques have been described. These simple techniques emulate some of the contextual features used by the manual interpreter of imagery in that they remove pixels which are out of context with their surroundings. The contextual operators achieve this by taking account of the size, and position of pixels of a certain class in the image. This not only gives rise to higher classification accuracies, it also improves the overall visual appearance of the output classified image.

Slightly more complex contextual features which measure the shape of certain classes (for example alluvial fans have characteristic shapes) have not been evaluated. This is because only non stereoscopic data was available, therefore the true shape could not be measured and also because the shape of an object is dependent on the its boundary pixels, these pixels are the ones that have the lowest likelihood of being correctly classified. Therefore boundary shape properties are not useful. Properties that measure fuzzy attributes of the overall shape may be useful, especially using stereoscopic data where the true shape of an object can be measured.

Chapter 8
Identification of Lithology

8.0 Introduction

A primary objective of image processing is to discriminate objects within scenes and thereby identify them. Accordingly, an image must first be segmented into regions that correspond to objects in the scene, and then the objects must be identified. Two levels are thus apparent, the low level processing stage mainly concerned with segmentation, which has been discussed in the first part of this work. Secondly, there is a high level stage devoted to the interpretation of the scene. Clearly, the second part of this process is more likely to be successful if the first part of the process is successful. This is why the most accurate classification of the image was so thoroughly investigated in the first part of this work. In this chapter a method is outlined in which tentative names can be given to the lithologies discriminated in the previous chapters. This is precisely the way that manual interpretation of imagery is carried out by an expert photo-interpreter.

8.1 Knowledge Based Systems

High level image interpretation or computer vision techniques are part of the field of Artificial Intelligence (AI). The knowledge from a number disciplines can be represented by a set of rules; these are called production rules (Nazif and Levine, 1985). Production rules can then be used to build Expert Systems, the rules are expressed in the form of "**IF** 'X' is true, **AND** 'Y' is true, **THEN** 'Z' is true. For example, **IF** the rock is sedimentary **AND** its predominant mineral is calcite, **THEN** the rock is limestone. In this example the rules are formed by the 'if then' statement and the goal (the lithology) is found as a consequence of the rule. Rules of this sort have the major advantage over other forms of knowledge representation in that they are modular entities which can be altered without affecting the structure of the system. Therefore the rules can be increased incrementally as our knowledge about an object increases, without a major restructuring of the knowledge base.

According to Basden (1984) the advantages of an Expert System are threefold. Firstly, they have a flexible expression, that is they are able to incorporate 'rules of thumb' that experts tend to use, as well as more formal expertise. Secondly, they use human-like processing, that is they operate at a level, and in terms and concepts that a user can feel affinity with, they can therefore be easily understand by experts who are not computer literate. Finally, Expert Systems can handle uncertainty and even

contradictory evidence in a human-like way. The benefits of automatic interpretation are two fold. Firstly, consistency; machine processing means that an the interpretation will not be subject to the variations which are caused by dufferent interpreters. Secondly, knowledge can be incorporated from a wide range of experts so that multiple interpretation of the imagery is possible. This is extremely valuable, because as was stated in chapter 1 the rate of data production now far outstrips the possibility of human interpretation.

Previous work by Tailor et al. (1986) describe the design of a knowledge based system for understanding remotely sensed images. Kanal et al. (1983) also describe the design of an expert system for remotely sensed imagery, they pay particular attention to the extraction of cartographic features from the data. They discuss the types of knowledge that must be modelled in remote sensing, such as the external factors which produce the structure seen in the imagery. They also discuss multisensor registration and the resolution of conflicting evidence. Goldberg et al. (1983) uses a production rule based expert system for the analysis of multitemporal LANDSAT imagery to analyse a forested region in Newfoundland, Canada. They show the value of this system as the system was able to identify both highly discernible, and more subtle forest changes. These results were verified correct by ground data. Erickson and Likens (1984) describe an expert system capable of producing a preliminary land cover classification from an unsupervised classification of LANDSAT MSS and other ancillary data, such as topographic data. Venable et al. (1985) use a rule based system to improve an image segmentation by segmented region merging. Perkins et al., (1985) uses the Lockhead Expert System (LES) to interpret digitised aerial photography. It makes use of multiple goals and multiple rule sets to determine the best label for each region. They make use of contextual knowledge of the type 'cars are likely to be found adjacent to roads', they find that this significantly improves the classification accuracy.

8.2 Recognition Of Lithological Materials

In this study the rules that an expert geological photo-interpreter would use to identify lithologies are described. Some points about the identification of lithology in remote sensing images must be borne in mind. Just as the field geologist, who bases his subdivisions of lithology on hand specimens, uses more generalised rock divisions than a petrographer using microscopic examination of the rocks. So the photogeologist or remote sensing expert must use more generalised units than the field geologist. The detail and the lithologies that can be mapped from satellite data are therefore reconnaissance divisions only.

According to Allum (1966) the following general data must be recorded prior to detailed analysis of the lithology.

1) The recognition of the climatic environment (for example, very active, active, inactive).

2) The recognition of areas of outcrop.

3) The type and amount of vegetation cover.

3) The recognition of areas of superficial deposits.

5) The recognition of the strike of the outcrop.

6) The study of lineaments transverse to outcrop, to see if they are faults, dykes, joints or combinations of these.

For a particular rock, some or all of the following data must be recorded.

1) The image tone of the rock relative to the adjacent rocks.

2) The resistance to erosion of the rock body relative to adjacent units.

3) The boundary of the rock body.

4) The topographical expression of the whole rock body.

5) The joint pattern (if any).

6) The fault pattern (if any).

7) The drainage pattern.

8) The bedding or the relic bedding lineaments.

9) The foliation lineaments.

10) The regional geological environment.

8.2.1 Recognition of Sedimentary Rocks in Imagery

In this study because of their predominance, work concentrated on the recognition of sedimentary rock types. As was shown in chapter 3, the physiography and hence the photomorphic character of each test site was heavily influenced by the lithology. According to Lillesand and Kiefer (1987) the main attributes that distinguish sedimentary rocks are there bedding, jointing and resistance to erosion, these all produce diagnostic textural attributes.

Generally sediments are recognised by their layered appearance, this can frequently be observed even in LANDSAT MSS data. This layering is represented by variation in both the relief and tone of the lithology. In most cases it is possible to differentiate between metamorphosed and unmetamorphosed sediments. One of the results of metamorphism is to make the individual beds of a sequence more nearly equal in their

resistance to erosion. Sandstone has prominent bedding especially when interbedded with shale. In arid areas there is seldom residual soil cover because the sand which would form such a soil is removed by wind erosion. In humid areas residual soil cover of one to two metres on sandstones are common, depending on the grain size of the sandstone. Horizontally bedded sandstone forms bold massive topography, flat topped hills, steep hillsides and coarse drainage systems with V- shaped gullies. The rock is normally medium to light toned, and is sometimes reddish. A dense tree cover over sandstone in humid areas is common.

Shale does not have bedding visible on either satellite imagery or small scale aerial photography. The resistance to erosion is low and, shale is relatively impermeable, so most groundwater runs of the surface causing extensive erosion and a very fine drainage pattern. Residual soils are normally less than one metre thick and are high in silt and clay content so are therefore fine grained and homogeneous in texture. In arid climates minutely dissected terrains with steep sided narrow gullies are common. In humid climates hills are gently sloping, softly rounded. Dendritic drainage is common and the overall effect is a characteristic very fine texture.

Limestone in arid climates has a mottled light tone often with some reddening. Few surface streams occur because of its permeability, giving the rock a very coarse, smooth texture. In humid climates numerous roughly circular sink holes occur with centripetal drainage which give the outcrop a mottled appearance.

8.2.2 Recognition of Superficial Deposits in Imagery

For photogeological purposes superficial cover is conventionally classified as either residual or transported (Allum, 1966). Transported superficial cover is recognised by its almost total blanketing effect on the underlying geology. Its association of the cover with its means of transport, its association with diagnostic landforms (such as scree slopes, sand dunes or meander belts). Finally, transported superficial cover is recognised by well defined, sharp boundaries. Residual cover on the other hand, (which includes laterites, bauxites and soil) does not completely blanket the geology, because it is formed by the in situ weathering of the underlying rocks. No means of transport for the cover type can be recognised. Residual cover has gradational boundaries with the underlying lithology. On satellite imagery it is virtually impossible to delineate residual cover accurately, therefore little effort was expended in recognising this class.

Sand dunes have excellent internal drainage, and are frequently being eroded by wind action and therefore do not support much vegetative cover. Loess forms generally an undulating surface with roughly parallel crests, very often dissected by many streams and gullies, giving a very fine textured appearance.

Fluvial deposits such as alluvial fans occur adjacent to steep slopes where streams discharge into areas of subdued relief. Fans (which are funnel or fan shaped) generally have coarsest material at their apex and finest material at their base, texture is generally fine grained except where the drainage is prominent. Flood plains are relatively flat and level with small downstream slope. Complex patterns of tone are present reflecting the variety of soil and moisture conditions which can exist. In arid areas flood plains are often stained white by the presence of precipitated water soluble salts carried by the river.

8.3 Design of a Knowledge Based System

The first stage in the production of a knowledge based system is to decide on which attributes are used in the manual interpretation of the lithology from satellite imagery. Once these attributes have been decided upon some form of measuring these attributes should be found. Once the attributes have been measured the system should convert these measures into some form which would be recognisable to a manual interpreter. For example a lithology might have an average reflectance in all bands of 65, but this conveys little information to the observer. However, if the average reflectance were described as being dark, or light then this would convey meaning. The problem arises here that many attributes are measured on a relative scale not an absolute one. For example, a sandstone outcrop is normally said to be light toned, but in a scene dominated by dark toned basalts it would be described by manual interpreters as being light toned. Such 'fuzziness' in an attribute can be modelled in a knowledge based system by allowing margins for error in the assignment of an attribute to an object.

Using two dimensional satellite imagery, it was decided to measure the following three attributes which are used by manual interpreters to identify lithology: 1) average tone; 2) texture roughness; and 3) texture coarseness. An experiment was carried out to determine whether these attributes could be used with simple production rules to identify the sedimentary lithologies used in each of the two test sites. For the sake of being able to compare results directly the experiment concentrated on the LANDSAT MSS imagery.

The overall tone of each lithology was calculated by simply adding the brightness value of each pixel in bands 4, 5 and 7 (the bands used to produce a standard false colour composite), belonging to each class and dividing this by the number of pixels in that class. A classified image was used to give the distribution of each class type, in each case the maximum likelihood classifier image, with the highest accuracy following contextual processing was used. In test site 1 the image used was the Swain and Tilton (1981) maximum likelihood classification, followed by 7 by 7 median filter; and in test site 2 the image used was the maximum likelihood classifier using four bands of MSS and three SGLDM texture measures, followed by a 7 by 7 mode filter.

To test the texture of each class, SGLDM based measures were chosen because, though these measures were not successful for increasing the classification accuracy, they probably provide better information over the much larger areas covered by each lithology, rather than the small 8 by 8 blocks used in the classifiers. Two texture features were selected, firstly the angular second moment (ASM) (to measure texture coarseness) and secondly entropy (to measure texture roughness). It was shown in an earlier experiment, that the ASM was the most consistently used texture feature employed to measure texture coarseness, while measures based on entropy were chosen in each case to measure texture roughness.

Using test site 1 to train the system the boundaries given in table 8.1 were chosen to define different states of tone and texture.

Table 8.1 Results of tone and texture coarseness boundaries decided upon by using test site as a control area.

Tone		Coarseness		Roughness	
55 -	Very Dark	55 -	Very Coarse	45 -	Very Smooth
55- 60	Dark	55- 60	Coarse	46- 50	Smooth
61- 65	Medium	61- 65	Medium	51- 55	Medium
65- 70	Light	66- 70	Fine	56- 60	Rough
70 +	Very Light	70 +	Very Fine	60 +	Very Rough

Having decided upon these somewhat arbitrary boundaries, the expected attributes of a wide variety of rock types were programmed. The look up table (LUT) of lithologies used to identify objects in the imagery are given in table 8.2. The attributes are based on those given by Allum (1966) and Lillesand and Kiefer (1987).

Table 8.2 Look Up Table of Lithology Used to Identify Objects Discriminated in this Study.

Tone	Coarseness	Roughness	Lithology
Medium/ Light	Very coarse	Very rough	conglomerate
Medium/ Light	Very coarse	Rough	conglomerate/ sandstone
Medium/ Light	Very coarse	Medium	sandstone/ conglomerate
Medium/ Light	Coarse	Rough	coarse sandstone
Medium/ Light	Coarse	Smooth	limestone
Dark	Medium	Rough	shale
Medium	Medium	Medium	sandstone
Medium	Fine	Rough	Alluvial fan
Medium	Fine	Smooth	Alluvium
Dark	Fine	Medium	Siltstone/ sandstone

Table 8.3 Results of Lithological Identification of Test Site 1

	True Class	Classified As
Class 1	Alluvium	Alluvium
Class 2	Conglomerate	Conglomerate
Class 3	Conglomerate and Sandstone	Alluvium
Class 4	Silstones, Fine Sandstones	Coarse Sandstones
Class 5	Conglomerates	Conglomerate

Table 8.4 Results of Lithological Identification of Test Site 2

	True Class	Classified As
Class 1	Alluvium	Alluvium
Class 2	Alluvial Fan	Conglomerate
Class 3	Fine Sandstone	Coarse Sandstone
Class 4	Fine Sandstones	Coarse Sandstones
Class 5	Coarse Sandstones	Coarse Sandstones

The results show that in this simple example the production rules were capable of assigning the correct classes to three out of five lithologies in each test site. These results are moderately encouraging, as the misclassifications are not very different from the true classes. However, it should be remembered that the lithologies are described at only the reconnaissance level. No detail is given about the composition and distribution of the variation of rock types in each class. Furthermore, in each example only a fairly limited number sedimentary and superficial of rock types were present, therefore the knowledge represented in the system is rather limited, the overall model of lithologies was relatively simple. The system needs testing in a much more complexly structured area, and with a much greater number of lithologies, before any strong conclusions can be drawn as to the merit of this type of system. The rules could be made more complex by adding weightings to each attribute depending on its importance. For example a certain spectral signature such as limonite will identify it in MSS data. Therefore such a spectral signature could be used to identify limonite without any other attributes being measured.

A manual interpreter would normally use stereoscopic data to identify bedding dip and amount, as well as a variety of other structural details. Without stereoscopic data, only a limited success could be achieved in identifying lithology.

8.4 Summary

It has been shown that simple production rules can be used to store the knowledge used by an expert photo-interpreter. Production rules are relatively simple to program, but somewhat arbitrary values must be assigned to attributes measured from the image; such as texture coarseness, and roughness. In this very simple example, using sedimentary and superficial cover types, a limited amount of success was achieved in assigning lithology names to classes in the imagery. The results are by no means conclusive, and much work must be done with other examples before a working system can be designed. However, these initial results are moderately encouraging. The limitations of this knowledge base are firstly, on the lack of generality of the attributes used, a coarse texture in this image might be a fine grained texture in an adjacent scene. Secondly the system has not been tested in a sufficient number of cases to produce confidence limits on the ability to consistently recognise lithology.

Chapter Nine
Discussion

This study has aimed to use remotely sensed data to map lithology of a semi arid region of northwest Argentina. Satellite remote sensing data from three different sources was available for this study: these were LANDSAT MSS, TM and SIR-A imagery. The methodology applied was to simulate as far as possible by use of computer, the methods employed by a geologist manually interpreting satellite imagery with the aim of producing a lithological map. The photogeologist uses three different attributes to map lithology, these are: firstly tonal features (that is colour), these give compositional about the lithology. Secondly he uses textural features (spatial variation), these give information about the jointing and bedding (if any) of the lithology and its relative resistance to erosion. Finally he uses contextual features (the size, shape and position of objects) to eliminate unlikely occurrences of a lithology. Work has involved modelling these three attributes to produce optimal classification products.

Geological maps contain a wealth of structural features, (such as faults, dip and direction of dip of bedding) and chronological information, this is in addition to lithological detail which they provide. The photogeologist is in favourable circumstances, capable of producing reconnaissance geological maps containing some or all of this structural detail (only relative chronological information can be obtained from remote sensing data). Structural details, however, can only be produced from stereoscopic data, and therefore LANDSAT or SIR-A imagery can not be used to produce 'true' geological maps (LANDSAT can produce some stereoscopic data in the overlapping part of adjacent images, but this area is small, and the vertical exaggeration is relatively weak). Therefore this work has concentrated on the production of a lithological map from these data.

The SPOT satellite is capable of generating three dimensional images at nearly all latitudes. Therefore with SPOT data it will be possible to map structural features and thereby produce a 'true' geological map. Stereoscopic data allows the production of topographic information, and the addition of this is likely to increase the classification accuracy. Many geological phenomenon produce their own characteristic topographical features, for example fault guided valleys, or ridges caused by dykes. Topographic data is very likely to be useful for delineating such features and is therefore one step toward the production of more accurate lithological maps, and possibly 'true' geological maps.

It was shown in the first part of this work, that the positioning of the spectral bands of the sensors on LANDSAT MSS are comparatively poor for the discrimination and identification of geological materials. This is because the bands for LANDSAT MSS were chosen for the maximum differentiation of vegetation, not geological materials (Henderson and Swann, 1976). Limonite is the only commonly occurring mineral which can be uniquely identified in LANDSAT MSS data, because of an iron absorption band which occurs in the near infra red. It was also noted that the middle infra red is a promising area of the electromagnetic spectrum for the discrimination of certain types of lithological material, because of an absorption feature caused by Al-OH and Mg-OH bond bending and stretching vibrations for layered silicates. Therefore, the presence or absence of clay minerals can be determined in this part of the electromagnetic spectrum (Siegrist and Schnetzler, 1980 and Rothery, 1985). The LANDSAT TM sensor which has spectral bands in the middle infra red would be expected to better discriminate lithology. It is interesting to note that the band 7 of TM which covers the middle infra red region was placed on the TM sensor at a very late stage on the insistence of GEOSAT (a committee of geological remote sensing experts). The superior positioning of spectral bands for the TM sensor was shown in this study: the coincident spectral plots for test site 2 (figures 5.4 to 5.7) show that the LANDSAT MSS could only poorly differentiate between the lithologies present while, bands 5 and 7 of the TM sensor (the middle infra red bands) provided much better separation of classes.

It was further noted that the thermal infra red may potentially be the most exciting region of the spectrum for geological remote sensing. Silicate minerals have distinctive absorption features in this part of the spectrum (restrahlen bands), and these bands occur in different positions for different silicates, depending on the bonding of the silicate lattice. The potential exists for sensors such as TIMS (a multiband thermal sensor), for example where the rock surface is well exposed, (such as in desert environments) to identify bulk silicate compositions of many lithological materials. Silicate materials are particularly important, because it is estimated that over 90% of all crustal materials are composed of silicates. However, there are complications, as even small amounts of vegetation and other surface materials can cause anomalous spectral responses. Some work is currently being carried out on the use of so called 'agent orange algorithms' or software defoliants (Fraser and Green, 1987). The idea behind these algorithms is the removal of vegetation effects from the data in order to better delineate the position of rock outcrops. It may be possible that such algorithms coupled with data collected in the middle and thermal infra red will for the first time make it

possible to discriminate, and also possibly even identify, the composition of most geological materials.

Mineral composition is only a part of lithological identification, for example a granite and a sandstone can have fairly similar mineral compositions:- quartz, feldspar and a mafic (commonly a mica), but they are clearly very different lithologies. Radar data provides important lithological information which is complementary to the compositional information conveyed by passive sensors (such as LANDSAT MSS or TM). Radar gives information about the physical properties of a lithology such as its surface roughness, subsurface roughness and its complex dielectric constant. Radar data are to a large extent dominated by the attitude and orientation of topographic slope to the antenna, therefore it is useful to pick out structural details such as faulting, jointing and bedding. It is also useful for discriminating between wet and dry materials because of its dependence on the complex dielectric constant, which to a first order approximation is dominated by the water content. Therefore radar may be useful for discriminating a well drained lithology such as limestone from a poorly drained lithology such as a limy mudstone. As radar is dependent on subsurface roughness, it can in certain favourable circumstances (arid conditions), penetrate the surface and therefore reveal lithological information about shallowly covered classes. This is particularly useful for penetrating the sort of thin veneers, such as desert varnish, which can obscure rock outcrops in LANDSAT images of arid environments. Finally radar is very useful for differentiating the grain size of sediments, especially when the incidence angle of the radar is high, as is the case with the SIR-A data used in this study (Stone and McBean, 1987). At high incidence angles the topography has a much smaller influence on the returning beam, therefore surface and subsurface roughness (which are related to the grain size) more strongly influence the radar return.

Blom and Daily (1982) carried out experiments to combine the complementary aspects of radar and passive multispectral data. They used coregistered LANDSAT MSS and SEASAT data, the radar data modulating the brightness of the image at every point. They claim this significantly improves the visual appearance of the imagery. Experiments using a similar, coregistered MSS and SIR-A data set in this study showed a similar visual improvement, mainly caused by the increased texture in previously homogeneous regions, and strong radar shadow giving a pseudo three dimensional effect. However, it was found that this increased texture gave rise to greater within-class variation, which in turn led to lower classification accuracy for supervised classification techniques.

The SIR-A data used in this study was successfully co-registered to the LANDSAT MSS data with a first order least squares to polynomials fit, having under 10 control points. This model seems justified because of the small coefficients of xy: of the order of 10^{-5} or smaller. Nearest neighbour resampling was used, this has the advantages of being computationally efficient and preserving the radiometric characteristics of the data. This is important in the case of radar, with its strong speckle, because other resampling methods would produce excessive blurring of the data. Principal components analysis of the coregistered LANDSAT and radar data sets showed the radar to be uncorrelated with either the MSS or TM data. The first principal component of the combined data set was found to be dominated by the red and near infra red bands, it is believed that this is due to the presence of ferrous minerals such as limonite and haematite. The second component was dominated by the radar data.

Radar data sets will become routinely available during the 1990's with the launch of ERS-1 and RADARSAT, it will be interesting to investigate the potential of multi-polarisation, multi-look angle and multitemporal radar data sets for geological mapping. Much work remains to carried out on the processing of radar data for geological mapping.

Topographic data need not be produced by a remote sensing device, it can be input from contoured maps and interpolated onto a regular grid to form a ancillary data set, and if topographic data is available then in most cases it should be used. This brings in the whole area of geographical information systems (GIS), which store spatially related data sets from a large number of sources. The sources of available data for a geological GIS include: multisensor imagery, magnetic data, gravity data, geochemical data, seismic profiles, airborne geophysical data and borehole records. The data are stored in a relational database which can be interrogated to show for example, the most likely site for the occurrence of a certain mineral deposit or the optimal positioning of an oil well. GIS are very powerful tools for exploration work, clearly with all the available data the number of combinations becomes impractical for efficient manual interpretation. The GIS therefore offers the potential for storing and interrogating data both efficiently and quickly. Remotely sensed data are among the most important data input to GIS .

The primary means of semi-automatically producing a lithological map from digital remote sensing data is to use supervised classification techniques. Using a variety of these techniques it was found that the classification accuracy for LANDSAT MSS data was unacceptably low. The addition of SIR-A data significantly improved this classification accuracy - by nearly 10 % in some cases. The results for the TM data

showed significant increases in the classification accuracy over both the MSS and the combined MSS and SIR-A data sets, the addition of SIR-A data made comparatively little difference to the accuracy of the TM. The improvement of the TM over the MSS was as expected, as was shown the TM showed much better discrimination of lithology than either the MSS or the SIR-A, especially in its middle infra red bands.

It was found that the maximum likelihood classifier produced results 10 to 15% higher than either the decision tree classifier or the minimum distance to means classifiers. In the case of the decision tree classifier the separability of classes was so poor that multiple AND's were used to define class decision boundaries. Classification accuracies for the LANDSAT MSS combined with SIR-A data were found to be in close agreement with those reported in the literature, that is in the range of 40 to 60% (Siegal and Abrams, 1976 and Short, 1984). Accuracies for TM data were in the range of 50 to 70%, these accuracies are still unacceptably low except for the crudest reconnaissance purposes.

The spectral shape classifier is a new type of classifier first described as an unsupervised technique by Pendock (1987). The classifier can be used as a supervised classifier by building histograms of the spectral shapes for each of the training areas. Each pixel is placed in the class which its spectral shape most closely resembles. One of the advantages of the spectral shape classifier is that it is numerically simple. Results show that generally the classifier produced disappointing classification accuracies, normally being able to distinguish only two or three classes. However, the results for TM data with added SGLDM texture bands did produce an acceptable result. Therefore, it is probable that if data were obtained that better discriminates the lithologies in the scene, then the spectral shape classifier would be able to perform at least as well as other forms of supervised classifiers. The spectral shape classifier may become of increasing interest because of its computational simplicity, as more highly dimensioned remote sensing data sets become available in the next few years.

Textural features are very important in the photogeological interpretation of images, especially when spectral features are insufficient to discriminate lithology. The jointing and or bedding relationship allied to the resistance to erosion of the lithology gives rise to its texture. For example, as has been stated, granite and sandstone can have almost identical bulk mineral compositions and therefore may have very similar spectral characteristics. However, granite is characterised by a well developed irregular joint set, while sandstone is characterised by strong, regular bedding and jointing, each gives rise to a characteristic texture. Therefore, experiments were carried out in this

study using textural analysis techniques to increase the classification accuracy achieved with supervised algorithms.

A review of literature showed that second order texture measures were both theoretically and empirically more powerful than first order measures, because they take account of the change of texture within a texel. Two important textural properties of texture can be recognised. These are: firstly, coarseness (related to the spatial frequency), which is a measure of the overall size of the texel. And secondly, roughness (related to the spatial amplitude), which is the a measure of the internal variability of the grey tones that make up the texel. Second order measures can potentially measure both texture coarseness and roughness, whereas first order measures can only measure texture roughness. A third attribute of texture is directionality, few measures have been described that can measure this property. It would seem desirable that a texture measure be developed that can measure this attribute as many geological phenomena, such as bedding, drainage patterns, dyke swarms, faulting, and folding all produce directional textures.

With TM data the addition of texture bands did significantly increase the classification accuracy, and the second order texture measures were found to be superior to first order measures, with the SGLDM measures producing the best results. However, in the case of LANDSAT MSS data the classification accuracy was not improved significantly by the addition of texture data. Furthermore, the second order measures performed less well than simple first order texture measures. The difference between the results for the MSS and the TM appears to be due to two factors. Firstly the texture measures for the TM were carried out on a middle infra red band which showed good discrimination of lithology, while for the MSS texture features were generated from a near infra red band which showed less spectral discrimination of lithology. Therefore, it would be expected that textural features would be better shown by the TM than the MSS. Secondly and possibly more importantly, the spatial resolution of the TM is more than twice as great as the MSS data. The texture of a rock surface is determined by the topography of the surface, which is in turn related to the lithology. If the topography of an area varies on a smaller scale than the spatial resolution of the imagery then the data will be unable to discern the texture of the lithologies. It is probable that the resolution of LANDSAT MSS is too low to measure the distinctive textures of the lithologies in the two test sites and therefore was unable to significantly improve the overall classification accuracy.

Contextual rules, those which use the spatial relationships of a pixel or an object, and which are extensively used by manual interpreters in classification, were investigated in this study. Three different types of contextual operator can be used: those that work prior to classification, those that work at the time of classification, and those that work after an initial classification. Preclassification contextual rules are essentially mathematical processing techniques related to noise reduction, and smoothing operations. Postclassification techniques are essentially logical operations (working on class labels rather than pixel numbers) which relate the size, position and shape of objects in the image, they are therefore analogous to contextual rules used by manual interpreters. Work in this study, therefore concentrated on this type of post classification operator.

In a large majority of cases contextual operators were able to improve the accuracy of classification, the exception being those cases where the initial accuracy of the classifier was very low. Interestingly, the simple operators, such as median and mode filter, out performed more complex operators such as the gravitational model or minimal area replacement. These findings are in accord with some of the experimental work carried out by Quegan and Rye (1987). Contextual operators not only increase the classification accuracy, they also produce a more subjective enhancement in the visual appearance of classified images, making them less noisy and generally more like thematic maps.

The improvement in classification accuracy produced by contextual features may be more apparent than real. As was noted in a previous chapter the areas classified as alluvium and not shown on the lithological map, in the bottom right of test site 2, in both the MSS and the TM probably belonged to this class. Contextual processing reduced the size of these apparently misclassified objects and therefore increase the apparent classification accuracy by actually making the classification worse. In this case the addition of topographic data would have shown the classification to be correct. This is an example of the remote sensing data being more accurate than the presently available lithological map. It is therefore also an example of where a GIS could potentially update the existing lithological map.

In the final part of the work high level image recognition techniques were adopted in order to emulate the methods used by a photo-interpreter to identify classes in the image. In this simple example, a variety of sedimentary lithologies were placed in a look up table. A class was given a label belonging to a lithology if it fulfilled three criteria, these criteria were based on: tone, texture roughness and texture coarseness

(these are widely used attributes used in manual interpretation). A set of production rules were used to represent the knowledge used by a manual interpreter. Results showed that in this very limited example that three out of five lithologies were correctly identified. Considerable work remains to be done to extend the knowledge base used in this work so that a much wider variety of lithologies and environments. Work must be also carried on less arbitrary boundaries for the attributes used, many more attributes must be used in identifying the lithology if a system is to truly mimic a human interpreter.

Expert Systems also have a major role to play in GIS and remote sensing. Fisher and Wilkinson (1985) use a knowledge-based system coupled to a GIS to automatically extract and label linear features in remotely sensed data. Knowledge-based systems can also be used to incorporate contextual knowledge of the sort 'cars are likely to be found adjacent to roads' (Perkins et al., 1985), they find that using such simple rules considerably improve the initial classification. A geological example of this might be 'a lava flow is likely to be adjacent to a volcanic centre'. Therefore the twin fields of Artificial Intelligence and GIS are inextricably linked to the field of geological remote sensing.

Chapter 10
Conclusions

The objectives of this research are to produce a lithological map by means of digital processing of remotely sensed satellite data. Throughout, regard has been paid to the methods employed by a photogeologist to manually produce a lithological map from the same data set, and to model these methods.

It has been shown that the positioning of spectral bands on the LANDSAT MSS sensor are poor for lithological discrimination. This leads to generally low accuracies for supervised classification techniques using only LANDSAT MSS data. The positioning of spectral bands in the middle infra red on the TM sensor are a significant improvement over the MSS sensor. This leads to better class discrimination and hence significantly higher classification accuracies for TM data.

Registration of SIR-A radar data to MSS and TM data was achieved using less than ten control points. Using SIR-A data to modulate the the brightness of the MSS data produced a subjective visual enhancement of the imagery. This was achieved by adding textural detail to previously homogeneous regions, and by adding strong shadow, which produces pseudo-relief. It was found that modulation of the MSS imagery by the SIR-A data produced increases in the standard deviation of classes, and therefore reduced classification accuracy. Principal components analysis showed that the SIR-A band had a very low correlation with the MSS and TM data. The addition of SIR-A data as an uncorrelated channel to the MSS and TM data significantly improved the classification accuracy of the supervised classifiers, and therefore the radar data must contain complementary lithological information to the MSS and TM data.

Four different types of supervised classifier were tested, namely: the minimum distance to means, the decision tree, the spectral shape, and the maximum likelihood classifiers. Classification accuracies were in the range of 40 to 60% for the MSS and SIR-A data and in the region of 50 to 70% for the TM and SIR-A data. The maximum likelihood classifier consistently produced accuracies 10 to 15% greater than either the decision tree or minimum distance to means classifier. However, the increase in accuracy of the maximum likelihood classifier was at the expense of greatly increased computation time. The spectral shape classifier, which is a new type of supervised classification technique, has the advantage of being computationally simple. The time of calculation was found to be almost identical to that of the minimum distance to means classifier. Results for the spectral shape classifier were generally relatively disappointing, it being

able to distinguish only two or three consistently classes. This was probably due to the ambiguous spectral signatures of the classes. It was felt that the classification accuracies for all the supervised classifiers were unacceptably low and that further attributes used by manual interpreters should be modelled.

Texture is an important feature used by manual interpreters to identify lithology, because the spatial attributes of a lithology can be distinctive, even when the spectral response is ambiguous. Because of this a variety of texture measures were investigated. Three properties of texture can be recognised, these are coarseness, roughness and directionality. All commonly occurring classifiers measure either coarseness and/or roughness, none measure directionality. A texture measure that measured directional properties would be desirable because many geological textures have a strong directional component.

For the TM data, texture measures were able to improve the classification accuracy. However, in the case of the LANDSAT MSS data, texture measures failed to significantly improve the accuracy of classification. It was found that a six band TM data set with three bands of texture and a SIR-A band was over 100 times computationally more expensive than a minimum distance to means classifier using the same bands of data. For the TM data, second order measures were found to be superior to first order texture measures; the SGLDM based measures proving the most effective, with increases in classification accuracy of up to 15%. The differences between results for the MSS and the TM data are related to two causes. Firstly, the MSS has poorer spectral separation of lithology than the TM sensor, this means the MSS is unable to display the lithological textures. Secondly and probably more importantly, the MSS spatial resolution is less than half that of the TM, therefore the MSS may not be able to resolve the distinctive textures of the lithologies.

The classification accuracies using tonal and textural features were still comparatively low, therefore some of the contextual features used by manual interpreters were modelled. Context is a spatially related property that is extensively used by manual interpreters to identify objects in images. Contextual properties include the sizes, positions and shapes of objects. Contextual features such as size and position can (after some initial classification has taken place) be incorporated into classification algorithms. They can include simple low pass filters such as the median or mode, or they can be modelled by more complex operators such as gravitational models or small area replacement. It was found that simple median and mode filters produced better results than the more complex operators, and generally the larger the size of the kernel,

the greater the improvement in the classification accuracy. Contextual post classification filtering was also found to improve the visual appearance of classified imagery by removing small isolated areas of pixels, completely surrounded by pixels belonging to other classes. Contextual features that measure shape properties were not used but are likely to be especially useful with stereoscopic data sets.

Finally, a method was investigated using production rules to identify lithology in the imagery, following the low level classification procedures investigated in the earlier parts of the work. In the very simple situation in the two test sites, three out of five lithologies were correctly identified. Much work remains to be carried out on the effectiveness of such a knowledge based system in more complex situations with a greater variety of lithologies. This is a fertile area of research which can be investigated now that fourth generation languages are available.

References

Allan, J. A. (1986) How few data do we need: some radical thoughts on renewable natural resources surveys. *Proceedings of the 7th International Symposium ISPRS*: Enschede 25- 29th Aug. 1986, 901-906.

Allum, J. A. E. (1966) *Photogeology and regional mapping* Pergammon Press, London 107p.

Anderson, J. R., Hardy, E. E., Roach, J. T. and Witmar, R. E. (1976) *A land use and land cover classification system for use with remote sensing data.* USGS Professional Paper 964, 28p.

Anon. (1979) *Geometric recognition techniques applied to land Landsat digital data.* Earth Satellite Corporation, Washington DC. 291p.

Ashley, R. P. and Abrams, M. J. (1980) *Alteration mapping using multispectral images- Cuprite mining district, Esmeralda County, Nevada.* US Geological Survey Open-File Report 80-367, 19p.

Babcock, E. A. and Sheldon, L. G. (1976) Relationships between photo lineaments and geologic structures, Athabaska oil sands area, northeast Alberta. *Proceedings of the Second International Conference on Basement Tectonics* Newark, Delaware, 177-180.

Ballard, D. H. and Brown, C. M. (1982) *Computer Vision*, Prentice- Hall Inc. New Jersey.

Barnett, M. E., Harnett, P. R., Welford, W. T. and Wynne, C. G. (1976) An iterative hybrid processing facility for geological and geographical applications. *Society of Photoptical Instrumentation Engineers*. **74**, 130-136.

Basden, A. (1984) On the application of Expert Systems. In: *Developments in Expert Systems*. Coombs, M. J. (ed). Academic Press, London.

Baur, M. E., Muasher, M. J. and Landgrebe, D. A. (1981) *Multistage classification of multispectral earth observation data: the design approach.* Laboratory for Applications of Remote Sensing, LARS-101481, Purdue University, Lafayette.

Belward, A. S. and de Hoyos, A. (1987) A comparison of supervised maximum likelihood and decision tree classification for crop cover estimation from multitemporal LANDSAT MSS data. *International Journal of Remote Sensing*, **8**, 229-235.

Bhan, S. K. and Krishnanunni, K. (1983) Applications of remote sensing techniques to geology. *Proceedings of the Indian Academy of Science* , **6**, 297-311.

Blodget, H. W. and Brown, G. F. (1982) *Geological mapping by use of computer enhanced imagery in western Saudi Arabia.* US Geological Survey Professional Paper 1153, 10p.

Blodget, H. W., Gunther, F. J. and Podwysocki, M. H. (1978) *Discrimination of rock classes and alteration products in southwestern Saudi Arabia with computer enhanced LANDSAT data*: US National Aeronautics and Space Administration technical paper 1327, 34p.

Blom, R. and Daily, M. (1982) Radar image processing for rock type discrimination *IEEE Transactions Geoscience and Remote Sensing*, **20**, 343-351.

Brodatz, P. (1966) *Textures- A Photographic Album for Artists and Designers.* Dover, New York.

Brunner, J. S. and Veck, N. J. (1985) Image texture encoding for geological mapping. *Advanced technology for monitoring and processing global environmental data, Proceedings of 11th conference of the Remote Sensing Society.* London September 8-12th,1985, 331-339.

Canoba, C. A. (1983) SIR-A and LANDSAT imagery interpretation of Sierra Velazco, La Rioja Province, Argentina. *ITC Journal*, 232-237.

Chavez, P. S., Berlin, G. L. and Acosta, A. V. (1977) Computer processing of LANDSAT MSS digital data for linear enhancement. Mapping with Remote Sensing Data *Proceedings of the Second Annual Wm. T. Pecora Memorial Symposium.* Sioux Falls, South Dakota, 25-29th October 1976, 235-250.

Chen, P. C. and Pavlidis, T. (1979) Segmentation by texture using a co-occurrence matrix. *Computer Graphics and Image Processing*, **10**, 172-182.

Chen, W. Y. and Collins, W. G. (1982) A new classifier of multispectral scanner data. *Proceedings of Data Processing of Satellite Imagery Symposium.* LARS, Purdue, 100-108.

Cohen, J. (1960) A coefficient of agreement for nominal scales *Educational and Psychological Measurement*, **20**, 37-46.

Colwell, R. N. (1982) (ed.) *Manual of Remote Sensing.* American Society of Photogrammetry, Falls Church, Virginia, 1667-1954.

Congalton, R. G. (1987) Comments on the remote sensing brief reference entitled "Correct formulation of the kappa coefficient of agreement" *Photogrammetric Engineering and Remote Sensing*, **53**, 442.

Congalton, R. G. and Mead, R. A. (1986) A review of three discrete multivariate analysis techniques used in assessing the accuracy of remotely sensed data from error matrices. *IEEE Transactions Geoscience and Remote Sensing*, **24**, 169-174.

Conners, R. W. and Harlow, C. A. (1980) A theoretical comparison of texture algorithms *IEEE Transactions Pattern and Machine Intelligence*, **2**, 204-222.

Cuerda, A. J. (1963) Yacimiento de Baritina en la Provincia de La Rioja. *En Mineria*, **4**, 15-21.

Curran, P. J. (1985) *Principles of Remote Sensing.* Longman, London, 282p.

Curran, P. J. (1987) What is a semi-variogram? *Proceedings of the 13th Annual Conference of the Remote Sensing Society, Advances in Digital Image Processing.* Nottingham, England 7-11th September 1987, 36-45.

Daily, M. (1983) Hue-saturation-intensity split-spectrum processing of Seasat radar imagery. *Photogrammetric Engineering and Remote Sensing*, **49**, 349-355.

Davis, J. C. (1973) *Statistics and data analysis in geology.* Wiley, New York.

Davis, P. A., Grolier, M. J., Schultejann, P. A. and Eliasion, P. T. (1982) Discrimination of phosphate, gypsum, limestone, halide and quartz-sand deposits in south-central Tunisia by cluster analysis of LANDSAT MSS data. *Proceedings of the 1st Thematic conference Remote Sensing of Arid and Semi-arid Lands.* Cairo, Egypt January 1982, 337-369.

Davis, W. A. and Peet, F. G. (1977) A method of smoothing digital thematic maps. *Remote Sensing of Environment*, **6**, 45-49.

Drury, S. A. (1985) Applications of digital image enhancement in regional tectonic mapping of south India. *Proceedings of the 18th International Symposium Remote Sensing of Environment.* Paris, France, 1895-1904.

Drury, S. A. (1986a.) *Image Interpretation in Geology.* Allen and Unwin, London, 243p.

Drury, S. A. (1986b.) Remote sensing of geological structure in temperate agricultural terrains. *Geological Magazine*, **123**, 113-121.

Duda, R. O. and Hart, P. E. (1973) *Pattern classification and scene analysis.* John Wiley and Sons, New York, 201p.

Elachi, C., Brown, W. E., Cimino, J. B., Dixon, T., Evans, D. L., Ford, J. B., Saunders, R. S., Breed, C. S., Masurski, H., Schaber, G., Dellwig, L., England, A., MacDonald, H., Martin-Kaye, P. and Sabins, F. (1982) Shuttle imaging Radar experiment. *Science*, **218**, 996-1006.

Engel, J. L. and Weinstein, O. (1983) The Thematic Mapper - an overview. *IEEE Transactions on Geoscience and Remote Sensing*, **24**, 246-257.

Evans, D. L., Farr, T. G., Ford, J. P., Thompson, T. W. and Werner, G. L. (1986) Multipolarization radar images for geologic mapping and vegetation discrimination. *IEEE Transactions Geoscience and Remote Sensing*, **24**, 246-257.

Evans, D. L. and Stromberg, W. (1983) Development of texture signatures in radar images *IGARSS 83 Remote Sensing Extending Man's Horizon.* San Fransisco, California, 6.1-6.5.

Farr, T. G. (1983) Geologic interpretation of texture in SEASAT and SIR-A radar images. *International Society of Photogrammetry and Remote Sensing Commission VII International Symposium,* Tolouse, France, **1**, 261- 270.

Fischer, W. A. (1976) Introduction to chapter 2, *Application to Geology and Geophysics: ERTS, A New Window on Our Planet.* US Geological Survey Professional Paper 929, 48-49.

Fisher, P. F. and Wilkinson, G. G. (1985) Towards the knowledge-based information systems.*Advanced technology for monitoring and processing global environmental data, Proceedings of 11th conference of the Remote Sensing Society.* London September 8-12th,1985, 51-56.

Fontanel, A., Blanchet, C. and Lallemand, C. (1975) Enhancement of LANDSAT imagery by combination of multispectral classification and principal component analysis. *Proceedings of Earth Resources Symposium* . Houston, Texas, 991-1012.

Fraser, S. J. and Green, A. A. (1987) A software defoliant for geological analysis of band ratios. *International Journal of Remote Sensing*, **8**, 525-532.

Fredericksen, P. (1981) Terrain analysis and accuracy prediction by means of the Fourier Transform. *Photogrammetria*, **136**, 145-157.

Frenguelli, J. (1948) Estratigrafia y edad del llamado retico en la Argentina. *Anales. Soc. Argent. Est. Geog*, **8**, 159-310.

Furque, G. (1979) *Descripcion Geologica, De La Hoja 18c, Jachal.* Carta Geologico de la Republica Argentina.

Galloway, M. M. (1975) Texture analysis using gray level run lengths *Computer Graphics and Image Processing*, **4**, 172-179.

Gentili, C. A. (1972) *Descripcion geologica de la Hoja 17c, Cerro Rajado.* Carta Geologico- Economica de la Republica Argentina, 62p.

Gillespie, A. R. (1976) Directional fabrics introduced by digital filtering of images. *Proceedings of the 2nd International Conference on Basement Tectonics.* Newark, Delaware, 500-507.

Goetz, A. F. H., Billingsley, F. C., Gillespie, A. R., Abrams, M. J., Squires, R. L., Shoemaker, E. N., Lucchita, I. and Elston, D. P. (1975) *Applications of ERTS images and image processing to regional geologic problems and geologic mapping in northern Arizona.* California Institute of Technology, Jet Propulsion Laboratory, Technical Report 32-1597, 188p.

Goetz, A. F. H. and Rowan, L. C. (1983) Remote sensing for exploration: an overview. *Economic Geology*, **78**.

Gold, D. P. and Parizek, R. R. (1976) A study of lineaments, fracture traces and Joints in Pennsylvania. *Proceedings of the 2nd International Conference on Basement Tectonics*. Newark, Delaware, 142.

Goldberg, M., Alvo, M. and Karan, G. (1983) An expert system for the analysis of remotely sensed imagery. *Proceedings of the Spring Convention.* Paris, France. 30th May-3rd June, 263-271.

Gramenopoulos, N. (1973) Terrain type recognition using ERTS-1 MSS images. *Symposium on Significant Results Obtained from the Earth Resources Technology Satellite,* NASA SP-327, 1229-1241.

Gurney, C. M. and Townshend, J. R. G. (1983) The use of contextual information in the classification of remotely sensed data *Photogrammetric Engineering and Remote Sensing,* **49**, 55-64.

Haman, P. J. (1976) Angular and spatial relationships of Landsat lineaments of the United States. *Proceedings of the 2nd International Conference on Basement Tectonics,* Newark, Delaware, 353-360

Haralick, R. M. (1979) Statistical and structural approaches to texture *Proceedings IEEE*, **67**, 786-804.

Haralick, R. M. and Bosley, R. (1973) Texture features for image classification. *Third ERTS Symposium.* NASA SP-351, NASA Goddard Space Flight Center, Greenbelt , MD, 1929-1969.

Haralick, R. M. and Joo, H. (1986) A context classifier *IEEE Transactions Geoscience and Remote Sensing*, **24**, 997-1007.

Haralick, R. M. and Shanmugan, K. (1973) Computer classification of reservoir sandstones. *IEEE Transactions Geoscience and Electronics*, **11**, 171-177.

Haralick, R. M. and Shanmugan, K. (1974) Combined spectral and spatial processing of ERTS imagery. *Remote Sensing of Environment*, **3**, 3-13.

Haralick, R. M., Shanmugan, K. and Dinstein, I'H. (1973) Textural features for image classification *IEEE Transactions Systems, Man and Cybernetics*, **1 3**, 610-621.

Hardy, D. D. (1985) Today the earth is 100 000 000 000 000 bits. Advanced technology for monitoring and processing global environmental data, *Proceedings of 11th conference of the Remote Sensing Society*. London September 8-12th, 1985, 1-4.

Hayes, K. C., Shah, A. N. and Rosenfeld, A. (1974) *Visual texture analysis IV*. Technical Report-320, Computer Center, University of Maryland, Feb 1973.

Henderson, F. B. and Swann, G. A. (1976) *Geological remote sensing from space*. The Geosat Committee, inc. Flagstaff, Arizona, May 10- 14th, 1976, 60p.

Hord, R. M. (1982) *Remote sensing methods and applications*. Academic Press, New York.

Hsu, S-Y (1977) A texture-tone analysis for automated landuse mapping with panchromatic images. *Proceedings of the American Society of Photogrammetry*, 203-215

Hsu, S-Y (1978) Texture-tone analysis for automated land-Use mapping *Photogrammetric Engineering and Remote Sensing*, **44**, 1393-1404.

Hudson, W. D. and Ramm, C. W. (1987) Correct formulation of the kappa coefficient of agreement. *Photogrammetric Engineering and Remote Sensing*, **53**, 421-422.

Hunt, G. R. (1976) Spectral signatures of the particulate minerals in the visible and near infra-red. *Geophysics*, **42**, 738-747.

Hunt, G. R. (1981) Emission spectra in the thermal infra-red region. *Workshop on Geological Applications of Thermal Infrared Remote Sensing Techniques*, 63-71.

IEEE Transactions on Geoscience and Remote Sensing (1984) *Special issue on LANDSAT 4*, **22**, 176- 338.

Indebetuow, G. and Bernardo, L. (1981) Color coding of texture- an analog optical technique *Journal Optics*, **12**, 173-176.

Irons, J. R. and Petersen, G. W. (1981) Texture transform of remote sensing data *Remote Sensing of Environment*, **11**, 350-370.

Jacobberger, P. A., Raska, D. L., Arvidson, R. E. and Batiza, R. (1982) Use of LANDSAT multispectral scanner data in geologic mapping of the Meatiq Dome, central eastern desert, Egypt. *Proceedings of the 1st Thematic conference 'Remote Sensing of Arid and Semi-arid Lands*. Cairo, Egypt Jan 1982, 775-779.

Jensen, J. R. (1986) *Introductory digital image processing- a remote sensing perspective*. Prentice-Hall, Englewood Cliffs, New Jersey.

Kanal, L. N., Lambird, B. A. and Lavine, D. (1983) Knowledge- based systems for remote sensing. *Proceedings of the International Conference on Systems Man and Cybernetics*. Bombay and New Delhi, India, **1**, 171-175.

Kendall, M. (1980) *Multivariate analysis*. (Second edition) Griffin and Co., London.

Koopmans, B. N. (1985) Report on the results in geology and geomorphology of the European SAR -580 experiment. *ITC Journal*, 203-206.

Landgrebe, D. A. (1981) Analysis technology for land remote sensing. *Proceedings of IEEE*, **69**, 628-642.

Lendaris, G. G. and Stanley, G. L. (1970) Diffraction pattern samplings for automatic pattern recognition. *Proceedings of the IEEE*, **58**, 198-216.

Lee, T. and Richards, J. A. (1985) A low cost classifier for multitemporal applications. *International Journal of Remote Sensing*, **6**, 1405-1418.

Lees, R. D., Lettis, W. R. and Bernstein, R. (1985) Evaluation of Landsat Thematic Mapper imagery for geologic applications. *Proceedings of the IEEE*, **73**, 1108-1117.

Lillesand, T. M. and Kiefer, R. W. (1987) *Remote sensing and image interpretation*. 2nd Edition, Wiley and Sons, New York.

McCauley, J. F., Schaber, G. G., Breed, C. S., Grolier, M. J., Haynes, C. V., Issawi, B., Elachi, C. and Blom, R. (1982) Subsurface valleys and geoarcheology of the eastern Sahara revealed by Shuttle Radar. *Science*, **218**, 1004-1020.

McCullagh, M. J. and Davis, J. C. (1972) Optical analysis of two-dimensional patterns. *Annals of the Association of American Geographers*, **62**, 561-577.

Malila, W. A., Metzler, M. D., Rice, D. P. and Crist, E. P. (1984) Characterization of LANDSAT 4 MSS and TM digital image data. *IEEE Transactions on Geoscience and Remote Sensing*, **22**, 177-191.

Mather, P. M. (1985) A computationally efficient maximum likelihood classifier employing prior probabilities for remotely sensed data. *International Journal of Remote Sensing*, **6**, 369-376.

Mather, P. M. (1987) *Computer processing of remotely sensed images*. John Wiley and Sons, Chichester, 352p.

Maurer, H. (1974) Quantification of textures-textural parameters and their significance for classifying agricultural crop types from colour aerial photographs *Photogrammetria*, **30**, 21-40.

Merembeck, B. F., Borden, F. Y., Podwysocki, M. H. and Applegate, D. M. (1977) Application of canonical analysis to multispectral scanner data. *Proceedings of the 14th Annual Symposium on Computer Applications in the mineral Industries*. Society of Mining Engineers, American Institute of Mining, Metallurgical and Petroleum Engineers, New York, 867-879.

Moore, C. K. and Waltz, F. A. (1983) Objective procedures for lineament enhancement and extraction. *Photogrammetric Engineering and Remote Sensing*, **49**, 641-647.

Nazif, A. M. and Levine, M. D. (1984) Low level image segmentation: an expert system. *IEEE Transactions on Pattern and Machine Intelligence*, **6**, 555-577

O'Leary, D. W., Friedman, J. D. and Pohn, H. A. (1976) Lineaments, linear, lineation: some proposed new standards for old terms. *Geological Society of America Bulletin*, **87**, 1463-1469.

Offield, T. W. (1975) Line grating diffraction in image analysis: enhanced detection of linear structures in ERTS images, Colarado Front Range. *Modern Geology*, **5**, 101-107.

Oldfield, R. B. and Elgy, J. (1987) Geological mapping from remotely sensed data using tonal, textural and contextual features. *Advances in Digital Image Processing, Proceedings of the Annual Conference of the Remote Sensing Society.* Nottingham, September, 1987, 553-537.

Oldfield, R. B., Elgy, J. and Morton, J. A. (1988) The use of coregistered LANDSAT MSS, TM and SIR-A imagery for lithological mapping. *IGARSS 88 Remote Sensing: Moving Towards the 21st Century, the 14th Annual Conference of the Remote Sensing Society.* Edinburgh, Sept. 14-16th, 1988.

Peake, W. H. and Oliver, T. L. (1972) *The response of terrestrial surfaces at microwave frequencies.* US Air Forces Lab. Report AFAL-TR-70-301.

Pendock, N. (1987) Fast classification of image data with large spectral dimension. *South African Journal of Photogrammetry, Remote Sensing and Cartography*, **14**, 351-358.

Perkins, W. A., Laffey, J. J. and Nguyen, T. A. (1985) Rule-based interpreting of aerial photographs using LES. *Proceedings of the Society for Photoptical Instrumentation. Applications of Artificial Intelligence*, **548**, 138-146.

Pentland, A. F. (1984) Fractal- based description of natural surfaces. *IEEE Transactions Pattern and Machine Intelligence*, **6**, 661-674

Podwysocki, M. H., Pohn, H. A., Phillips, J. D., Krohn, M. D., Purdy, T. I. and Merin, I. S. (1976) *Evaluation of remote sensing, geological and geophysical data for south- central New York and northern Pennsylvania.* US Geological Survey Open-File Report 82-319, 52p.

Podwysocki, M. H. and Segal, D. B. (1980) *Preliminary digital classification of limonitic rocks, Frisco and 15-minute quadrangle, Utah.* US Geological Survey Open-File Report 80-19.

Podwysocki, M. H., Segal, D. B. and Abrams, M. J. (1982) *Use of multispectral scanner images for assessment of hydrothermal alteration in the Marysvale, Utah, Mining Area.* US Geological Survey Open-File Report 82-675, 29p.

Pohn, H. A. (1970) *Remote sensor application studies progress Report July 1, 1968, to June 30, 1969- Analysis of images and photographs by a Ronchi grating.* US Geological Survey Report, 14p. (NTIS Report number PB 197-101).

Quegan, S. and Rye, A. J. (1987) Automatic interpreter strategies for synthetic-aperture radar images. *Towards Improved Methods of Exploiting Remotely Sensed Imagery.* Royal Society, London, 12th March 1987.

Quershy, M. N. (1982) Geophysical and LANDSAT lineament mapping- an approach illustrated from west- central and south India. *Photogrammetria*, **37**, 161-184.

Quinlan, J. R. (1982) Learning efficient classification procedures and their application to chess end games. Chapter 15. In *Machine learning an artificial intelligence approach.* Michalski, R. S. Carbonell, J. G. and Mitchall, T. M. Tioga Publishing Co, Palo Alto, California, 463-482.

Ray, A. K. Bakliwal, P. C. and Sharma, S. B. (1980) Lineament fabric of western India and its relationship with the genesis and localisation of mineral deposits- a study aided by remote sensing. *Proceedings of Seminar on the Application of photo-interpretation and Remote Sensing Technology for exploration Geology*, 50-56.

Ramapriyan, H. K. (1972) Spatial frequency analysis of multispectral data. *Remote Sensing of Earth Resources,* **1**, 621-644.

Ramapriyan, H. K., Strong, J. P. and Tilton, J. C. (1985) The massively parallel processor- programming and applications. *Proceedings of the 10th William T. Pecora Symposium. Remote Sensing in Forest and Range Resource Management.* 20- 22 August, 546-555.

Reeves, R. G., Kover, A. N., Lyon, R. J. P. and Smith, H. T. U. (1975) Terrain and minerals: assessment and evaluation: *Manual of Remote Sensing.* American Society of Photogrammetry, Falls Church, Virginia, 1107- 1351.

Rebillard, Ph., Pascand, P. N. and Sarrat, D. (1984) Merging Landsat and spaceborne radar over Tunisia. *Advances in Space Research*, **4**, 133- 138.

Robinove, C. J. (1963) Photography and imagery- a classification of terms. *Photogrammetric Engineering*, **29**, 880-881.

Rosenfeld, A. and Thurston, M. (1971) Edge and curve detection for visual scene analysis *IEEE Transactions Computing*, **20**, 562-569.

Rosenfeld, A. and Troy, E. (1970) *Visual texture analysis.* Technical report 70-116, University of Maryland, College Park, MD, June 1970

Rosenfeld, G. H. and Fitzpatrick-Lins, K. (1986) A coefficient of agreement as a measures of thematic classification accuracy. *Photogrammetric Engineering and Remote Sensing*, **52**, 223-227.

Rothery, D. A. (1983) Supervised maximum-likelihood classification and post-classification filtering using MSS imagery for lithological mapping in the Oman ophiolite. *Proceedings of 2nd Thematic Conference, Remote Sensing for Exploration Geology.* Fort Worth, Texas 6-10 December 1982, 417-426.

Rothery, D. A. (1985a) Remote Sensing. *Geology Today*, **1**, 105-108.

Rothery, D. A. (1985b) Interactive processing of satellite images for geological interpretation- a Case Study. *Geological Magazine*, **122**, 57-63.

Rothery, D. A. (1985c) The realities of lithologic mapping by multispectral remote sensing. *Presented to the Geological Information Group of the Geological Society of London.* Birmingham, May 23rd 1985, 4p.

Rothery, D. A. (1987) Decorrelation stretching and related techniques as an aid to image interpretation in geology. *Proceedings of the 13th Remote Sensing Society Conference, Advances in Digital Image Processing.* Nottingham, 7-11th September, 1987, 204-213.

Rothery, D. A. and Francis, P. W. (1987) Synergistic use of MOMS-01 and LANDSAT TM data. *International Journal Of Remote Sensing*, **8**, 501-508.

Rowan, L. C. and Kahle, A. B. (1982) Evaluation of the 0.46-2.36 μm multispectral scanner images of the East Tintic Mining District, Utah, for mapping hydrothermally altered rocks. *Economic Geology*, **77**, 441-452.

Rowan, L. C., Wetlaufer, P. H., Goetz, A. F. H., Billingsley, F. C. and Stewart, J. H. (1974) *Discrimination of rock types and detection of hydrothermally altered areas in south-central Nevada by the use of computer enhanced ERTS images.* US Geological Survey Professional Paper 883, 35p.

Sabins, F. F. (1978) *Remote sensing, pricniples and interpretation.* Freeman, San Fransisco.

Saraph, P. R. and Inamadar, A. B. (1983) Use of textural discrimination techniques in Landsat digital analysis for physical feature identification in mineralized zones *Proceedings International Symposium Remote Sensing of Environment 2nd Thematic Conference, Remote Sensing for Exploration Geology.* Fort Worth Texas, 6-10 Dec, 1982, 977-985.

Shanmugan, K. S., Narayanan, V., Frost, V. S., Stiles, J. A. and Holtzman, J. C. (1981) Textural features for radar image analysis *IEEE Transactions Geoscience and Remote Sensing*, **19**, 153-156

Shih, E. H. H. and Schowengerdt, R. A. (1983) Classification of arid geomorphic surfaces using Landsat spectral and textural features *Photogrammetric Engineering and Remote Sensing*, **49**, 337-347.

Short, N. M. (1982) *The LANDSAT tutorial workbook: basics of satellite remote sensing.* NASA Washington D. C., 553p.

Short, N. M. (1984) Accuracy of computer-based geologic mapping of rock units in the LANDSAT-4 Scene of northern Death Valley, California. *National Conference on Resource Management Applications: Energy and Environment,* 1-21.

Siegal, B. S. and Abrams, M. (1976) Geologic mapping using Landsat data. *Photogrammetric Engineering and Remote Sensing*, **42**, 325-337.

Siegal, B. S. and Gillespie, A. R. (1980) *Remote Sensing in Geology.* John Wiley and Sons, New York, 702p.

Slaney, V. R. (1982) *LANDSAT images of Canada- A geological appraisal.* Geological Survey of Canada Paper 80-15, 102p.

Slegrist, A. W. and Scnetzler, C. C. (1980) Optimum spectral bands in rock discrimination. *Photogrammetric Engineering and Remote Sensing*, **46**, 1207-1215.

Stewart, H. E., Blom, R., Abrams, M. and Daily, M. (1980) Rock type discrimination and structural analysis with LANDSAT and SEASAT data, San Rafael Swell, Utah. *Radar Geology*, 151-67.

Stone, R. J. and McBean, C. W. (1987) Radar discrimination of sebkha environments: A comparison of SIR-A backscatter from Tunisia and Oman. *Advances in Digital Image Processing, Proceedings of the Annual Conference of the Remote Sensing Society.* Nottingham, September, 1987, 611-617.

Strahler, A. H. (1980) The use of prior probabalities in maximum likelihood classification of remote sending data. *Remote Sensing of Environment.*, **10**, 135-163.

Sun, C. J. and Wee, W. G. (1983) Neighboring gray level dependence matrix for texture classification. *Computer Vision Graphics and Image Processing*, **23**, 341-352.

Sutton, R. N. and Hall, E. L. (1972) Texture measures for automatic classification of pulmonary disease. *IEEE Transactions Computers*, **27**, 667-676.

Swain, P. H. and Davis, S. M. (1978) (eds.) *Remote sensing the quantitative approach.* McGraw-Hill, New York.

Swain, P. H. and Hauska, H. (1977) The decision tree classifier: design and potential *IEEE Transactions Geoscience and Electronics*, **15**, 142-145.

Swain, P. H., Vardeman, S. B. and Tilton, J. C. (1981) Contextual classification of multispectral image data *Pattern Recognition*, **13**, 429-441.

Tamura, H., Mori, S. and Yamawaki, T. (1978) Textural features corresponding to visual perception *IEEE Transactions Systems, Man and Cybernetics*, **8**, 460-473.

Tailor, A., Cross, A., Hogg, D. C. and Mason, D.C. (1986) Knowledge based interpretation of remotely sensed images. *Image and Vision Computing*, **4**, 67-83.

Taylor, M. M. (1974) Principal components color display of ERTS imagery. *National Aeronautics and Space Administration Special Publication SP-357 3rd Earth Resources Technology Satellite-1 Symposium*, 10-14 December 1973; Washington D. C. **1**, section B, 1877- 1897.

Thomas, I. L. (1980) Spatial post processing of spectrally classified LANDSAT data. *Photogrammetric Engineering and Remote Sensing*, **46**, 1201-1206.

Thomas, I. L., Howarth, R., Eggers, A. J. and Fowler, A. D. W. (1981) Textural enhancement of a circular geological feature. *Photogrammetric Engineering and Remote Sensing*, **47**, 98-91.

Tilton, J. C., Vardeman, S. B. and Swain. P. H. (1982) Estimation of context for statistical classification of multispectral image data *IEEE Transactions Geoscience and Remote Sensing*, **20**, 445-452.

Tomlins, G. F. (1981) Canadian experience in wetland monitoring by satellite. In: Smith, H. (ed.) *Plants and the daylight Spectrum.* Academic Press, London, 102-103.

Trevett, W. (1986) *Imaging radar for resources surveys.* Chapman and Hall, London.

Triendl, E. E. (1972) Automatic terrain mapping by texture recognition *Proceedings of the Eighth International Symposium on Remote Sensing of Environment.* University of Michigan, 771-776.

Ulaby, F. T., Kauyate, F. Brisco, B. and Williams, T. H. (1986) Textural information in SAR images *IEEE Transactions Geoscience and Remote Sensing*, **24**, 235-245.

University of Michigan (1962) *Proceedings of the first symposium on remote sensing of environment. University of Michigan, Institute of Science and Technology, Infrared Laboratory.* Ann Arbor, Michigan; 13-15 February 1962, 149p.

Venable, S. F. Richter, D. and Wiedmann, M. (1985) A rule-based system for improving image segmentation. *IEEE Conference on Artificial Intelligence Applications. The Engineering of Knowledge Based Systems*, Miami Beach, Florida, 94-99.

Vincent, R. K., Rowan, L. C., Gillespie, R. E. and Fowler, A. D. W. (1975) Thermal infrared spectra and chemical analyses of twenty-six igneous rock samples. *Remote Sensing of Environment*, **4**, 199-209.

Watkins, A. H. and Freden, S. C. (1979) *Landsat data users handbook.* US Geological Survey.

Weszka, J. S., Dyer, C. R. and Rosenfeld, A. (1976) A comparative study of texture measures for terrain classification. *IEEE Transactions Systems, Man and Cybernetics*, **6**, 269-285.

Wharton, S. W. (1982) A contextual classification method for recognizing land use patterns in high resolution remotely sensed data. *Pattern Recognition*, **15**, 317-324.

Williams, R. S. (1983) (ed.) Geological Applications. In: Colwell (1983), 1726-1951.

Wheeler, R. L. and Stubbs, J. L. (1976) Style elements of systematic joints: statistical analysis of size, spacing and other characteristics. *Proceedings of the 2nd International Conference on Basement Tectonics.* Newark, Delaware, 491-499.

Yu, T. S. and Fu, K. S. (1983) Recursive contextual classification using a spatial stochastic model. *Pattern Recognition*, **16**, 89-108.

Appendix 1 Flow Chart of the Spectral Shape Classifier

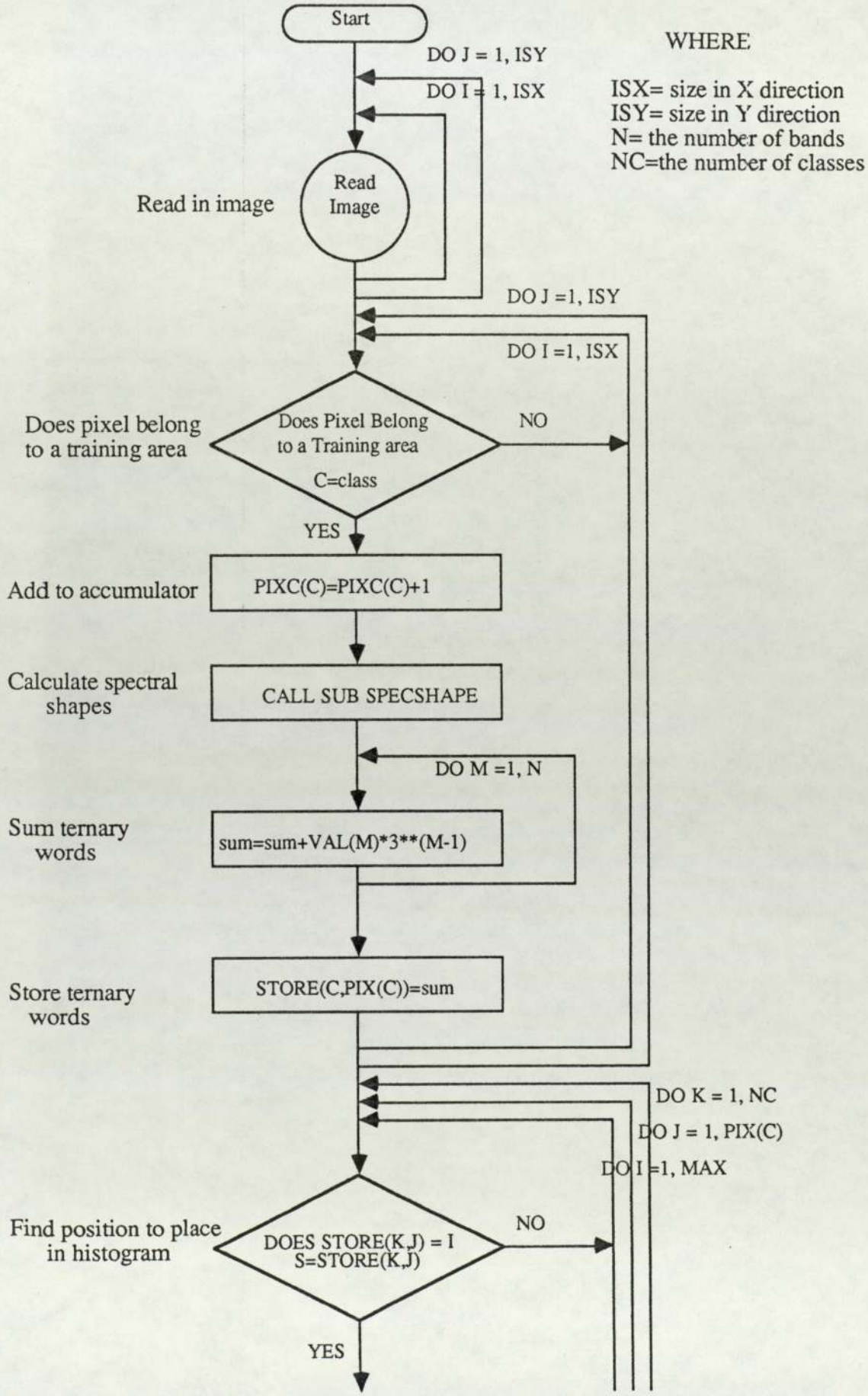

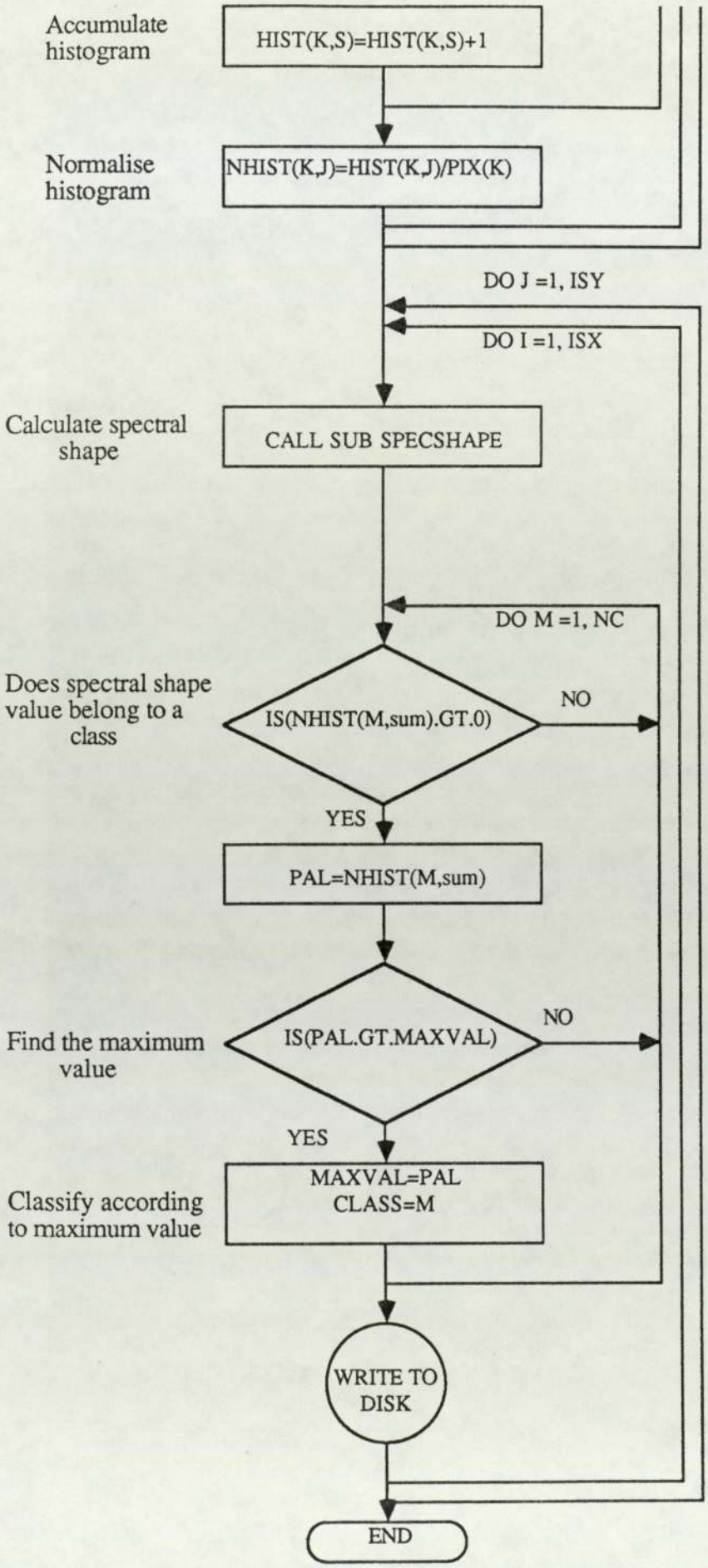
Accumulate histogram
HIST(K,S)=HIST(K,S)+1
Normalise histogram
NHIST(K,J)=HIST(K,J)/PIX(K)
DO J =1, ISY
DO I =1, ISX
Calculate spectral shape
CALL SUB SPECSHAPE
DO M =1, NC
Does spectral shape value belong to a class
IS(NHIST(M,sum).GT.0)
NO
YES
PAL=NHIST(M,sum)
Find the maximum value
IS(PAL.GT.MAXVAL)
NO
YES
Classify according to maximum value
MAXVAL=PAL
CLASS=M
WRITE TO DISK
END

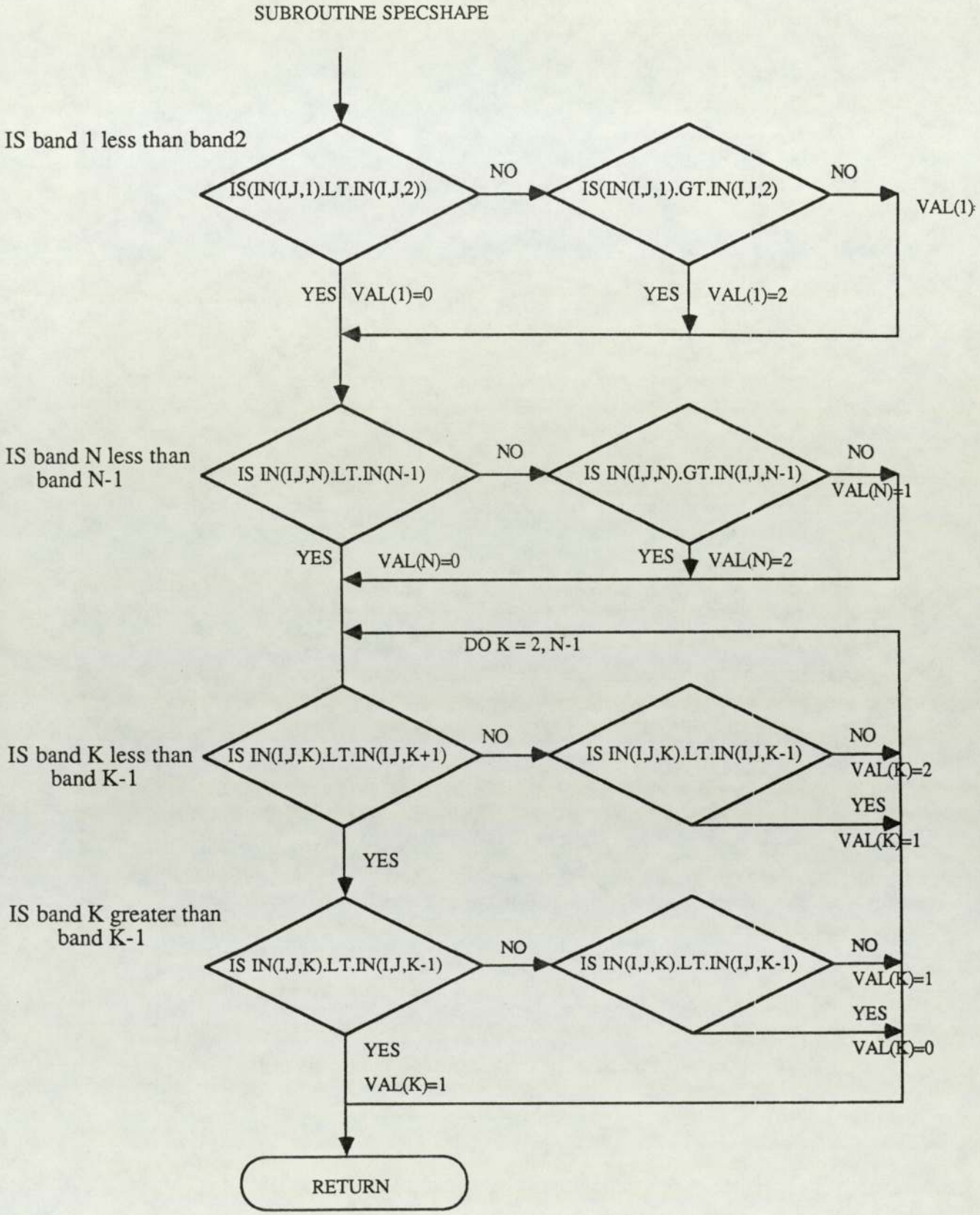
SUBROUTINE SPECSHAPE
IS band 1 less than band2
IS(IN(I,J,1).LT.IN(I,J,2))
NO
IS(IN(I,J,1).GT.IN(I,J,2)
NO
VAL(1)
YES
VAL(1)=0
YES
VAL(1)=2
IS band N less than band N-1
IS IN(I,J,N).LT.IN(N-1)
NO
IS IN(I,J,N).GT.IN(I,J,N-1)
NO
VAL(N)=1
YES
VAL(N)=0
YES
VAL(N)=2
DO K = 2, N-1
IS band K less than band K-1
IS IN(I,J,K).LT.IN(I,J,K+1)
NO
IS IN(I,J,K).LT.IN(I,J,K-1)
NO
VAL(K)=2
YES
VAL(K)=1
YES
IS band K greater than band K-1
IS IN(I,J,K).LT.IN(I,J,K-1)
NO
IS IN(I,J,K).LT.IN(I,J,K-1)
NO
VAL(K)=1
YES
VAL(K)=0
YES
VAL(K)=1
RETURN

Appendix 2

The five texture features which were suggested by Galloway (1975), which can be calculated from the grey level run length matrix.

Where:

p(i, j) is the (i, j)th entry in the given run length matrix.

Ng is the number of grey levels in the image.

Nr is the number of different run lengths that occur.

P is the number of pixels in the image.

1. Short Run Emphasis

$$RF1 = \sum_{i=1}^{Ng}\sum_{j=1}^{Nr}(p(i, j)/j^2)/\sum_{i=1}^{Ng}\sum_{j=1}^{Nr}p(i, j)$$

2. Long Run Emphasis

$$RF2 = \sum_{i=1}^{Ng}\sum_{j=1}^{Nr}j^2p(i, j)/\sum_{i=1}^{Ng}\sum_{j=1}^{Nr}p(i, j)$$

3. Grey Level Nonuniformity

$$RF3 = \sum_{i=1}^{Ng}(\sum_{j=1}^{Nr}p(i, j))^2/\sum_{i=1}^{Ng}\sum_{j=1}^{Nr}p(i, j)$$

4. Grey Level Nonuniformity

$$RF4 = \sum_{j=1}^{Ng}(\sum_{i=1}^{Nr}p(i, j))^2/\sum_{i=1}^{Ng}\sum_{j=1}^{Nr}p(i, j)$$

5. Run Percentage

$$RF5 = \sum_{i=1}^{Ng}\sum_{j=1}^{Nr}p(i, j)/P$$

Appendix 3

The fourteen texture measures described by Haralick et al. (1973), where:

p(i, j) is the (i, j)th entry in a normalised grey tone spatial dependence matrix.

$p_x(i)$ is the ith entry in the marginal probability matrix obtained by summing the rows of p(i, j), $= \sum^{Ng} p(i, j)$.

Ng is the number of grey levels in the image.

1) Angular Second Moment

$$ASM=\sum_i \sum_j \{p(i,j)\}^2$$

2) Contrast

$$CON=\sum_{n=0}^{Ng-1} n^2 \left\{ \sum_{i=1}^{Ng} \sum_{j=1}^{Ng} p(i,j) \right\}$$

where n= Ii-jI

3) Correlation

$$COR=\frac{\sum_i \sum_j (ij)p(i,j)-\mu_x\mu_y}{\sigma_x\sigma_y}$$

where μ_x, μ_y, σ_x and σ_y are the means and standard deviations of p_x and p_y

4) Sum of Squares (Variance)

$$SS=\sum_i \sum_j (i-\mu)^2 p(i,j)$$

5) Inverse Difference Moment

$$IDM=\sum_i \sum_j \frac{1}{1+(i-j)^2} p(i,j)$$

6) Sum Average

$$SA=\sum_{i=2}^{2Ng} i p_{x+y}(i)$$

7) Sum Variance

$$SV=\sum_{i=2}^{2Ng} (i-SE)^2 p_{x+y}(i)$$

8) Sum Entropy

$$SE=\sum_{i=2}^{2Ng} p_{x+y}(i)\log\{p_{x+y}(i)\}$$

9) Entropy

$$E=-\sum_i\sum_j p(i,j)\log(p(i,j))$$

10) Difference Variance

DV= variance of p_{x-y}

11) Difference Entropy

$$DE=-\sum_{i=0}^{Ng-1} p_{x-y}(i)\log\{p_{x-y}(i)\}$$

12) and 13) Information Measures of Correlation

$$12 = \frac{HXY-HXY1}{\max\{HX,HY\}}$$

$$13 = (1-\exp[-2.0(HXY2-HXY)])^{0.5}$$

where $HXY= -\sum_i\sum_j p(i,j)\log(p(i,j))$

HX and HY are entropies of px and py

$$HXY1 = -\sum_i\sum_j p(i,j)\log\{p_x(i)p_y(j)\}$$

$$HXY2 = -\sum_i\sum_j p_x(i)p_y(j)\log\{p_x(i)p_y(j)$$